EFFECTS OF PLASMA, TEMPERATURE AND CHEMICAL REACTIONS ON POROUS LOW DIELECTRIC FILMS FOR SEMICONDUCTOR DEVICES

Eric Osei-Yiadom, B.S., M.S.

Dissertation Prepared for the Degree of

DOCTOR OF PHILOSOPHY

UNIVERSITY OF NORTH TEXAS

December 2010

APPROVED:

Richard F. Reidy, Major Professor
Jincheng Du, Committee Member
Thomas W. Scharf, Committee Member
Rajarshi Banerjee, Committee Member
Nigel Shepherd, Coordinator of the Program in Materials Science and Engineering
Narendra Dahotre, Chair of the Department of Materials Science and Engineering
Costas Tsatsoulis, Dean of the College of Engineering
James D. Meernik, Acting Dean of the Robert B. Toulouse School of Graduate Studies

Osei-Yiadom, Eric. Effects of plasma, temperature and chemical reactions on porous low dielectric films for semiconductor devices. Doctor of Philosophy (Materials Science and Engineering), December 2010, 171 pp., 9 tables, 69 illustrations, 209 references.

Low-dielectric (*k*) films are one of the performance drivers for continued scaling of integrated circuit devices. These films are needed in microelectronic device interconnects to lower power consumption and minimize cross talk between metal lines that "interconnect" transistors. Low-*k* materials currently in production for the 45 and 65 nm node are most often organosilicate glasses (OSG) with dielectric constants near 2.8 and nominal porosities of 8-10%. The next generation of low-*k* materials will require *k* values 2.6 and below for the 45 nm device generation and beyond. The continuous decrease in device dimensions in ultra large scale integrated (ULSI) circuits have brought about the replacement of the silicon dioxide interconnect dielectric (ILD), which has a dielectric constant (*k*) of approximately 4.1, with low dielectric constant materials. Lowering the dielectric constant reduces the propagation delays, RC constant (*R* = the resistance of the metal lines; *C* = the line capacitance), and metal cross-talk between wires. In order to reduce the RC constants, a number of low-*k* materials have been studied for use as intermetal dielectrics. The *k* values of these dielectric materials can be lowered by replacing oxide films with carbon-based polymer films, incorporating hydrocarbon functional groups into oxide films (SiOCH films), or introducing porogens in the film during processing to create pores. However, additional

integration issues such as damage to these materials caused by plasma etch, plasma ash, and wet etch processes are yet to be overcome.

This dissertation reports the effects of plasma, temperature and chemical reactions on low-*k* SiOCH films. Plasma ash processes have been known to cause hydrophobic films to lose their hydrophobic methyl groups, rendering them to be hydrophilic. This allows the films to readily absorb moisture. Supercritical carbon dioxide (SC-CO_2) can be used to transport silylating agents, hexamethyldisilazane (HMDS) and diethoxy-dimethlysilane (DEDMS), to functionalize the damaged surfaces of the ash-damaged films. The thermal stability of the low-*k* films after SC-CO_2 treatment is also discussed by performing in-situ heat treatments on the films. UV curing has been shown to reduce the amount of pores while showing only a limited change dielectric constant. This work goes on to describe the effect of UV curing on low-*k* films after exposing the films to supercritical carbon dioxide (CO_2) in combination with tetramethylorthosilicate (TMOS).

ACKNOWLEDGMENTS

About a little over six years ago, I arrived in the USA from Ghana to pursue my graduate education. Little did I know that after six years, I would be graduating with my doctorate degree. I thank God for taking me through this phase of my life. I would also want to thank my wife Afua, my daughter Erica and Auntie Doris for supporting me through all of this. Without their support and the smile that greeted me after a stressful day, those days would have been really long. I love you all. I am forever grateful to my advisor and friend Dr. Richard F. Reidy, who prefers to be called Rick, for taking me under his wing and instilling in me how to relate to people and for making me a good student. I also like to thank my committee members, Dr. Jincheng Du, Dr. Thomas W. Scharf, Dr. Rajarshi Banerjee for spending quite a time reading this dissertation and making the best of it in a short period of time; nor do I want to forget all the faculty in MTSE department who helped in shaping me to be the person I am today. I would like to thank all of my friends and team members (some of them have left and others are still here) who were all supportive and made life here comfortable: Nelson, Oseoghaghare, Carl, Ian, Pete, Casey, Benedict, Fang-Ling, Arun, Antariksh, Mathias and Nanny. I would also like to thank CART, especially Nancy for being helpful. And not to forget the MTSE department front office: Wendy, April, Joan and Amy; you guys have been helpful. If I accidentally have left someone out, accept my apologies. Lastly, I would like to say a big thank you to my wonderful parents for making me the man that I am today.

TABLE OF CONTENTS

Page

LIST OF TABLES

Page

LIST OF ILLUSTRATIONS

CHAPTER 1

INTRODUCTION

1.1 Low-*k* Films

Low-dielectric (*k*) films are one of the performance drivers to back end of line (BEOL) integration. In integrated circuit (IC) manufacturing, BEOL involves creating metal interconnecting wires that are isolated by insulating dielectrics. These interlayer dielectrics (ILD) electrically separate closely spaced interconnect lines arranged in several level in an IC, while on the other hand, intermetal dielectrics (IMD) are deposited between metal layers (Fig. 1). These films are needed in microelectronic device interconnects to lower power consumption and minimize cross talk between metal lines. Low-*k* materials currently in production for the 65 nm node are most often organosilicate glasses (OSG) with dielectric constants near 2.8 and nominal porosities of 8-10%. The next generation of low-*k* materials will require *k* values below 2.6 for the 45 nm device generation and beyond [1]. The continuous decrease in device dimensions in ultra large scale integrated (ULSI) circuits have brought about the replacement of the silicon dioxide interconnect dielectric (ILD), which has a dielectric constant (*k*) of approximately 4.1, with low dielectric constant materials. Lowering the dielectric constant reduces the propagation delays, and metal cross-talk between wires, and power dissipation from RC coupling (*R* = the resistance of the metal lines; *C* = the line capacitance) [2]. In order to

reduce the RC constants, a number of low-*k* materials have been studied for use as intermetal dielectrics. The *k* values of these dielectric materials can be lowered by replacing oxide films with carbon-based polymer films, incorporating hydrocarbon functional groups into oxide films (also called SiOCH films) [3] or introducing porogens in the film during processing to create pores. Thin films synthesized by chemical vapor deposition (CVD) and spin-on methods have been studied and implemented as replacements for SiO_2. CVD-deposited porous carbon doped oxide dielectrics (SiOCH) have been widely studied as a promising candidate for interlayer dielectric applications in multilevel interconnect architectures [4]. The SiOCH film is suitable for ultra large scale integrated applications because it has a *k* of less than 2.9 [5] and can go to less than 2.6. The SiOCH is composed of a Si-O base with incorporation of methyl (CH_3). The Si-O present in the film provides good properties similar to that of silicon dioxide (SiO_2) [6], but the film chemical stability and reactivity strongly depend on porosity, pore size, and interconnectivity. The addition of methyl groups lower polarization (and dielectric constant) by decreasing film density and introducing Si-C bonds that are less polar than Si-O bonds. By introducing pores into a dielectric material, the dielectric constant can be reduced because air has a dielectric constant of ~1.

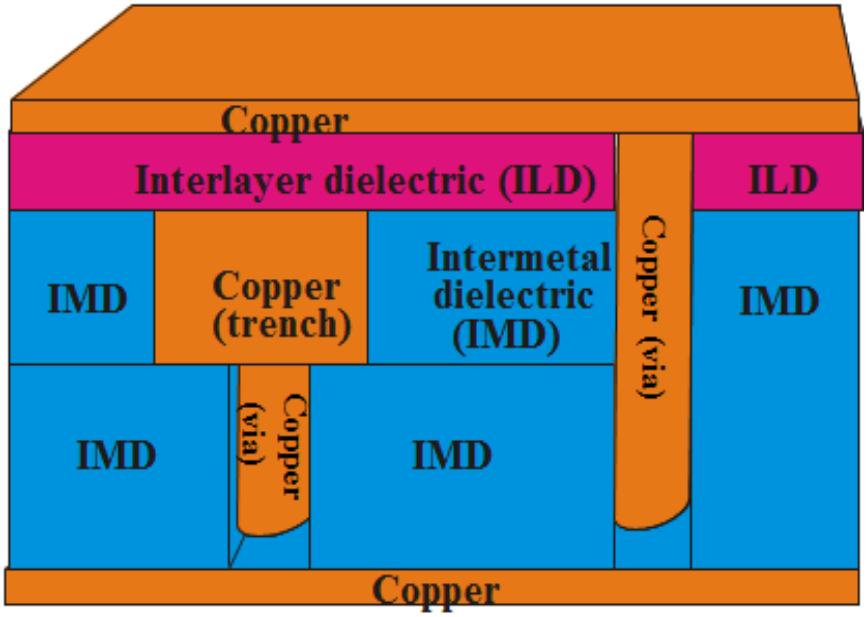

Fig. 1.1. A 3-dimensional image of an IC showing IMD, ILD and copper trench and vias.

In back end of line (BEOL) integration of semiconductor chips, different plasma treatments are widely employed to etch, cap layers, post-etch treatments, such as photoresist strip or etch residue cleaning. A dielectric etch approach most widely employed is the dual damascene. This process consecutively generates embedded vias and trenches, with the vias forming vertical connections from one layer of circuitry (trenches) to the next (Fig. 1.1). The introduction of pores or a change in porosity in a dielectric material can possibly affect the etch behavior of these materials, hence it is important to study the effects of different plasmas on SiOCH films. Plasma treatment processes result in complex combinations of chemical reactions between the surface species and the radicals formed in a discharge volume, and the physical impact of sputtering by ion bombardment [7]. A number of factors including the plasma composition, power, temperature and treatment time influence this process and determine

etching rate, uniformity and selectivity as well as the extent of damage to the dielectric film [8]. Interaction of these plasmas with the SiOCH films causes carbon depletion on the surfaces of these films that, induces the formation of silanols, film densification and dangling bonds defects [9], making these films hydrophilic. In other words, these plasmas damage the normally chemically stable SiOCH films. It has been reported that oxygen plasmas which are typically employed for photoresist stripping lead to the formation of a densified thin layer at the near surface region of the SiOCH film thereby protecting the $-CH_3$ groups in the bulk material from being oxidized [10,11]. Other authors have also come to the conclusion that O_2 plasma treatment does not seal an organic low-*k* film [12,13].

Several approaches have been used to repair damage to SiOCH low-*k* films after ashing. The first approach is to use He, H_2, or NH_3 plasmas to treat the oxygen plasma ashed films and restore the dielectric constant [14,15]. The second approach is to implant boron (B) or arsenic (As) to protect the film during plasma ashing [16,17]. The third approach is to use a silylating agent such as HMDS or TMCS vapor followed by annealing to remove OH groups and produce a hydrophobic surface [18,19]. Exposure to the different plasmas creates a hydrophilic surface which is susceptible to water absorption and also has a high surface free energy. The hydrophilic surfaces of plasma damaged SiOCH films is a result of the presence of hydroxyl (-OH) on these surfaces. Silylating agents such as hexamethyldisilazane [20] (HMDS, as it will be called in this work) or diethoxy-dimethlysilane (DEDMS, as will be called in this work) can be used to modify these surfaces by replacing the hydroxyl groups with hydrophobic methyl species.

These reactions normally require high concentrations of organic solvents and reaction time of up to 24 hours. Supercritical CO_2 based process is a process that uses less volume of toxic solvents thereby increasing rapidly the reaction times. Because of the gas-like transport properties and near liquid densities of supercritical CO_2 and its easily accessible critical point (31.1 °C and 1170 psi, 73.8 bar), it offers an excellent medium for processing porous low-*k* dielectrics. Even though carbon dioxide is a nonpolar molecule, varying pressure, temperature, and co-solvents can control its solvating capability in the supercritical state [21]. Supercritical CO_2 finds applications in a variety of fields. These fields include but are not limited to polymerizations [22], pharmaceutical applications [23], textile processing and dyeing [24], coatings [25], natural products/food extractions [26], specialized materials fabrications [27], cleaning [28], and chromatography [29].

An important property required of these new ILD's is the thermal stability because the IC processing (post copper deposition anneal) conditions call for temperatures in the range of 400-425 °C. Therefore there is a specific need to study the temperature effects on the properties of these SiOCH films both before and after silylation treatments. It is believed that thermal treatments of SiOCH films reduce the *k* value to < 2 (making it an ultra-low-*k* material) by removing thermally unstable components from the films or intentionally deposited chemistries that generates porosity in the films [30]. At high enough temperatures, hydroxyl groups which make the films hydrophilic and also increasing the water absorption are also removed.

Conventional thermal curing processes appears to be insufficient to achieve a robust material with suitable strength required for BEOL integration processes, such as

chemical mechanical planarization [31] (CMP) and packaging [32]. Ultraviolet irradiation curing is a method that has showed most promise in reducing the number of pores in porous SiOCH films and possibly increasing the mechanical strength of porous low-*k* SiOCH materials [33,34] while showing only a limited change of dielectric constant. A UV light source is known to deliver energy in the form of photons. UV irradiation also reduces the ionic and orientational polarizations by removing the weak bonded and unstable CH_3 bonds in low-*k* SiOCH films, thereby reducing the *k* value. By increasing the intensity of the UV source, enhancement to this process can be achieved without compromising thermal budget (because you don't need a high temperature furnace and the duration is minimal). Because silylating species react most effectively within 20 Å of the film surface, these species may readily react with UV irradiation to form very thin barrier layers. A UV light source emits energy in the form of photons, and the energy delivered is inversely proportional to the wavelength of the light source. With UV curing, the cross-linking kinetics can be enhanced by just increasing the intensity of the UV.

1.2 Organization of Dissertation

The dissertation is organized into seven chapters. The first chapter gives a review of what each chapter presented in this dissertation is about. The second chapter addresses recent work on low-*k* dielectric materials such as effects of plasma ashing on low-*k* films and a process for repairing the damage caused. Recent work focused on thermal stability of low-*k* films and the process of enhancing pore sealing in porous low-*k* films are also discussed in this chapter.

In chapter 3 an overview of the experimental procedure and characterization techniques used in this dissertation is presented.

As-deposited (unashed) low-*k* SiOCH films are hydrophobic, plasma treatments which are used mostly in the semiconductor industry for cleaning process and etching rids these films of the hydrophobic methyl groups and replaces them with polar silanol groups. This makes the films hydrophilic and hence increasing the *k* value and also making them susceptible to moisture absorption. In chapter 4, the effects of using supercritical carbon dioxide (SC-CO_2) together with hexamethyldisilazane (HMDS) and diethoxydimethylsilane (DEDMS) silylation agents to repair ash-damaged low-*k* SiOCH films is investigated.

Copper damascene structures call for interconnect processing temperatures over 400 °C and, has recently generated interest in studying the thermal stability of low-*k* dielectrics. Hence, in chapter 5, the effects of temperature on unashed low-*k* CVD SiOCH film and on repaired plasma damaged films using HMDS and DEDMS are discussed.

Silylating agents have been shown to recover surface hydrophobicity and to prevent water and precursor moieties from intruding into porous silica-based low-*k* films. When further aggressive plasma conditions damage dielectric constants, these chemistries can repair film dielectric constants and prevent thickness losses during wet etch/cleans. UV curing has been shown to enhance low-*k* mechanical properties while showing only a limited increase of dielectric constant. In chapter 6, tetramethylorthosilicate or tetramethyloxysilane (TMOS) are discussed as silylating agents to enhance pore sealing

in porous low-*k* SiOCH. Finally, chapter 7 discusses the conclusions for this dissertation, as well as giving an insight to future work that can be done to improve this dissertation.

1.3 References

[1] International Technology Roadmap for Semiconductors, 2008 Update

[2] A. Grill, J. Appl. Phys., 93-3 (2003) 1785-1790.

[3] S. Lee, D. Jung, J. Yang, J. H. Boo, H. Kim, J. Lee, H. Chae, J. Mater. Res. 23- 3 (2008) 856-861.

[4] A. Grill, V. Patel, J. Appl. Phys. 85 (1999) 3314.

[5] Y. H. Wang, R. Kumar, X. Zhou, J. S. Pan, J. W. Chai, Thin Solid Films 473 (2005) 132-136.

[6] S. Lee, J. Yang, S. Yeo, J. Lee, D. Jung, J. Boo, H. Kim, H. Chae, Japanese J. Appl. Phys., 46-2 (2007) 536-541.

[7] E. Tanglauer, Appl. Phys. A 51 (1990) 3314.

[8] E. Vinogradova, E. Osei-Yiadom, C.E. Smith, D.W. Mueller, R. F. Reidy, Microelectronic Eng. 86 (2009) 176-180.

[9] E. Kondoh, M. R. Baklanov, H. Bender, K. Max, Electro-Chem. Solid State Lett. 1 (1998) 224.

[10] J. N. Sun, D. W. Gidley, Y. Hu, W. Frieze, Appl. Phys. Lett. 81 (2002) 1447.

[11] T. K. Goh, T. K. S. Wong, Microelectron. Eng. 75 (2004) 330.

[12] A. M. Hoyas, J. Schuhmacher, C. M. Whelan, M. R. Baklanov, L. Carbonell, J. P. Celis, K. Maex, J. Vac. Sci. Technol. B 23 (2005) 1551.

[13] P. Yang, D. Lu, R. Kumar, H. O. Moser, Nucl. Instr. Meth. Phys. Res. B 238 (2005) 310-313.

[14] T. C. Chang, Y. S. Mor, P. T. Liu, T. M. Tsai, C. W. Chen, Y. J. Mei, F. M. Pan, W. F. Wu, S. M. Sze, Microelectron. Eng. 60 (2002) 469-475.

[15] Y. H. Wang, D. Gui, R. Kumar, P. D. Foo, Electro-chem. Solid-State Lett.(2003) F1-F3.

[16] C. Y. Wang, J. Z. Zheng, Z. X. Shen, Y. Lin, A. T. S. Wee, Thin Solid Films 397 (2001) 90-94.

[17] T. C. Chang, Y. S. Mor, P. T. Liu, T. M. Tsai, C. W. Chen, Y. J. Mei, S. M. Sze, Thin Solid Films 398-399 (2001) 637-640.

[18] Y. S. Mor, T. C. Chang, P. T. Liu, T. M. Tsai, C. W. Chen, S. T. Yan, C. J. Chu, W. F. Wu, F. M. Pan, W. Lur, S. M. Sze, J. Vac. Sci. Technol. B 20 (2002) 1334-1338.

[19] T. C. Chang, P. T. Liu, Y. S. Mor, T. M. Tsai, C. W. Chen, Y. J. Mei, F. M. Pan, W. F. Wu, S. M. Sze, J. Vac. Sci. Technol. B 20 (2002) 1561-1566.

[20] A. V. Rao, E. Nilsen, M. A. Einarsrud, J. Non-Cryst.Solids 296 (2001) 165.

[21] L. T. Taylor, Supercritical Fluid Extraction (Wiley, New York, 1996).

[22] J. L. Kendall, D. A. Canelas, J. L. Young, J. M. DeSimone, Chem. Rev. 99 (1999) 543-563.

[23] U. B. Kompella, K. Koushik, Crit. Rev. Thermal Drug Carrier Syst. 18 (2001) 173-199.

[24] G. A. Montero, C. B. Smith, W. A. Hendrix, D. L. Butcher, Ind. Eng. Chem. Res. 39 (2000) 4806-4812.

[25] K. Johns, G. Stead, (Eds.), Supercritical Fluids for Coatings-From Analysis to Xenon. A Brief Overview, Vol. 2, Kluwer Academic/Plenum Publishers, New York, NY, 1999.

[26] M. Sihvonen, E. Jarvenpaa, V. Hietaniemi, R. Huopalahti, Trends Food Sci. Technol. 10 (1999) 217-222.

[27] A. I. Cooper, Adv. Mater. 13 (2001) 1111-1114.

[28] J. McHardy, S. P. Sawan, Supercritical Fluid Cleaning Fundamentals, Technology and Applications, Noyes, Westwood, NJ, 1998.

[29] M. D. Palmieri, J. Chem. Educ. 66 (1989) A141-147.

[30] S. Lee, D. Jung, J. Yang, J. H. Boo, H. Kim, J. Lee, H. Chae, J. Mater. Res., Vol. 23, No. 3 (2008) 856-861.

[31] P. Leduc, M. Savoye, S. Maitrejean, D. Scevola, V. Jousseaume, G. Passemard, Interconnect Technology Conference, San Francisco, CA, U.S.A., June 6-10, Conference Proceedings, IEEE Service Center, Piscataway, NJ, 2005, 209.

[32] G. Kloster, T. Scherban, G. Xu, G., J. Blaine, B. Sun, Y. Zhou, Interconnect Technology Conference, San Francisco, CA, U.S.A., June 3-5, Conference Proceedings, IEEE Service Center, Piscataway, NJ, 2002, 242.

[33] J. Ushio, T. Ohno, T. Hamada, S. I. Nakao, K. Yoneda, M. Kato, N. Kobayashi, Jpn J. Appl. Phys. 46 (2007) L405.

[34] S. Giangrandi, B. Brijs, T. Sajavaara, H. Bender, F. Iacopi, A. Vantomme, W. Vandervorst, Nucl. Inst. And Methods in Physics Research B 249 (2006) 189-192.

CHAPTER 2

LITERATURE REVIEW

2.1 Low-Dielectric Constant (*k*) Films

2.1.1 Introduction

The continuous scaling down or shrinking of the ultra large scale integrated (ULSI) circuits requires replacing interlayer and intermetal dielectrics (ILD and IMD) to continue to decrease well below silica (k~4.1) to values less than 2.6. These low dielectric constant materials are necessary to reduce metal cross-talk, and RC coupling delay (R = resistance of metal lines; C = line capacitance) which causes power dissipation. For some time now, there have been a number of candidate materials for low-*k*interconnect applications some of which are listed in Table 2.1.

Table 2.1
Candidates for low-*k* interconnect applications [1].

Materials	Dielectric Constant	Deposition method
Ultra low-k materials ($k \leq 2.2$)		
Teflon-AF	1.9 – 2.1	Spin on
Teflon – microemulsion	1.9 – 2.1	Spin on
Porous materials		
SiOCH	2.3	CVD
Porous Silk	2.2	Spin on
Silica aerogels	1.3 – 2.2	Spin on
Silica xerogels	1.5 – 2.2	Spin on
Mesoporous silica	1.9 – 2.2	Spin on
Methylsilsesquioxane (MSQ)	2.2-2.5	Spin-on

The International Roadmap for Semiconductors (ITRS) indicates that materials with dielectric constant lower than 2.7 are required as device features sizes shrink below the 65 nm technology nodes [2], hence efforts have been made to decrease the dielectric constant of ILD been used. The introduction of free volume (micropores < 2nm in diameter) or mesoporosity (2 – 50 nm diameter pores) into a dielectric has become an approach of creatingultra-low-*k* materials. This is achieved by introducing porogens that are removed in later thermal treatments during the fabrication process. However, the presence of pores in a material reduces the mechanical strength and increases its active

surface area, thereby making it susceptible to moisture and deleterious chemical adsorption during device fabrication [3,4]. As porosity increases, the effects of surface groups, bonding, compositional variations and interconnectivity within the solid network become critical factors in film dielectric constant and mechanical properties because specific surface area (surface area of unit weight) increases significantly as porosity increases.

New low-*k*materials which are glassy materials containing Si, C, O, and H have been studied as ILD's. One of such material is porous carbon-doped oxide (SiOCH as will be used in this work) have been studied because of its adaptable integration properties [5]. The SiOCH is composed of Si-O with incorporation of methyl (CH_3). The Si-O present in the film provides good properties similar to that of silicon dioxide (SiO_2) [6]. A networked structure of a SiOCH film is given in Fig. 2.1 below.

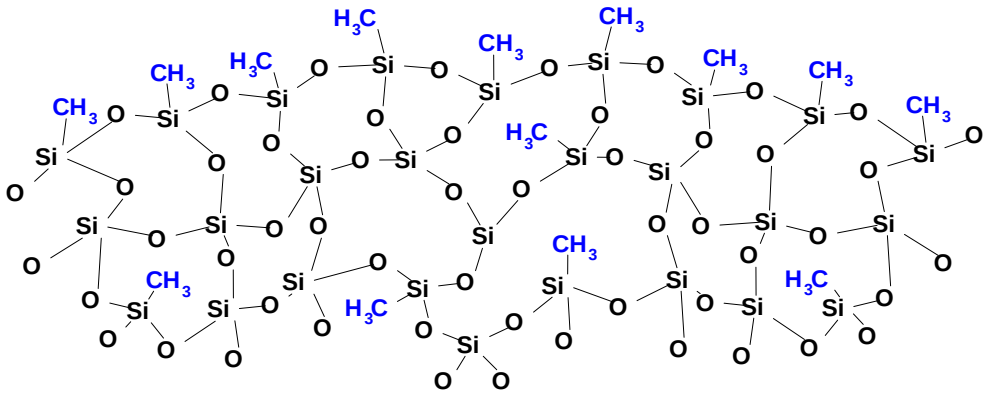

Fig. 2.1. Diagram of networked structure of SiOCH film.

The CVD SiOCH low-*k* films used in this study were fabricated from ringed siloxane compounds and molecular templates. The films have closed porosity and were ~28% porous with interconnecting pores of pore size ~2 nm, and a dielectric constant of approximately 2.35. In addition to siloxanes, the SiOCH have been deposited using various organosilicon sources, such as tetramethylsilane [3], trimethylsilane [7], and bis-trimethylsilylmethane [8].

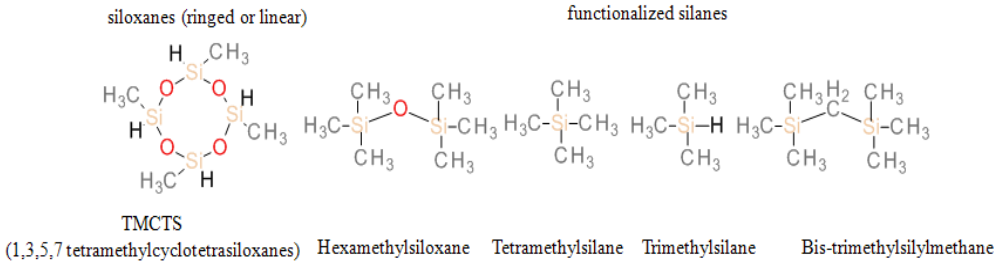

Fig. 2.2. Organosilicon sources for depositing SiOCH.

The aforementioned sources are suitable for the deposition of SiOCH because they contain a very strong bond between Si and alkyl groups (CH_n) [9]. The incorporation of

air or pores into these SiOCH thin films causes a reduction in the dielectric constant. This is because air has a dielectric constant of 1 so the more you have in, the lesser the dielectric constant is going to be. Bruggerman Effective medium approximation and Maxwell-Garnettare some of the spectroscopic ellipsometry models that are used for approximating the dielectric constant or refractive index based on porosity. Fig. 2.3 shows the relation between dielectric constant and porosity for OSG, CVD low-*k* (k=2.5 and 2.3) and a spin-on low-*k*. The "solid" models assume that the solid fraction of the low-*k* is like silica while the "microporous" models assume that solid is fractions are microporous (therefore their *k*~3 rather than 4).

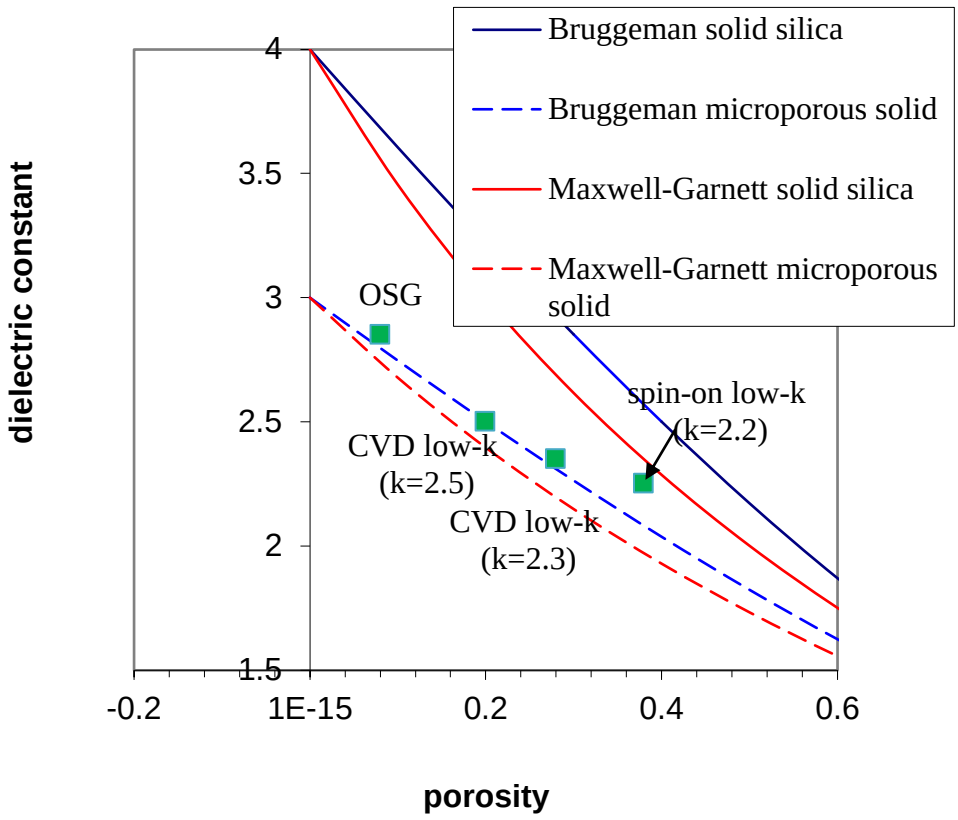

Fig. 2.3. Relation between dielectric constant and porosity for porous low-*k* films.

Grill et al. [10] prepared a SiOCH film which had dielectric constants between 2.8 – 2.05, by PECVD deposition using tetramethylcyclotetrasiloxane (TMCTS, $[MeHSiO]_4$, D_{4h}, $Si_4C4H_{16}O_4$) as the organic precursor; where Me is used to denote the methyl radical (CH_3). The unused organic fragments in the film are removed after annealing the deposited film, which then reduces the dielectric constant by creating pores in the material [10]. Specific pore-initiating compounds (porogens) can also be introduced into the process, and then removed during curing (see examples in Fig. 2.4 below).

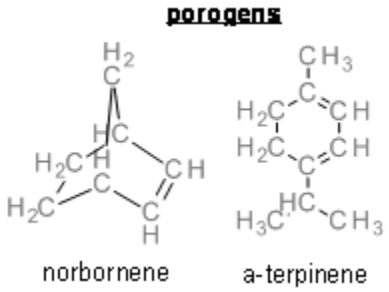

Fig. 2.4. Pore-initiating compounds (porogens).

They also reported that PECVD of TMCTS produces a highly cross-linked networked SiOCH film. Nagai et al. [11] also fabricated multilayered SiOCH films employing a layer-by-layer process of PECVD using a hexamethyldisiloxane (HMDSO) monomer source and O_2 plasma oxidation. They showed that, Si-O-Si bonds form the main network of the as-deposited film and methyl groups are bonded directly to the Si atoms. But after oxidation of the as-deposited film, the methyl groups bonding to the Si-O-Si main network were decomposed or reduced. Loss of methyls usually leads to an increase in density. This then reduces the density of the SiOCH film, hence reducing the dielectric constant. Yamaoka et al. [8] deposited SiOCH thin films by room-temperature PECVD

using tetraethoxysilane (TEOS). In their deposition, the films strongly depended on the radio frequency (RF) power as the films deposited at low RF power contained more alkyl (CH_n) groups. On the other hand, the number of silanol groups (O-H) decreased with RF power. Nevertheless, there is a disadvantage that the alkyl groups will dissociate from the TEOS precursor due to the weak bond of $O\text{-}C_2H_5$. But depositing at room temperature prevents the dissociation of alkyl groups from the precursor. They concluded that to deposit SiOCH by the PECVD method using TEOS, a combination of low substrate temperature and low plasma density is needed. The presence of methyl groups and/or hydrocarbons in these films makes them hydrophobic, and the films tend to have lower densities because of the breaking up of tetrahedral $Si\text{-}O_4$ tetrahedral. Hydrophobicity prevents the uptake of moisture and other harmful chemicals decreasing the dielectric constant compared to hydrophilic surfaces that allows the uptake of moisture.

2.1.2 Effects of Plasma Ashing on Low-*k* Films

In the back-end of line (BEOL) integration of semiconductor chips, plasma treatments are widely used. One of the major applications of plasmas in BEOL is the removal of photoresist and polymer residues after dry etching process. This is known as plasma ash [12]. Reactive-ion-etch (RIE) processes are one of the processes that have long been used to remove photoresist in ULSI processing [13]. SiOCH films because of the pores present have been found to be susceptible to significant damage caused by oxidizing plasmas [14,15] consequently there is the need for reducing plasmas and other processes. RIE plasmas using reducing gases such as N_2/H_2 and NH_3 have been found to have a lower impact on SiOCH films than the oxidative plasma. However, increased

porosity in these filmscan change how they react with different plasmas. Therefore, it is important to study the effects of different plasmas on SiOCH films. When low-*k* films are exposed to plasmas, the dielectric constant increases due to the absorption of moisture, degradation of the films morphology, reduction in films thickness/increase in density, and the loss of critical dimension [16]. Plasma treatment processes also result in complex combinations of chemical reactions between the surface species and the radicals formed in a discharge volume, and the physical impact of sputtering by ion bombardment [17]. Oxygen plasmas interact with SiOCH films can lead to a distortion of trench profiles [18]. A number of factors including the plasma composition, temperature and treatment time influence this process and determine etching rate, uniformity and selectivity as well as the extent of damage to the dielectric film. An increase in the dielectric constant is also due to the depletion of carbon atoms in the SiOCH films, which makes the films oxygen-rich (SiO_x) and induces silanol formation. Moreover the depletion of carbon causes the films to lose their hydrophobicity. Exposure of SiOCH films to O_2 plasma sources induces breaking of Si-CH_3 and CH_3 abstraction and other chemical changes via a diffusion-dominated mechanism-evidence that atomic oxygen is the major agent in plasma-induced carbon abstraction [19]. The radicals and ions in direct plasma usually shows a range of kinetic energies, but O radicals diffusing to the interior of a nanoporous material would eventually have a lower kinetic energy because of multiple wall collisions [20]. Calculations performed by Chaudhari et al. [20] reveal that, reactions that occur when O radicals collides with these films are hydrogen abstraction through OH radical or H_2O formation, carbon elimination through CH_3 radical formation and simultaneous

oxygen addition as bridged oxygen. With the downscaling of critical dimensions in ULSI circuits, the impact of plasma damage on electrical properties is expected to be more severe, as this can cause an increase in the leakage current. The undesired effects that oxygen plasma has on most low-*k* films calls for other resist strip techniques to be found, hence hydrogen plasma has been found to be a capable nominee for dry resist strip.

This prompted Shamiryan et al. [21] to investigate the interaction between conventional and highly porous SiOCH with tetrafluoromethane (CF_4), O_2, and H_2 plasma. They used two films; a highly porous SiOCH film which was 40% porous and having a *k* value of about 2.2 and a less porous film which was 19% porous and *k* value of 2.7. These were conducted at room temperature and it was found that, the CF_4 plasma etches the SiOCH films without modification to the bulk material, O_2 plasma oxidized the SiOCH film and converted the top layer to a hydrophilic SiO_2-like porous material, CF_4/O_2 plasma mixture had an optimal O_2 concentration at which the etch rate was maximal and H_2 plasma didn't react with the SiOCH film. Performing *in-situ* ellipsometric measurements on these films also showed no changes in the refractive indices and thicknesses of the films after hydrogen plasma treatments. Hydrogen plasma can thus be a promising candidate for photoresist stripping and has been found to have positive effect on hydrogen silsesquioxane (HSQ) [22] and methyl-silsesquioxane (MSQ) based low-*k* films. Wang et al. [23] deposited carbon-doped silicon oxide (CDO) using PECVD which had a *k* value of less than 2.9. They investigated the impact of oxygen plasma treatment on the quality of the low-*k* CDO films. This study affirmed the notion that, oxygen plasma causes damage to the CDO film by removing the entire carbon

content in the upper part of the film. This results in an increase in the *k* value and film thickness loss, even though atomic force microscopy (AFM) technique showed no changes in the topography of the low-*k* film after O_2 plasma treatment. All the films had a smooth surface with the root mean square surface roughness in the range of 0.6-0.8 nm.

In one of my earlier works [24], I investigated the effects of plasmas on porous low-*k* CVD SiOCH films using O_2, He/O_2, N_2/H_2 plasmas. A three dimensional atomic force microscopy (AFM) images of these films showed a dense arrangement of very fine surface topographies for the O_2 and He/O_2 plasma treated films while the N_2/H_2 treated films exposed smoother surface structures. The AFM results indicated that different plasmas have different effects on the SiOCH films, with the oxygen plasma causing amore adverse effect compared to the reducing plasma of N_2/H_2. This buttresses the point that Shamiryan et al. [19] made about oxygen plasmas causing more damaging effects on these low-*k* films than H_2 or other plasmas. Spectroscopic ellipsometry derived depth profiles of the films also revealed the N_2/H_2 plasma caused greater surface layer densification than that found in the O_2 plasma. Further studies on the effects of these different plasmas on the low-*k* SiOCH film is been explored in this work. Similar to O_2 plasma ash, N_2/H_2 plasma ash causes SiOCH films to lose their hydrophobic methyl groups. An interaction of the plasma species and the film then creates dangling bonds, converting the hydrophobic film surface to hydrophilic. As a result, atmospheric moisture diffuses into the damaged SiOCH film and this then causes an increase in the dielectric constant. N_2/H_2 plasma also interacts with the porous SiOCH films by collapsing some of these pores at the surfaces of the film. The collapse of these pores at the surface of the

film makes the films surface dense compared to the underlying bulk layer. This is what was observed by Hao Cui et al. [25] when they studied the impact of reductive N_2/H_2 plasma on PECVD porous low-dielectric constant SiCOH thin films having a dielectric constant of 2.5. After exposing these films to N_2/H_2 plasma, it was reported that the refractive index of the top layer increased but that for the underlying bulk films remained the same. This shows that the plasma caused the surface of the film to be densified. Significant reduction in film thickness was also observed by Cui et al. [23] after the plasma treatment. This reduction in thickness could be due to either the removal of film after the ashing process or film shrinkage, or a combination of both. It is suggested that film densification is caused by the interaction of chemicals between plasma ions and chemical bonds in the low-*k* film that results in pore collapse and, hence, an increase in films density. Therefore, the rate of densification is dependent on the depth of penetration of plasma ions into the film, and the penetration rate is expected to be greater for films with higher porosity. The effect of the plasma also causes changes in the films roughness. AFM studies conducted by Cui et al. [23] on low-*k* SiCOH films exposed to N_2/H_2 plasma showed the as-deposited film to have a very smooth surface with a root mean square (RMS) surface roughness of 0.41 nm while the ashed film had a higher RMS surface roughness of 2.72 nm. However, RMS roughness gradually decreased with increasing plasma exposure time. The initial increase in roughness was thought of to be as a result of the uneven film shrinkage as a result of densification, but at an increase exposure time, the films densification slows down and the film removal process due to the plasma becomes more dominant. The later process then tends to smooth the film

surface or homogeneously removes it. Therefore, if surface film densification is controlled, it could be used as a good pore-sealing technique, which has been demonstrated by Hoyas et al. [26] another way of limiting the effects of O_2 plasma on these low-k SiOCH films is the addition of He to the O_2 plasma forming He/O_2 plasma. Blaschta et al.[27] showed that, the admixture of He reduces shrinkage and *k* values are only slightly impacted.

2.2 Supercritical Fluids

With increased regulations on the use and release of toxic chemicals and the increased costs of solvents and water, the semiconductor industry have found it necessary to reduce the use of water and chemicals in their processes. This prompted increased research into incorporating supercritical fluids in main production processes. Carbon dioxide is of interest because it is:

1. Nontoxic
2. Nonflammable
3. Un-reactive under most conditions
4. Has easily accessible critical point (31.1 ^{o}C and 1170 psi, 73.8 bar)
5. Leaves no liquid waste
6. Low cost

Supercritical carbon dioxide have been successfully used in applications such as polymerizations [28], pharmaceutical applications [29], textile processing and dyeing [30], coatings [31], natural products/food extractions [32], specialized materials

fabrications [33], cleaning [34], and chromatography [35]. Even though supercritical carbon dioxide is been used in the aforementioned applications, it has only slowly gained interest in the semiconductor industry because it is been seen as novel in the context of semiconductor fabrications and capital costs.

When compounds are heated and pressurized above their critical pressure and temperature, the compound is neither a liquid nor a vapor it is in the fourth state [36] of matter known as supercritical state. Table 2.2 below shows the comparison of the physical data for the gaseous, liquid and supercritical states. It can be seen that, the properties of the supercritical state is in between the gaseous and the liquid states.

Table 2.2
Physical properties of gas, liquid, and supercritical fluid of typical organic fluid (order of magnitude) [37].

	Density (g/ml)	Diffusivity (cm2/s)	Dynamic viscosity (g/cm s)
Gas	1×10^{-3}	1×10^{-1}	1×10^{-4}
Liquid	1.0	5×10^{-6}	1×10^{-2}
Supercritical fluid	3×10^{-1}	1×10^{-3}	1×10^{-4}

Supercritical fluid is normally defined as the phase that is above its critical temperature, T_c and critical pressure, P_c. This is depicted in Fig. 2.4 below.

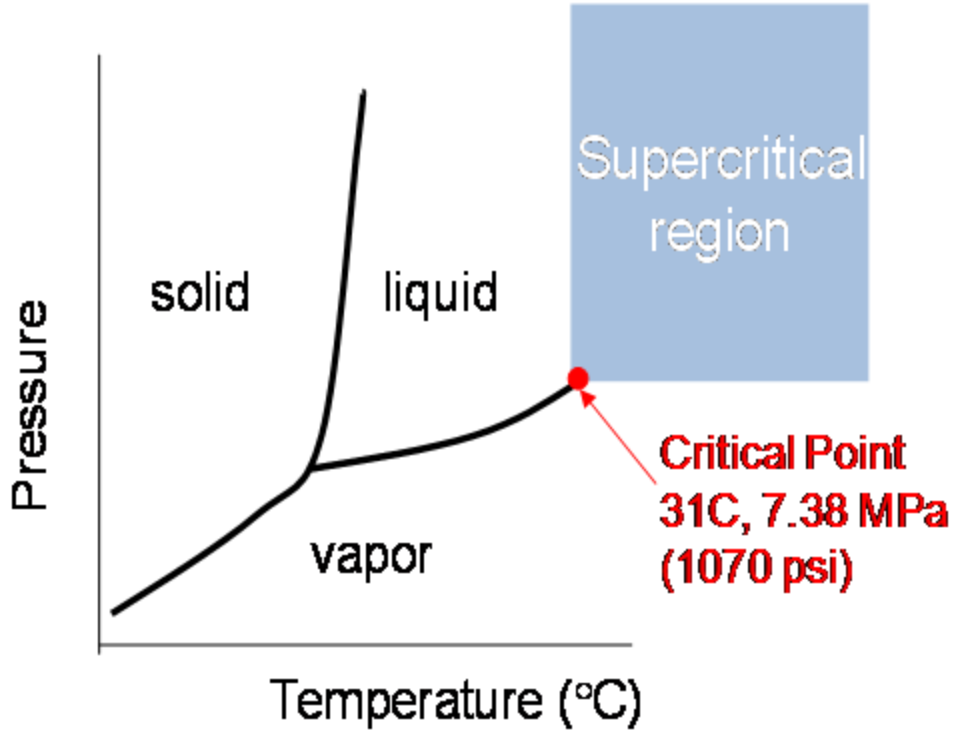

Fig. 2.5. Schematic representation of a phase diagram for carbon dioxide.

In the diagram, the areas where the substance exists as solid, liquid and gas are labeled. The triple point is where all three phases co-exist, and the critical point describes the conditions above where the material exists as a supercritical fluid and is neither liquid nor gas. As we move up along the gas-liquid equilibrium, both pressure and temperature increase. This causes the density of the liquid phase to decrease because of thermal expansion and the gas becomes denser because of increase in pressure. At the supercritical point, the densities of the two phases become identical and there is no distinction between liquid and gas (Fig. 2.6).

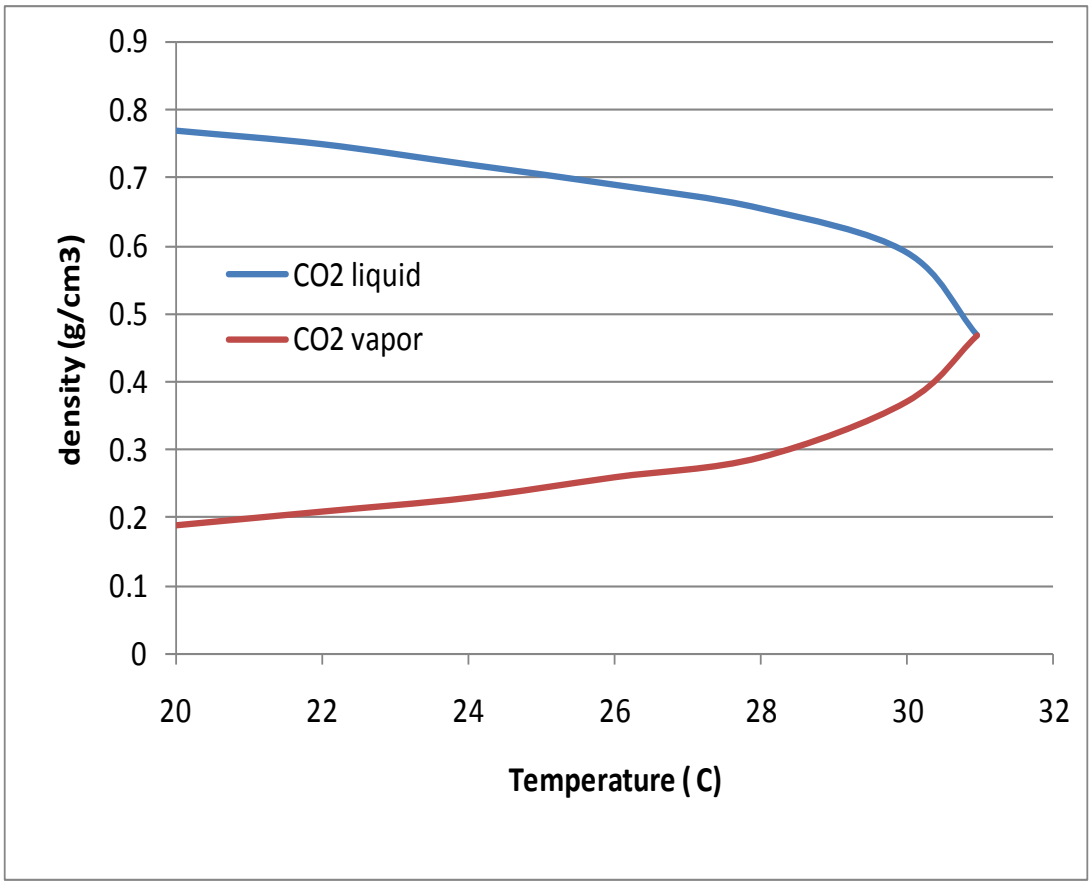

Fig. 2.6. Density of CO_2 liquid and vapor at super-critical point.

A supercritical fluid has gas-like transport properties of diffusivity and viscosity and near liquid properties such as density, rapid wetting and excellent penetration characteristics which makes it useful when processing low-*k* dielectrics. Supercritical carbon dioxide can dissolve non-polar solids; however, its solvating strength depends on the density, pressure, temperature and co-solvent. The zero surface tension of the SCF phase, another distinct advantage for manufacturing sub-micron features, allows complete wetting of complex substrates with intricate geometries. These attractive capabilities of supercritical

CO_2 (absence of surface tension, excellent mass-transfer phenomena, and controllable solvent quality) have been the driving force for many recent innovations [30].

In the semiconductor industry, supercritical carbon dioxide can be used as alternatives for photoresist removal and cleaning, as it offers many potential advantages over conventional organic solvents. With respect to inorganic materials, CO_2 is generally inert and hence will be compatible with a variety of substrates. Carbon dioxide pellet cleaning uses dry ice particles than larger snow for cleaning machined equipment, tools and parts. In contrast, supercritical CO_2 easily and swiftly penetrates fissures and boundary layers where snow cannot. Los Alamos's SCORR cleaning system was the first to show removal of hard-baked poly-methyl methacrylate (PMMA)-based resist from metalized Si without causing etching, pitting or undercutting of thin metallization patterns while regenerating CO_2 and solvent in a closed loop [38]. Viscosity and low surface tension of the fluid are the qualities that have for a long time prompted suggestions for supercritical fluid (SCF) initial wafer cleaning [39], aid in penetrating materials and removing contaminants. One of the selling points of super-critical systems is the ability to strip photoresist without damaging the underlying dielectric materials. With research focus shifting to the use of porous low-*k* materials such as SiOCH, polymeric or F-containing as ILD, this has become very important. This is because these materials are easily damaged by oxygen plasma or other types of plasmas during photoresist removal, unlike conventional SiO_2-type dielectrics.

Plasma causes damages to porous low-*k* thin films making the films lose their hydrophobicity as a result of the loss of carbon species. This mostly creates a hydroxyl

terminated surface. By using silylation agents in supercritical CO_2, it has been demonstrated that, the hydrophobicity of these films can be restored. The use of supercritical carbon dioxide fluid as a carrier for the silylation reagents thus reduces the consumption of chemicals and improves surface coverage.

2.3 Chemical Functionalization

Modification of plasma ashed thin film surfaces by the introduction of alkyl (-CH_3) groups to the films has shown to be an effective and important way of altering the way these thin films react with their surroundings and also changing the physical and chemical characterization of the films. This is done by silylating (functionalization) agents that have shown to recover surface hydrophobicity and also prevent water and precursor moieties from intruding into porous silica-based low-*k* films. Depending on the alkyl groups and the type of bonding present in these silylating agents, the effects of the recovery might be different.

2.3.1 Hexamethyldisilazane (HMDS) Functionalization

The use of different plasmas for different processes in the semiconductor industry; such as for photoresist removal and polymer residues renders the films hydrophilic as a result of the loss of hydrophobic methyl groups and the creation of hydroxyls on the film surfaces (Fig. 2.7).

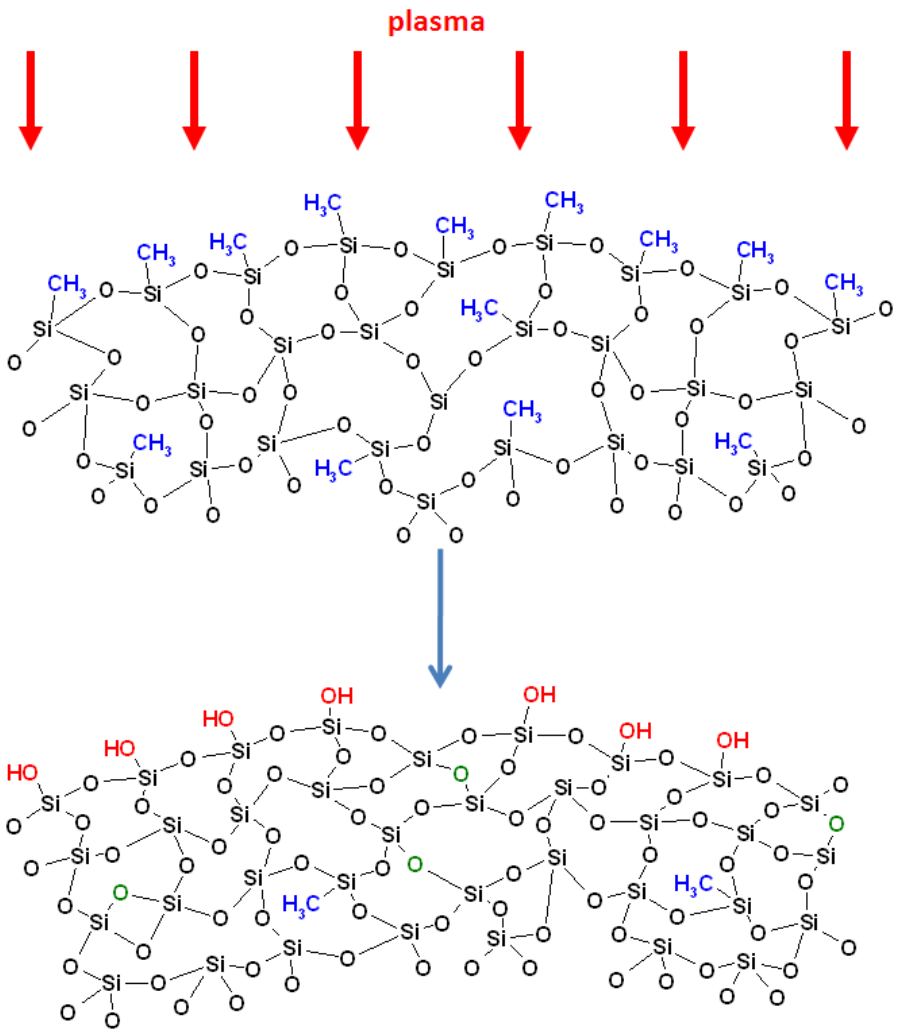

Fig. 2.7. Schematic of surface modification of low-*k* SiOCH film before and after O_2 plasma exposure.

Plasma when used on silica or silica-based films can create a hydroxyl terminated surface and, depending on the subsequent temperature treatments, the hydroxyl will exist as a vicinal (hydrogen-bonded silanol), germinal (two silanol group attached to the same silicon atom), or isolated (no hydrogen bonds possible) silanol sites [40] (Fig. 2.8).

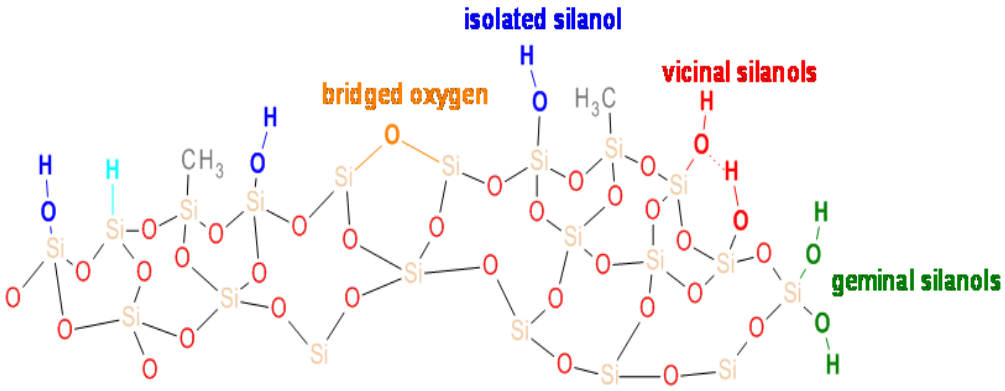

Fig. 2.8. Schematic representation of type of silanol groups occurring on silica surface.

The elimination of these created silanol groups and water from the surfaces of these films are accomplished by chemical modification of the silica surfaces created during plasma processing. The reactions that have mostly been used involve the removal of the surface hydroxyls with functionalizing agents such as HMDS [41] and trimethylchlorosilane (TMCS) [42]. Typically such reactions require a large amount of solvents and it can take reaction times up to 24 hours. With this in mind, the development of a process that uses a short reaction time and a small amount of solvent will be useful. Supercritical carbon dioxide (SC-CO_2) when used with a silylating agent such as HMDS has shown that it can rapidly and thoroughly silylates a plasma-damaged low-*k* surface [43]. Functionalizing a hydroxyl terminated surface with HMDS in SC-CO_2 is faster and very efficient when compared to liquid and vapor functionalization methods. Solvating properties of SC-CO_2 can be controlled by varying temperature, pressure and amount of co-solvents. The significant effects caused by the addition of small amounts of co-solvents have been attributed to the aggregation of the co-solvent about species of interest [44]. During the functionalization process, water is removed from the substrate and

because of the addition of the co-solvent (HMDS), it places hydrophobic trimethylsilyls on the films surface. SC-CO_2 is a two-step reaction and is shown below [45,46].

$$Si - OH + (CH_3)_3Si - NH - Si(CH_3)_3 \rightarrow Si - O - Si(CH_3)_3 + (CH_3)_3 - SiNH_2 \text{(Eq. 2.1a)}$$

$$(CH_3)_3 - SiNH_2 + Si - OH \rightarrow Si - O - Si(CH_3)_3 + NH_3 \uparrow \text{ (Eq. 2.1b)}$$

A schematic of HMDS/SC-CO_2 silylation process on a hydroxyl terminated porous low-*k* SiOCH film is showed below (Fig. 2.9).

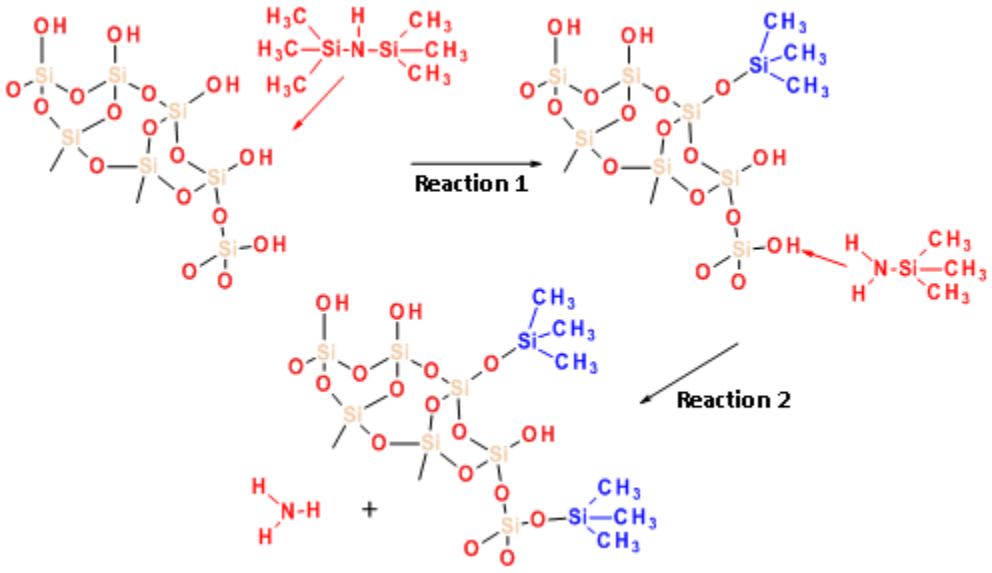

Fig. 2.9. Schematic of HMDS/SC-CO_2 silylation of plasma damaged porous low-*k* SiOCH film.

Gorman et al. [47] employed the use of SC-CO_2/HMDS to rapidly repair plasma damaged methylsilsequioxane (MSQ) based low-*k* dielectric material. In this work, using 1 volume percent of HMDS in SC-CO_2 and reacting for less than 5 minutes was able to rapidly repair the surface by recovering the contact angle (making the film hydrophobic). The water contact angle measurement increased from an initial hydrophilic value of

approximately 20° to recovered value of greater than 90°. Other groups have also shown this rapid reaction rate of silylating agents with silica surfaces in supercritical CO_2 [48]. The FTIR data for Gorman et al., showed significant amounts of water and silanol have been removed without readsorption upon exposure to ambient moisture. Subsequent spectroscopic ellipsometer measurements showed no significant change in thickness and refractive index, but a significant change in carbon concentration was observed after they measured the atom concentration using the XPS. Xie et al. [49] also performed silylation reactions using a super critical CO_2 solvent on MSQ films that has been exposed to oxygen plasma. But instead of using just HMDS which Gorman et al. did, their chemistries included HMDS, tetramethyldisilazane (TMDS), and trimethylchlorosilane (TMCS) mixed with SC-CO_2. FTIR analysis of their data showed that, HMDS, TMDS and TMCS all reacted with both H-bonded O-H groups (3150-3160 cm^{-1}) as well as isolated O-H groups (3740 cm^{-1}), hence a decrease in O-H peaks after silylation treatment. There was also a simultaneous increase in the C-H stretch of CH_3 at 2977 and 2922 cm^{-1} and Si-CH_3 peaks at 1279 and 839 cm^{-1}, which indicated the addition of trimethylsilyls (O-Si-$(CH_3)_3$) to the films surfaces. For their TMDS process, there was the presence of additional peaks at 2150 cm^{-1} which they assigned as a Si-H stretch [50], and at 910 cm^{-1}, which was attributed to the Si-H bending mode [51]. In this effect, it can be noted that, Xie et al. used HMDS, TMDS, and TMCS dissolved in SC-CO_2 to successfully silylate blanket ashed p-MSQ films which produced nearly hydrophobic surfaces with water contact angle measurements between 84-90°. The initial dielectric constant of the unashed blanket which was 2.4 was recovered to within 10% when they

used HMDS and TMCS. Similar results were obtained by Orozco-Teran et al. [52] when they used HMDS in SC-CO_2 as a recovery tool for plasma damaged low-*k* materials. In their work, after using HMDS and SC-CO_2 to recover oxygen damaged MSQ films, the resistance of these films to post-ash wet etch was improved. As discussed earlier on, there was also a reduction in the number of Si-OH bonds, and an increase in the hydrophobic $Si(CH_3)_3$ bonds. Water contact angle measurements also confirmed the partial recovery of hydrophobicity of these films. These results then suggest that precursors bearing Si without chemical groups that polarize are an effectual approach to repair oxygen ashed low-*k* MSQ films using SC-CO_2.

2.3.2 Diethoxydimethylsilane (DEDMS) Functionalization

Increasing interest in interlayer dielectrics low-*k* films calls for exploring the use of other solvents in SC-CO_2 as a recovery tool after the films have been plasma damaged. One such solvent worth exploring is the use of diethoxydimethylsilane (DEDMS) as a co-solvent in this process. DEDMS is of interest because of the presence of methyl groups in the chemical structure, which is showed in Fig. 2.10 below.

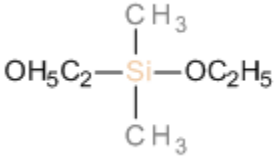

Fig. 2.10. DEDMS Chemical Structure.

DEDMS have been used in various processes, but not much work has been done with regards to using it as a functionalizing agent in recovering plasma-ashed damaged

surfaces. Casey et al. employed alkoxide silyation agents containing one to three methoxy groups dissolved in super-critical CO_2 to repair ash damaged low-*k* methylsilsesquioxane (MSQ) films [53]. Lenaerts et al. [54] used DEDMS to extract sol-gel material with polymer-like properties. Chi et al. [55] also employed DEDMS in the terminating effects of organosilane in the formation of silica cross-linked Micellar core-shell nano-particles. They employed DEDMS as a termination agent to inhibit the condensation of nano-particles. DEDMS has a stronger steric hindrance because of the presence of methyl groups, and hence it was able to improve the terminating effects. Thus, the presence of methyl groups in DEDMS makes it a viable candidate to be used in functionalizing plasma damaged films to introduce hydrophobic methyl groups on the films. But concerns still remain about the presence of $–OC_2H_5$. This is because $–OC_2H_5$ has a weak bond and hence there is the likelihood of the bonds been dissociated.

2.4 Effects of Temperature Treatments on Low-*k* Films

In efforts to reduce parasitic capacitances, materials with low dielectric constant have been the focus of investigation to be used as intermetal or interlayer dielectrics. For low-*k* films to be used in semiconductor device fabrication, these films need to have good electrical, mechanical, chemical and thermal properties. Hence, these materials should have a low dielectric constant while at the same time having a high thermal stability. Furthermore, techniques used in processing of these low-*k* films need to be compatible with existing processes. In previous research work, it has been found that lower *k* values can be achieved by reducing the plasma power and/or increasing the pressure of deposition, but this result in the film having a low or decreasing thermal stability [56].

This therefore calls for the development of a process which achieves a low-*k* material without compromising on its thermal stability. With this in mind, Yang et al. [57] performed work on the effects of post-deposition heat treatment on the properties of low dielectric constant films. In this work, they reported that post-deposition heat treatment could reduce *k* values while at the same time, increasing the thermal stability of plasma polymer thin films formed by the PECVD method using plasma polymerized decahydronaphthalene (PPDHN) as the organic precursor. These films were heat treated at 150 or 250 °C and after heat treatment, they observed no reduction in the film thicknesses. However, they observed that heat treatment higher than 300 °C caused the films to increase in *k* value when compared to the as-deposited films. The thermal stability of these films was investigated by measuring the thicknesses between, before and after annealing under argon ambient. At 150 °C, they observed that the *k* value decreased from 2.80 which were for the as-deposited to 2.52 while heat treatment at 250 °C decreased *k* from 2.80 to 2.63. As they increased the heat treatment temperature, PPDHN thin film showed increased thermal stability. The PPDHN film which was annealed at 250 °C showed only ~30% thickness reduction upon annealing at 400 °C. The changes in the *k* value and the thermal stability of these films were related to the changes in C-H, C=O, and O-H group densities present in the films. At higher temperatures, the PPDHN films showed lower density of O-H groups. Lower O-H groups means, lesser desorption of moisture and other deleterious chemical species, and hence increases in the film contact angles. Hence, post-deposition heat treatment can be considered as a useful method of further reducing the dielectric constant of low-*k* thin

films. In a similar work, Lee et al. [58] investigated the effect of annealing temperature on the properties of SiOCH films deposited by PECVD using a mixture of Si-O containing and hydrocarbon precursors, decamethyl-cyclopentasiloxane (DMCPSO-$C_{10}H_{30}O_5Si_5$) and cyclohexane (CHex-C_6H_{12}). This is a similar film that I used in this research work. In their work, they deposited SiOCH films which were annealed between 25 and 500 °C in ambient N_2 for an hour, 100 °C higher than the work of Yang et al. The as-deposited films had relative dielectric constant of 2.76 and 2.26. In their observation, an increase of annealing temperature to 450 °C caused the dielectric constant of these films to reduce to 2.31 and 1.85 respectively, but further increase to 500 °C caused the refractive index, hardness, and modulus to increase again. The film thickness retentions at annealing temperatures of 400, 450 and 500 °C were 90, 73, and 65% respectively. These changes in *k* value and thickness can be correlated to the FTIR data which showed a decrease in the intensities of the CH_x and Si-CH_3 peaks. This decrease in intensity of the CH_x groups and the Si-O cage structure in the SiOCH films can be interpreted as chemical changes in the films and led to lowering the dielectric constant, refractive index, hardness (decreased from 0.62 to 0.13 GPa) and modulus (decreased from 6.22 to 2.53 GPa) of the films, which was also reported by Grill and Neumayer [9]. In another work published elsewhere, Lee et al. [59] characterized ultra low-*k* SiCOH films (*k*=2.4) which were annealed under N_2 and O_2 ambient. In this work, they achieved a minimum dielectric constant of 1.85 for the N_2 (RTN) ambient and 1.98 for the O_2 (RTO) ambient after annealing. Hardness and modulus value of 0.44 and 3.95 GPa were achieved with the RTO process respectively. They attributed the enhancements in hardness and modulus

to oxygen incorporation in the Si-CH_3 structure. Processing time and thermal budget can thus be reduced to a minimum by using the annealing process when compared with furnace thermal process. In a different approach, Wong et al [60], rather than post-annealing their samples, deposited their SiOCH films at different substrate temperatures from 200 to 900 °C to observe the effects that it will have on the properties of the SiOCH low-*k* films. Their results indicated that lower refractive index and dielectric constant could be obtained at lower deposition temperatures, but the mechanical properties become poorer due to less degree oxidation and incorporation of more CH_3 bonds and Si-O cage structure into the film. Even though they were able to achieve films with low-k values and refractive index, post-deposition annealing process is better than pre-deposition substrate heating because the mechanical properties of the films are enhanced for post deposition annealing, and more CH_3 bonds and Si-O cage structure will be incorporated to the films during the deposition process.

In this work, a low-*k* SiOCH of dielectric constant ~2.3 (unashed) was used. This film was subjected to different plasmas of He/O_2 for 30s, O_2 for 20s and N_2/H_2 for 30 and 60s. These plasma damaged films were repaired using two silylation agents of HMDS and DEDMS in SC-CO_2 after which they were subjected to different temperature treatments between room temperature and 400 °C.

2.5 Ultra-violet (UV) Curing of Porous Low-*k* Films

In recent years, low-*k* films are under investigation to be used as interlayer dielectric films to replace the traditionally used SiO_2 films. In doing this, a viable low dielectric constant material should maintain sufficient mechanical properties to withstand

subsequent processing. Films with *k* values smaller than 2.7 cannot withstand chemical mechanical polishing (CMP) process for planarizing interlayer dielectric films; therefore, it is of great importance to enhance the mechanical strength of such films. Traditionally, thermal furnace treatments (at 450 °C) have been applied as the curing process for the films to remove unstable methyl groups in the films and also to remove porogens that makes the films porous. The thermal curing process also cures the matrix through the condensation of silanols and cross-linking mechanisms which has a positive impact on the mechanical properties of the film. However, the thermal budget in the BEOL is restricted, and curing temperatures are limited to $\leq$ 400 °C [61]. The conventional thermal curing process, appear to be insufficient in achieving a robust material with the suitable strength required for BEOL integration processes, hence, there is a need for alternative curing processes that have a low budget effect and only slightly increase the *k* value. To this effect, ultra-violet (UV) light irradiation on low-*k* films is currently under development in many laboratories. UV curing has been shown to enhance low-*k* mechanical properties while showing only a limited increase of dielectric constant. An advantage of the UV curing process is that the cross-linking and porogens extracting process can be enhanced just by increasing the intensity of the UV source.

Iacopi et al. [62] enhanced the mechanical properties of organosilicate glasses (OSG) at the expense of only minor densification by using a UV assisted cure. In doing so, they were able to enhance the elastic modulus of the film. Zenasni et al. [63] investigated the effects of UV assisted thermal cure on SiOCH spin-on ultra low-*k* materials as a substitute solution to the conventional thermal curing. They demonstrated

that UV thermal assisted curing makes a better porous film by removal of porogens, improved electrical properties as well as improved crosslinking, which was indicated by higher Si-O-Si bond density in their Fourier transform infra-red spectra when compared to that of the thermal cured film. Their FTIR data coupled with ellipsometric measurements show that the films cured using UV is more stable with a lower dielectric constant (k = 2.1) and no moisture uptake was observed. The calculation performed on the normalized Si-CH_3 absorbance peaks at 1275 cm^{-1} for different porous materials showed clearly that there was carbon depletion during UV cure. When compared to the Si-CH_3 for the thermal cured sample, it showed 0.32 and 0.26 for the UV assisted thermal cure FTIR respectively. But only few Si-CH_3 bonds are broken during UV assisted thermal cure, hence, this seems to be a more efficient way to cross-link the film matrix and to extract all porogens from the film. In electrical measurements that they performed, it showed that the breakdown voltage was also enhanced and leakage current was better in the case of UV assisted thermal cure, which can be possibly due to the presence of a minimal amount of silanols bonds. To this effect, they were able to demonstrate that, the UV assisted thermal cure has the ability of making a better porous film in terms of porogens removal, electrical properties and crosslinking degree. In another approach, Moore et al. [64] demonstrated that, controlled additions of O_2 to a N_2 ambient used in UV cure of low-k materials can increase the films modulus, hardness and shrinkage. They also showed that, the use of about 25-75 parts per million (ppm) O_2 in N_2 results in greater SiO cross-linking. In their study, they also realized that an addition of NH_3 to the N_2 ambient resulted in a mild retardation of cure which was due to the NH_3 absorption of

wavelengths critical for effective UV cure. Huang et al. [65] also developed a high performance porous low-*k* film of $k = 2.57$ using an advanced ultraviolet irradiation (UV curing) process. In their work, they reported some variations in bond structure changes of the porous low-*k* materials at different UV curing times. Their results also revealed that, the mechanical properties of the thin film can be efficiently strengthened which also causes a reduction in the dielectric constant. In their FTIR data, it was inferred that suboxide groups and Si-O-Si cage-like bonds are changed to Si-O-Si network structure bonds, which leads to an increase in the mechanical strength.

2.6 References

[1] J. Kim, H. Kim, H. Park, S. Hyun, Appl. Surf. Sci., 452 (2001) 169-170.

[2] International Technology Roadmap for Semiconductors 2007. Update.http://www.itrs.net/links/2007itrs/2007_Chapters/2007_Interconnect.pdf

[3] E. Vinogradova, E. Osei-Yiadom, C. E. Smith, D. W. Mueller, R. F. Reidy, Microelectronic Eng. 86 (2009) 176-180.

[4] K. Maex, M. R. Baklanov, D. Shamiryan, F. Iacopi, S. H. Brongersma, Z. S. Yanovitskaya, J. Appl. Phys. 93 (2003) 8793.

[5] A. Grill, V. Patel, J. Appl. Phys. 85 (1999) 3314.

[6] S. Lee, J. Yang, S. Yeo, J. Lee, D. Jung, J. Boo, H. Kim, H. Chae, Japanese J. Appl. Phys., 46-2 (2007) 536-541.

[7] M. J. Loboda, Microelectron. Eng. 50 (2000) 15.

[8] Y. H. Kim, S. K. Lee, H. J. Kim, J. Vac. Sci. Technol. A 18 (2000) 1216.

[9] K. Yamaoka, Y. Yoshizako, H. Kato, D. Tsukiyama, Y. Terai, Y. Fujiwara, Physica B376-377 (2006) 399-402.

[10] A. Grill, D. A. Neumayer, J. Appl. Phys. 94 (2003) 6697-6707.

[11] H. Nagai, M. Hori, T. Goto, T. Fujii, M. Hiramatsu, Jpn. J. Appl. Phys. Vol. 42 (2003) 2775-2779.

[12] Y. Li, Z. Tokei, J. V. Aelst, L. Carbonell, H. R. Baklanov, O. Richard, H. Bender, G. Groeseneken, K. Maex, Semicond. Sci. Technol. 22 (2007) 320-325.

[13] H. Cui, R. J. Carter, D. L. Moore, H. G. Peng, D. W. Gidley, P. A. Burke, J. Appl. Phys. 97 (2005) 11302-1-8.

[14] S. Ito, Y. Homma, E. Saski, S. Urichama, H. Morishima, J. Electrochem. Soc. 137 (1990) 1212.

[15] E. Kondoh, T. Asano, A. Nakashima, M. J. Komatu, J. Vac. Sci. Technol. B 18, (2000) 1276.

[16] T. C. Chang, P. T. Liu, Y. J. Mei, Y. S. Mor, T. H. Perng, Y. L. Yang, S. M. Sze, J. Vac. Sci. Techno. B 17 (1999) 2325.

[17] E. Taglauer, Appl. Phys. A 51 (1990) 238.

[18] D. Gray, M. Loboda, H. Struyf, M. Lepage, M. V. Hove, R. A. Donaton, E. Sleckx, Stucchi, F. Lanckmans, T. Gao, W. Boullart, B. Coenegrachts, M. Maenhoudt, S. Vanhaelemeersch, H. Meynen, K. Maex, Mat. Res. Soc., 612 (200) 651-657.

[19] M. A. Goldman, D. B. Graves, G. A. Antonelli, S. P. Behera, J. A. Kelber, (unpublished).

[20] M. Chaudhari, J. Du, S. Behera, S. Manandhar, App. Phys. Lett. 94 (2009) 204102-1-204102-3.

[21] D. Shamiryan, M. R. Baklanov, S. Vanhaelemeersch, K. J. Maex, J. Vac. Sci. Technol. B 20(5) (2002) 1923-1928.

[22] T. C. Chang, P. T. Liu, F. Y. Shih, S. M. Sze, Electrochem. Solid-State Lett.2 (1999) 390.

[23] Y. H. Wang, R. Kumar, X. Zhou, J. S. Pan, J. W. Chai, Thin Solid Films 473 (2005) 132-136.

[24] E. Vinogradova, E. Osei-Yiadom, C. E. Smith, D. W. Mueller, R. F. Reidy, Microelectronic Eng. 86 (2009) 176-180.

[25] H. Cui, R. J. Carter, D. L. Moore, H. G. Peng, D. W. Gidley, P. A. Burke, J. Appl. Phys. 97 (2005) 11302-11302-8.

[26] A. M. Hoyas, J. Schuhmacher, C. M. Whelan, J. P. Celis, K. Maex, Microelect. Eng. 76 (2004) 32-37.

[27] F. Blaschta, S. E. Schulz, T. Gessner, Microelect. Eng. 82 (2005) 427-433.

[28] J. L. Kendall, D. A. Canelas, J. L. Young, J. M. DeSimone, Chem. Rev. 99 (1999) 543–563.

[29] U. B. Kompella, K. Koushik, Crit. Rev. Thermal Drug Carrier Syst. 18 (2001) 173–199.

[30] G. A. Montero, C. B. Smith, W. A. Hendrix, D. L. Butcher, Ind. Eng. Chem. Res. 39 (2000) 4806–4812.

[31] K. Johns, G. Stead, (Eds.), Supercritical Fluids for Coatings—From Analysis to Xenon. A Brief Overview, Vol. 2, Kluwer Academic/Plenum Publishers, New York, NY, 1999.

[32] M. Sihvonen, E. Jarvenpaa, V. Hietaniemi, R. Huopalahti, Trends Food Sci. Technol. 10 (1999) 217–222.

[33] A. I. Cooper, Adv. Mater. 13 (2001) 1111–1114.

[34] J. McHardy, S. P. Sawan, Supercritical Fluid Cleaning Fundamentals, Technology and Applications, Noyes,Westwood, NJ, 1998.

[35] M. D. Palmieri, J. Chem. Educ. 65 (1988).

[36] G. L. Weibel, C. K. Ober, Microelectronic Eng. 65 (2003) 145-152.

[37] G. Manivannan, S. P. Sawan, J. McHardy, S. P. Sawan, (Eds.), Supercritical Fluid Cleaning: Fundamentals, Technology and Applications, Vols. 1-21, Noyes Publications, Westwood, NJ, 1998.

[38] J. B. Rubin, L. B. Davenhall, C. M. V. Taylor, L. D. Sivils, T. Pierce, Carbon dioxide-based supercritical fluids as IC manufacturing solvents, IEEE International Symposium on Electronics and the Environment, Danvers, MA, 1999.

[39] E. Bok, D. Kelch, K. Schumacher, Solid State Technol. 35 (1992) 117–120.

[40] T. W. Dijkstra, R. Duchateau, R. A. van Santen, A. Meetsma, G. P. A. Yap, J. Am. Chem. Soc., 124 (2002) 9856-9864.

[41] A. V. Rao, E. Nilsen, M. A. Einarsrud, J. Non-Cryst. Solids 296 (2001) 165.

[42] S. S. Prakash, C. J. Brinker, A. J. Hurd, J. Non-Cryst. Solids 190 (1995) 264

[43] R. A. Orozco-Teran, B. P. Gorman, Z. Zhang, D. W. Mueller, R. F. Reidy, Mat. Res. Soc. Symp. Proc. Vol. 766 (2003) E6.10.1-E6.10.6.

[44] J. Lu, B. Han, H. J. Yan, J. Supercrit. Fluids 15 (1999) 135-143.

[45] R. A. Orozco-Teran, "Functionalization and Characterization of Porous Low-*k* Dielectrics", Doctor of Philosophy, Materials Science and Engineering, University of North Texas, Denton, 2005.

[46] P. D. Matz, R. F. Reidy, Solid State Phenomena, V 103-104 (2005) 315-322.

[47] B. P. Gorman, R. A. Orozco-Teran, Z. Zhang, P. D. Matz, D. W. Mueller, R. F. Reidy, J. Vac. Sci. Technol. B 22(3) (2004) 1210-1212.

[48] C. Cao, A. Y. Faceev, T. J. McCarthy, Langmuir 17, (2001) 757.

[49] B. Xie, A. J. Muscat, Microelectronic Eng. 76 (2004) 52-59.

[50] E. A. Joseph, C. Gross, H. Y. Liu, R. T. Laaksonen, F. G. Celii, J. Vac. Sci. Techol. A 19 (2001) 2483-2489.

[51] H. Cui, J. Lu, I. Bhat, S. Murarka, W. Lanford, W. Li, Proceedings of IEEE International Interconnect Technology Conference, 2001, 45-47.

[52] R. A. Orozco-Teran, B. P. Gorman, Z. Zhang, D. W. Mueller, R. F. Reidy, Mat. Res. Soc. Symp. Proc. Vol 766 (2003) E6.10.1-E6.10.6.

[53] C. E. Smith, D. W. Mueller, P. Matz, R. F. Reidy, MRS Mater. Res. Soc. Symp. Proc. Vol. 914 © 2006 Materials Research Society 0914-F04-04).

[54] P. Lenaerts, E. Ryckebosch, K. Driesen, R. Van Deun, P. Nockemann, C. Gorller-Walrand, K. Binneman, J. of Luminescence 114 (2005) 77–84.

[55] F. Chi, B. Guan, B. Yang, Y. Liu, Q. Huo, Langmuir 26(13), (2010) 11421–11426.

[56] Y. C. Quan, J. Joo, D. Jung, Jpn J. Appl. Phys. 38 (1999) 1356.

[57] J. Yang, C. Shim, D. Jung, Jpn. J. Appl. Phys. 39 (2000) L 1324-L1326.

[58] S. Lee, J. Yang, S. Yeo, J. Lee, D. Jung, J. H. Boo, H. Kim, H. Chae, Jpn. J. of Appl. Phys. Vol. 46, No. 2, (2007) 536-541.

[59] S. Lee, D. Jung, J. Yang, J. H. Boo, H. Kim, J. Lee, H. J. Chae, J. Mater. Res., Vol. 23, No. 3, (2008) 856-861.

[60] T. K. S. Wong, B. Liu, B. Narayanan, V. Ligatchev, R. Kumar, Thin Solid Films 462-463 (2004) 156-160.

[61] V. Dharmadhikari, J. S. Sims, B. Varadarajan, S. Chang, D. Niu, K. Shrinivasan, Solid State Technol. 48 (3) (2005) 43.

[62] F. Iacopi, G. Beyer, Y. Travaly, C. Waldfried, D. M. Gage, R. H. Dauskardt, K. Houthoofd, P. Jacobs, P. Adriaensens, K. Schulze, S. E. Schulz, S. List, G. Carlotti, ActaMaterialia 55 (2007) 1407-1414.

[63] A. Zenasni, B. Remiat, C. Waldfried, C. Le Cornec, V. Jousseaume, G. Passemard, Thin Solid Films 516 (2008) 1097-1103.

[64] D. Moore, C. Waldfried, P. Sakthivel, O. Escorcia, Mater. Res. Soc. Symp. Proc. Vol. 1079 (2008) 1079-N02-04.

[65] C. H. Huang, H. L. Huang, C. I. Hung, N. F. Wang, Y. H. Wang, M. P. Houng, Jpn. J. App. Phys. Vol. 47, No. 3 (2008) 1532-1535.

CHAPTER 3

EXPERIMENTAL

3.1 Film Preparation

The CVD SiOCH low-*k* films used in this work were synthesized from ringed siloxane compounds and molecular templates. The films had a nominal thickness of 250 nm, a porosity of approximately 28%, and a dielectric constant of approximately 2.35 these films were exposed to 30s He/O_2, 20s O_2, and 30 and 60s N_2/H_2 plasma ash treatments. These films were obtained from SEMATECH. Prior to characterization measurements, the wafers were cleaved into multiple pieces. The as-received films were then characterized by the characterization techniques that are discussed later in this chapter. This was to check the initial properties of the films, before any further processes were performed on them.

3.2 Samples Characterization Techniques

A lot of characterization techniques have been established to be able to obtain useful information with regards to the properties of low-*k* materials. These properties include but are not limited to thickness, morphology, surface chemistry, functional groups present, wettability, porosity and refractive index. These properties are of much importance because they determine the distinctiveness and hence the application of these

low-*k* materials. The techniques that were used to characterize the films are: x-ray photoelectron spectroscopy (XPS), Fourier transform infrared spectroscopy (FTIR), variable angle spectroscopic ellipsometer (VASE), atomic force microscopy (AFM), and goniometer.

3.3 Fourier Transform Infrared Spectroscopy

3.3.1 Introduction and Fundamentals

Sir William Herschel was the first to discover infrared radiation in the 1800s, and since then there have been great deal of efforts to improve the measuring technique. The FTIR is commonly used for the identification of functional groups that are present in many samples such as, organic and inorganic compounds, thin films, gases, solids, liquids, powders, solutions, fibers, polymers, etc [1]. Fourier transform infrared spectroscopy (FTIR) uses a wide spectrum infrared (IR) source to identify, but are not limited to vibrational modes associated with chemical bonds in a substance, identifying functional groups, chemical bonds and also provides information about the vibrations modes of a molecule. When an infra-red source interacts with a molecule, the molecules have the tendency to either stretch, contract or bend, which are depicted in Fig. 3.1 below. These modes are stretching vibrations which consist of symmetric and asymmetric stretching vibrations. The other is the bending vibration modes which consist of scissoring, rocking, wagging, and twisting vibration modes. The first two are in-plane vibrations whereas the other two are out-of-plane vibrations. Hence, a chemical functional group tends to adsorb infrared radiation in a specific wavenumber range

regardless of the structure of the rest of the molecule. For infrared absorbance to take place, the energy of the light impinging on a molecule must equal a vibrational energy level difference within the molecule. This is summarized in Equation 3.1 below:

$$\Delta E_{vib} = hcW \text{ [2]} \qquad \text{(Eq. 3.1)}$$

where

$\Delta E_{vib} = vibrational\ energy\ level\ difference\ in\ a\ molecule$

$h = Planck's\ Constant\ (6.63 \times 10^{-34} Joule - second)$

$c = the\ speed\ of\ light\ \left(3 \times \frac{10^{10} cm}{second}\right)$

$W = wavenumber\ in\ cm^{-1}$

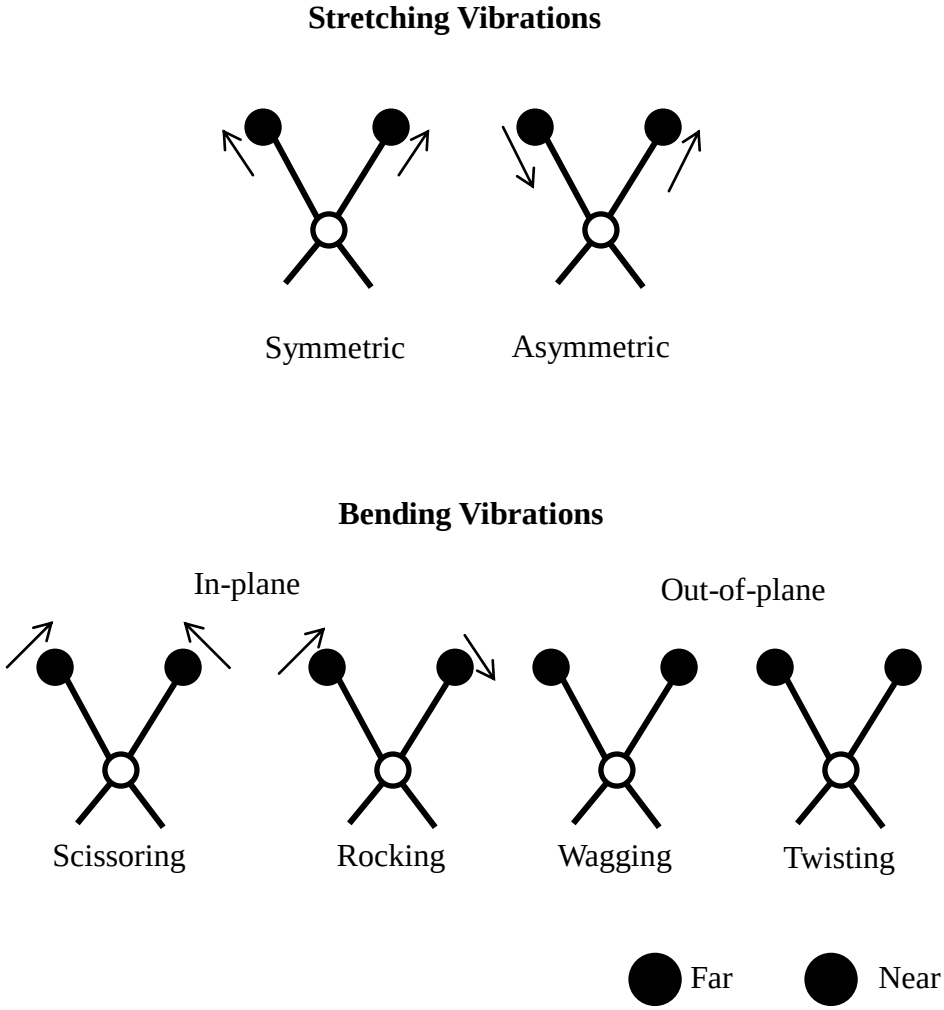

Fig. 3.1. Schematic representation of the different molecular vibration modes illustrating stretching and bending vibrations.Adapted from Christy et al. [3].

In infrared absorption, there are also allowed and forbidden transitions which are governed by a selection rule. The allowed transitions are those in which the vibrational quantum numbers changes by ±1 and the others are forbidden transitions. The symmetry of a molecule defines this selection rule and it states that "infrared light is absorbed when the electric dipole moment of a molecule changes as a whole in accordance with a molecular vibration" [3].

3.3.2 Instrumentation

The main components of the infrared spectrometer are the source, detector, beamsplitter, interferometer, and a computer where the Fourier transformation is performed. The Nexus 470 FT-IR was employed in this work.

The glowbar source is the most commonly used infrared source. This is made up of silicon carbide with metallic electrodes. For this source, when an electric current is applied to it, it creates heat of up to 1000 °C; hence the electrodes have to be cooled. The detector is the most important component of an IR spectrometer. The detectors are specially designed to measure the special interferogram signal. There are different types of detectors, but the commonly used are the thermal and photon detectors. As the name implies, the thermal detector detects the fluctuations of temperature from the sample, whiles the photon detector detects the production of free charge carriers in the sample due to the incoming IR radiation. Some of the detectors work under room temperature (e.g. deuteratedtriglycine sulfate (DTGS) with an alkali halide window which is a thermal type detector), whereas others need to cooled with liquid nitrogen (77 K) for it to operate (e.g. mercury cadmium telluride (MCT) which is a photon type detector).

The beamsplitter which is an optical device splits light passing through it into two (50%/50% ideally). Beamsplitters are normally made of silicon (Si), diamond, germanium (Ge) or iron oxide films which have been deposited on a transparent substrate like potassium bromide (KBr) or cesium iodide (CsI). For the mid-infrared region, Ge deposited on a KBr substrate is commonly used.

The interferometer is an important component of the infrared spectrometer. The principle of the interferometer used is based on the Michelson design, hence the name Michelson Interferometer, which measures the intensity as a function of the optical path. Infrared radiation from a radiation source is directed toward the Michelson interferometer. This collimated light is then incident on a beam splitter. An ideal beam splitter creates two separate optical paths by transmitting 50% of the incident light and reflecting the remaining 50%. The two beams produce interference when they are recombined. This recombined beam is then directed towards the sample and its rate of effective absorbance or transmittance is recorded, which is represented on the y-axis of the spectra produced by the FT-IR. The interferometer provides a means for the spectrometer to measure all frequencies simultaneously. The interferometer modulates the intensity of individual frequencies emitted by the sample. The beams are reflected from the surfaces of the two mirrors and recombine at the beamsplitter (Fig. 3.2). When the beams recombine, constructive or destructive interference occurs depending on the position of the moving mirror relative to the fixed mirror. When both beams are in phase, a constructive interference occurs creating a maximum peak and when they are out of phase, destructive interference occurs.

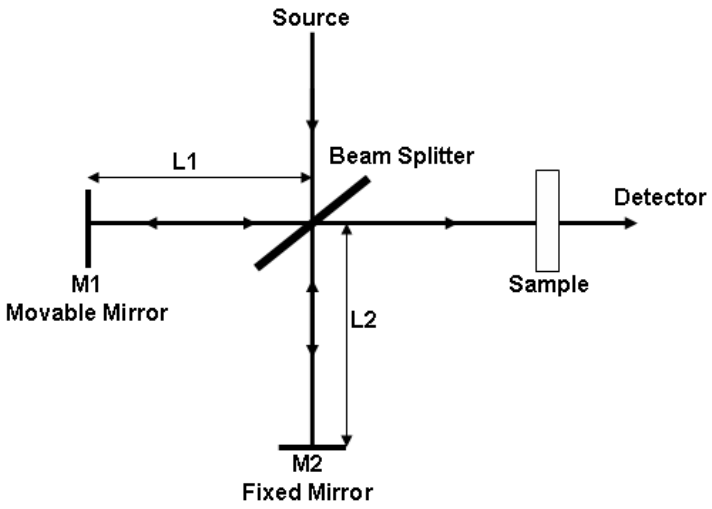

Fig. 3.2. Michelson Interferometer.

3.3.3 Techniques

The FTIR spectrometer is a dominant tool for infrared spectrometer because of the simplicity in the use and minimal sample preparation required, hence there have been the development of several techniques. The transmission technique is the most commonly used, where as other techniques requires reflection of the IR beam.

3.3.3.1 Transmission Method

In this technique, a parallel infrared beam passes directly through the sample. The FTIR actually measures the absorption of individual wavelengths passing through the sample. This absorption, which is normally reported as percent transmittance or absorbance, is representative of the energy transferred from the photons to the chemical bonds with complimentary vibrational modes. Absorbance is defined as [2]

$$A = log\left({I_o}/{I}\right) = -\log_{10} T \qquad \text{(Eq. 3.2)}$$

where A is the absorbance, I_o is the light intensity measured with no sample in the infrared beam (background spectrum) and I is the light intensity with a sample in the infrared beam (sample spectrum).

Transmittance is also defined as[2]

$$T = \left({}^{I}/_{I_o}\right) \qquad \text{(Eq. 3.3)}$$

The energy captured by the chemical bonds causes them to vibrate in a predictable fashion. This vibration may be described as a change in the inter-atomic distances known as stretching or a change in the angle between two bonds known as bending.

This technique possesses certain advantages namely; it requires little or no sample preparation before acquisition of a spectrum and it can also be used on solids, liquids, and gases. The only disadvantage is that samples thicker than 20 μm absorb a lot of infrared radiation and hence it is impossible to obtain a spectrum for thick samples. The optimal range for samples should be between from 1-20 μm [4].

3.3.3.2 Attenuated Total Reflectance (ATR)

An attenuated total reflectance technique is an internal reflectance method which measures the alterations that occur in a totally internally reflected infrared beam when the beam comes in contact with a sample (Fig. 3.3).

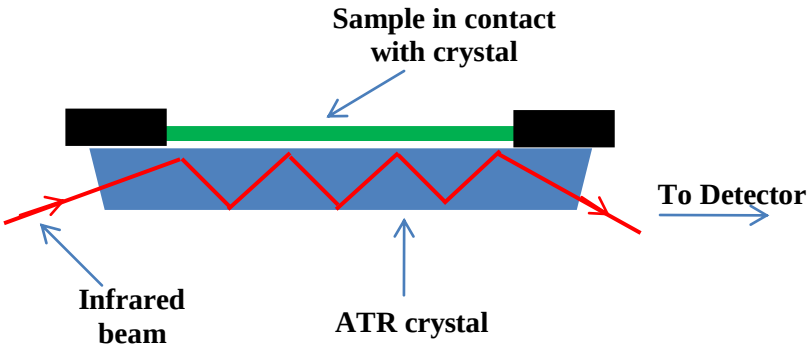

Fig. 3.3. A multiple reflection ATR system.

In this technique, an infrared beam is directed onto an optically dense crystal having a high refractive index, normally Si or Ge at a certain angle, and if the angle of incidence is greater than the critical angle, a total internal reflection is observed. The critical angle θ_c is defined as [5]

$$\theta_c = \sin^{-1}\left(\frac{n_2}{n_1}\right) \qquad \text{(Eq. 3.4)}$$

where n_1 *and* n_2 are the ATR crystal and the sample refractive index respectively.

This wave travels beyond the crystal and into the sample that is in contact with the crystal. The evanescent wave travels only a few microns (0.5 – 5 µm) [6] beyond the crystal surface into the sample, hence the need for a good contact between the sample and the crystal. The depth of penetration d_p is defined as [5]

$$d_p = \frac{\lambda_1}{2\pi\sqrt{sin^2\theta - \left(\frac{n_2}{n_1}\right)^2}} \qquad \text{(Eq. 3.5)}$$

where λ_1 is the wavelength of the light and θ is the angle of incidence.

This technique will be successful based on the following requirements; the sample must be in direct contact with the crystal and the refractive index of the crystal should be significantly greater than that of the sample for total internal reflection to occur.

3.4 X-Ray Photoelectron Spectroscopy (XPS)

3.4.1 Introduction and Fundamentals

X-ray photoelectron spectroscopy or electron spectroscopy for chemical analysis (ESCA) as it is normally known is based on the photoelectric effect [7,8], and it was developed in the mid-1960's by Kai Siegbahn and his research group at the University of Uppsala, Sweden [9]. This is a surface sensitive technique for the determination of elemental composition, chemical state analysis, empirical formula, and electronic state of a material. Some of the strengths of the XPS are [10]:

1. Can detect Li-U
2. Surface sensitive (10-100 Å sampling depth)
3. Sensitive to differences in chemical environment
4. Quantitative without use of standards
5. Manageable charging problems with insulators

XPS is a non-destructive technique in most cases, expect when doing a depth profile, and it owns this non-destructive nature to the fact that only the ejection of electrons is required for analysis. Unlike other techniques of elemental analysis, the atomic nuclei being examined remain unchanged during electron spectroscopic measurements. XPS is concerned with the ejection of an electron (photoemission) from a core level by an x-ray photon of energy *hv* (Refer to Fig. 3.4).

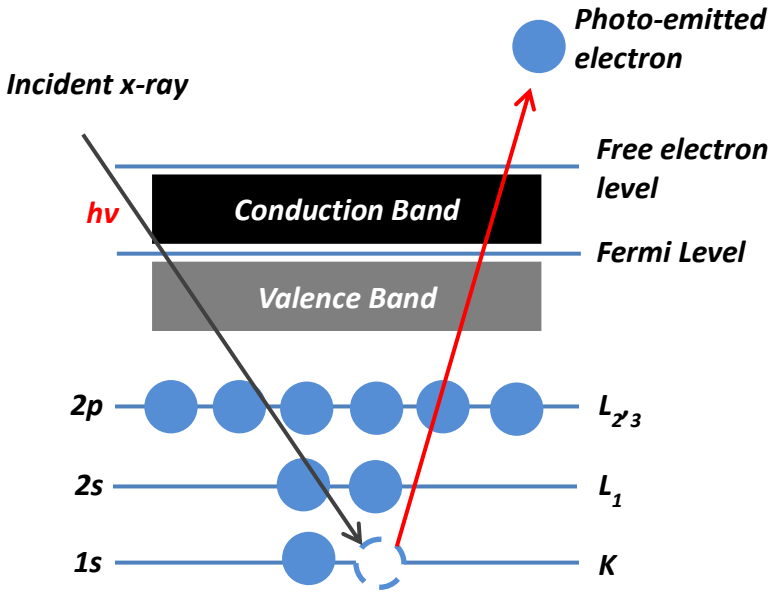

Fig. 3.4. Schematic diagram of the XPS process, showing the photo-electron effect.

Since the photoelectrons analyzed emanate only from the topmost atomic layers of the sample surface being studied (≤ 100 Å), the technique is an invaluable tool for studying interfacial phenomena at the solid-solid and solid-gas boundaries [11]. The energy of the emitted photoelectrons is then analyzed by the electron spectrometer. The kinetic energy (E_K) of the electron is the experimental quantity measured by the spectrometer, but this is dependent on the photon energy of the x-rays employed and is therefore not an intrinsic material property. The binding energy of the electron (E_B) is the parameter which identifies the electron specifically, both in terms of its parent element and atomic energy level. The relationship between these parameters is:

$$E_K = h\nu - E_B - \emptyset \qquad \text{(Eq. 3.6)}$$

where $\emptyset$ is the work function of the instrument which is the energy that the electron has to overcome to escape the surface.

X-ray photoelectron (XP) spectral peaks (generated by the photoelectrons) are named according to the orbital (l=0. 1. 2. 3… denoted as s, p, d, f…) and spin ($s = \pm 1/2$) quantum numbers of the core levels from which they emanate. The total momentum of the photoelectrons($J = l \pm s$) is included in the nomenclature of a measured XP spectral peak (e.g. $Ca2P_{3/2}$, where $l + s = 1 + 1/2 = 3/2$). In the XPS instrument, all the kinetic energy of all collected electrons are measured, including the contributions of photoelectron and Auger electron lines, which are as a result of an ejection of a valence level electron whose kinetic energy is independent of the photon energy.

XPS is well suited for both quantitative and qualitative elemental analysis which can be obtained from a collected XPS spectrum. This is achieved by measuring the peak intensities which is an approximate number of the atoms of a specific element present. The atomic concentration of an element *D, C_D*, can be calculated by [12]

$$C_D = \frac{\left(\frac{I_D}{S_D}\right)}{\Sigma\left(\frac{I_n}{S_n}\right)} \qquad \text{(Eq. 3.7)}$$

where I_D is the area of the most intense peak of element D, S_D is the sensitivity factor, and (I_n/S_n) is the ratio of the elements present. In well-calibrated XPS systems, the precision of the quantitation measurements is typically within ±5%; thus, XPS is well suited for both quantitative and qualitative elemental analysis. The distribution of chemical composition of materials greater than 50 Å or the normal acquisition depth of an XPS can be attained by performing a depth profile acquisition. In this, sputtering

process is employed by removing layers of the material as a result of ion bombardment on the film. Normally, argon (Ar) ion gun is used to sputter off layers from the film.

3.4.2 Instrumentation

XPS is basically consisted of a sample mount system, x-ray source, electrostatic charged-particle energy analyzer, and an electron detector contained in an ultra high vacuum (UHV) system. An optional argon ion gun is usually added, which is used for sputtering; to clean samples before data acquisition or to remove layers of the films when performing a depth profile analysis.

In choosing a material for a soft x-ray source, the following conditions needs to be considered:

1. The line width must not limit the energy resolution required in the technique,
2. The characteristic x-ray energy must be high enough, that a sufficient range of core electrons can be photo-ejected for an unambiguous analysis,
3. Since the photo-ionization cross-section of electron in different core levels varies with the wavelength of the x-ray, a suitable characteristic x-ray wavelength is crucial to obtain a strong enough photo-electron signal for analysis.

The most commonly used x-ray anodes in XPS are either magnesium (Mg) or aluminum (Al) with energies 1253.6 and 1486.6 eV [13] which corresponds to wavelengths of 0.989 and 0.834 nm respectively. Table 3.1 below also gives parameters of other available x-ray sources.

Table 3.1
Energy and line width for different x-ray sources [14].

Material	Radiation	Energy (eV)	Line Width (eV)
Mg	K (alpha)	1253.6	0.7
Al	K (alpha)	1486.6	0.85
Zr	L (alpha)	2042.4	1.6
Ag	L (alpha)	2984.3	2.6
Ti	K (alpha)	4510.9	2.0
Cr	K (alpha)	5417.0	2.1

With the aluminum source, monochromatic aluminum *k*-alpha x-rays are usually produced by diffracting and focusing a beam of non-monochromatic x-rays off of a thin disc of natural, crystalline quartz with a <1010> orientation. To provide protection of the sample from scattered electrons from the anode, heating and contamination effects, a 2 μm thick Al foil has to be inserted between the anode and the sample [15].

The heart of the XPS technique is the measurement of an electron energy spectrum. To measure this, an electron energy analyzer is often employed. This is also called a spectrometer. An electron spectrometer has the ability of directing and focusing the ejected electrons from the sample surface under x-ray excitation. These electrons are then filtered, energy selected (or velocity-selected) by the spectrometer. Hence a handful of electrons having the desired energy range is collected and detected by the detector. There have been a lot of analyzers designed for use in an XPS, but the commonly used types are the double-pass cylindrical mirror analyzer (DPCMA) and the concentric

hemispherical energy analyzer (CHA). The commonly used is the CHA and it is made up of two metal hemispheres, one of which is a concave shape whiles the other is a convex shape. They are concentric hemispheres hence their centers of curvature are coincident. In between these two is an electric field which is created as a result of placing different voltages on each of the spheres. When electrons are injected into the gap, they are attracted to the bottom (positive applied voltage) and repelled from the top one (negative applied voltage). Hence, only electrons having the specific energy called the pass energy is able to get to the detector.

The common detectors that are used in XPS are channeltrons, microchannel plates, and restrictive anode plates. These detectors increase the signal of the individual electrons that strike the detector so they can be detected. The detector is located at the exit point of the analyzer slit, and it is made up of several single detectors which are linked into a computer. The spectrum is then plotted and displayed on a computer.

3.5 Ellipsometry

3.5.1 Introduction and Fundamentals

Ellipsometry is a well-established and a very sensitive measurement technique that employs polarize light to characterize thin films, surfaces, and material microstructure. The use of ellipsometry was primarily limited due to the intricacy of the equations and lack of computing power. By the use of more powerful computers lately, its data acquisition is efficient and accurate, allowing analysis of more complex structures. Ellipsometry is usually used to characterize not only thin films, but bulk

materials too. The most common application is measurement of thin film thickness and optical constants. It has also proven to be the primary technique for determining optical constants in the UV, visible, and IR wavelength ranges. It has also been used to determine [16]:

- Optical constants (n, k or ε_1, ε_2)
- Doping concentration
- Surface and interfacial roughness
- Alloy ratio
- Crystallinity
- Optical anisotropy
- Depth profile or material properties
- Growth or Etch rate (in-situ)
- Temperature (in-situ)

A variety of films can be analyzed using this method, such as but not limited to, single films, multi stacked (layered) films, rough surfaces, interfaces, and mixtures of different materials [17].

Ellipsometry measures the change in polarization when the beam of polarized light is reflected from (or transmitted through) the surface of the film, as depicted in Fig. 3.5.

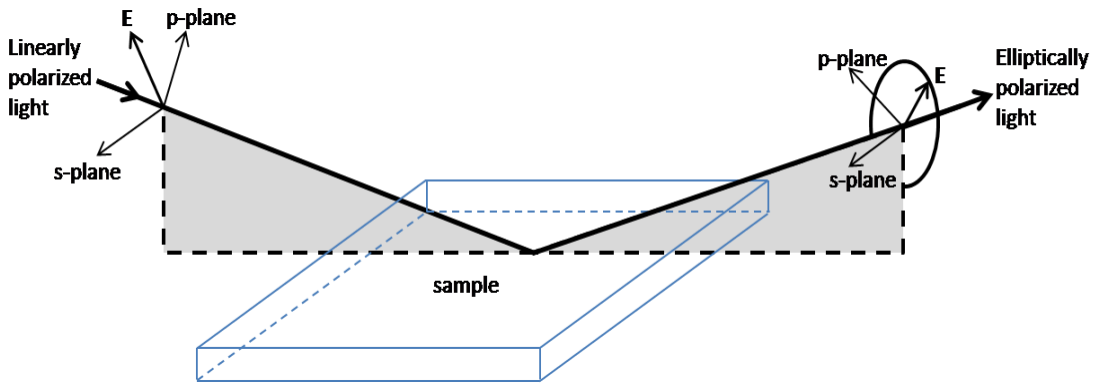

Fig. 3.5. Geometry of an ellipsometric experiment. Adapted from "Guide to Using WVASE32 Spectroscopic Ellipsometry Data Acquisition and Analysis Software" [18].

Basically, ellipsometry deals with the measurement of the polarization state of a light beam. However, a description of an "optical system" that changes the polarization state of a beam of light is what we get when we perform ellipsometric measurements. The measured values in ellipsometry of the reflected light are expressed as psi (Ψ) and delta (Δ), where Δ is the change in relative phase difference between the perpendicular and parallel components of the incoming and outgoing wave, and

$$\Delta = \delta_{inc} - \delta_{out} \qquad \text{(Eq. 3.8)}$$

Ψ is the amplitude ratio of the parallel and perpendicular components whose possible values can be between 0 and 90 degrees, R^p and R^s are the reflection coefficients of the parallel and perpendicular components [19].

$$\tan \Psi = \frac{R^p}{R^s} \qquad \text{(Eq. 3.9)}$$

Ψ and Δ are related to the ratio of Fresnel reflection coefficients R^p and R^s for p- and s-polarized light, respectively

$$\rho = \frac{R^p}{R^s} = \tan(\Psi) e^{i\Delta} \qquad \text{(Eq. 3.10)}$$

Because the ratio of two numbers is measured by the ellipsometry technique, it makes the technique highly accurate and very reproducible. The ratio is a complex number, which also contains "phase" information (Δ), hence the measurements are very accurate. But at times, the accuracy of the measurements depends on the type of model being used for the particular sample.

3.5.2 Instrumentation

The optical components used in ellipsometers are light source, optical fiber, beam modulator, polarizer, retarder or compensator, and a detector as depicted in Fig. 3.6.

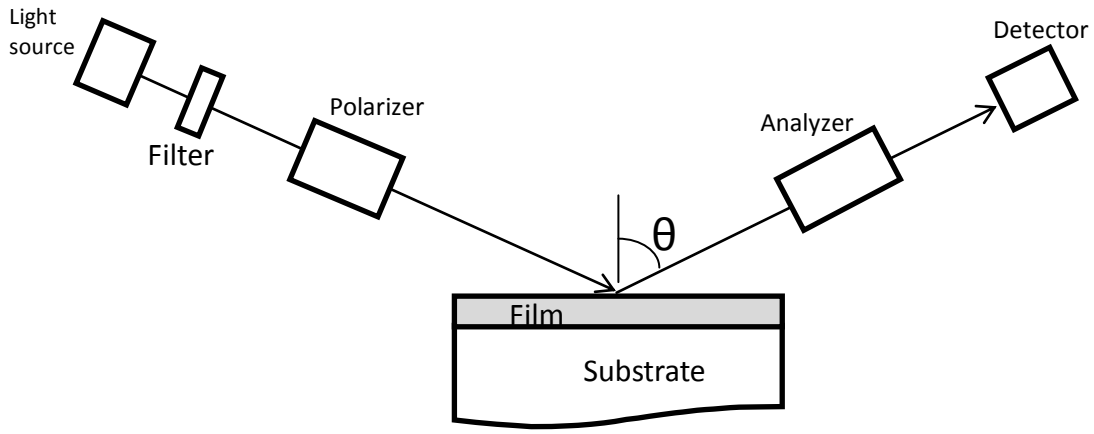

Fig. 3.6. Schematic diagram showing the main components in an ellipsometer. Adapted from Runyan [20].

Spectroscopic ellipsometers need a broad spectral output to match the needed range of measurements, unlike single-wavelength ellipsometers which uses laser sources. In other to cover these wavelengths from the vacuum ultraviolet to the infrared, the following sources are utilized [19]:

Table 3.2
Table of different spectroscopic ellipsometer light sources and their wavelengths.

Light Sources	Wavelengths
Deuterium (D_2) lamp	140 nm – 300 nm
Xenon (Xe) lamp	190 nm – 2 μm
Quartz Tungsten Halogen (QTH) lamp	350 nm – 2 μm
Silicon carbide glowbar	1.5 μm – 40 μm

The light source would be very stable (i.e. constant intensity vs. time) ideally, and should show roughly a constant output as a function of wavelength over the required spectral range, but such sources do not exist.

The purpose of using optical fibers is to couple the light beam between optical elements. These fibers usually have a diameter of 200-900 μm. There are two types of fibers; a UV transmitting fiber and an IR fiber. The UV transmitting fiber shows good transmission deep into the UV end of the spectrum, but they have a strong absorption band around 1340-1450 nm, and hence they are usually not used in the spectral region, whiles the IR fibers do not transmit much light below ~300 nm, but transmit throughout the near-IR region [19]. Beam modulators are used to harmonically modulate the intensity of the light beam, for subsequent synchronous detection.

Of all the optical components, the most important one for making ellipsometric measurements is the polarizer. A polarizer is used to convert any light beam into linearly polarized light oriented along the transmitting axis. Hence a polarizer will ideally transmit light polarized in one direction say horizontal direction but will not transmit any

light polarized along the perpendicular direction. As can be seen in Fig. 3.6 above the second polarizer acts as an analyzer, and its function is to determine the extent of polarization by measuring the degree of polarization of R^p/R^s.

The compensator or retarder converts linearly polarized light into elliptically polarized light. A retarder also introduces a phase delay between perpendicular linear polarizations (the perpendicular components of the electric field of the beam) [18]. Retarders are harder to work with than polarizers, but they tend to be very useful. In some cases, compensators are used, which can change linearly polarized to circularly polarized light.

The detector is used to measure the intensity of the light received after it reflects off the sample's surface. In ellipsometry, three different kinds of detectors are commonly used, namely: photodiodes, diode-arrays, and photomultiplier tubes [18]. When the signal reaches the detector, it is then measured and the resultant data is then analyzed to obtain psi (Ψ) and delta (Δ).

3.6 Contact Angle

3.6.1 Introduction and Fundamentals

The goniometer is a tool that is used to measure the contact angle (both static and dynamic), surface tension, and surface energy of a sample. Contact angle is of interest not only because they are a manifestation of the surface tension that the solid undergoes when placed in contact with a drop of solvent or water where the contact angle is formed, but also because they dictate the strength of interaction and wettability of the particular

solid. The measurements of contact angle have been used extensively to determine the surface hydrophobicity of solids. The basic way of measuring the contact angle is by finding the tangent of the liquid droplet placed on the surface of a solid material, as depicted in Fig. 3.7 below.

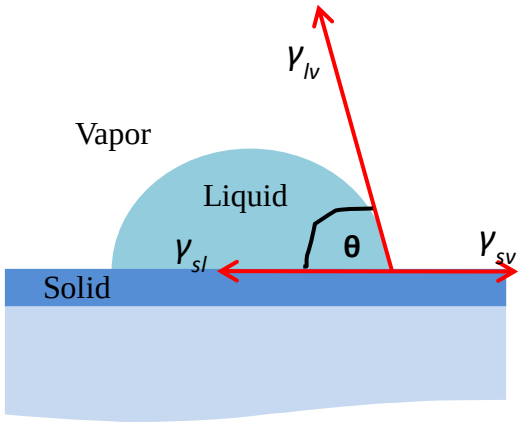

Fig. 3.7. Schematic representation of the contact angle formation when a fluid drop is put in contact with a solid surface. This also illustrates the three interfacial tensions: solid-vapor,$\boldsymbol{\gamma_{sv}}$, solid-liquid, $\boldsymbol{\gamma_{sl}}$ and liquid-vapor, $\boldsymbol{\gamma_{lv}}$.

The contact angle, θ can also be defined as a measure of the wetting of a solid by a liquid. It is the measure of the angle formed by a liquid at the three phase boundary of the solid, liquid and vapor (Fig. 3.7). A lower θ (θ < 90°) value indicates a wetting or hydrophilic surface, which also means that there is great adhesiveness between the liquid and the solid and also the solid has a high surface free energy, whiles a high θ value (θ > 90°) indicates a hydrophobic surface or non-wetting surface and a low surface free energy [21].

When a liquid drop is placed on top of a solid surface, there are basically two forces that determine how the liquid will interact with the solid surface. These forces are the cohesive and the adhesive forces. The higher the adhesive force, the more wide the

liquid will spread across the solid surface and cohesive force is the vice-versa, where the liquid is repelled from the solids surface. The spreading of the drop increases the contact area between the solid and the liquid thereby reducing the contact angle, making the solid surface hydrophilic. If the liquid-solid interface is favored over the vapor-solid interface, a complete wetting occurs, whiles on the other hand, if the surface tension dominates; only a partial wetting occurs [22].

The Young's equation [23,24] is a well-regarded equation that was established by the scientist Thomas Young, and this equation defines the balances of forces caused by a wet drop on a dry surface. By applying this equation, we are able to determine the surface tension form the contact angle.

$$\cos\theta = \frac{\gamma_{sv} - \gamma_{sl}}{\gamma_{lv}} \qquad \text{(Eq. 3.11)}$$

where θ is the Young contact angle and three interfacial tensions are: solid-vapor, γ_{sv}, solid-liquid, γ_{sl} and liquid-vapor, γ_{lv}. In this equation, it is assumed that the solid surface is smooth (i. e. an ideal surface), but in reality such an ideal surface does not exist. This has prompted other researchers to look into the Wenzel [25] and Cassie-Baxter [26] states, which is to be considered in the case of super-hydrophobicity. In these states, topography and roughness can be measured and used to better describe and envisage apparent contact angle and relative repellency.

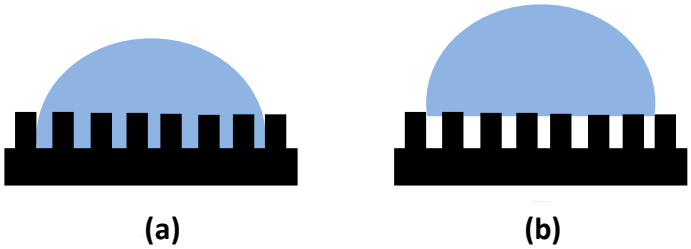

Fig. 3.8. Illustration of the Wenzel state (a) and Cassie-Baxter state (b).

The Wenzel state (Fig. 3.8 (a)) predicts that even though the surface is not smooth, the liquid in contact with the solid infiltrates the voids below the liquid and hence occupies more surface area. This is governed by the equation:

$$\cos\theta^* = r\cos\theta \qquad \text{(Eq. 3.12)}$$

where $\cos\theta^*$ is the contact angle at the rough surface, $\cos\theta$ is the Young's contact angle, and r is the roughness coefficient. But in the Cassie-Baxter state (Fig. 8 (b)), it is assumed that the liquid drop rests on the asperities on the solids surface and the voids are filled with air. The equation that predicts this state is:

$$\cos\theta^* = f_1\cos\theta_1 + f_2\cos\theta_2 \qquad \text{(Eq. 3.13)}$$

where $f_1$is the surface area fraction of one material with contact angle θ_1, and f_2 is the surface area fraction of the second material with contact angle θ_2. If f_2 represents the area fraction of trapped air then we know that the contact angle on a liquid drop on air would be 180° we can set $\cos\theta_2$ equal to 1, and since the $f_1 + f_2 = 1$ the equation becomes

$$\cos\theta^* = f_1\cos\theta_1 + (1 - f_1)\cos 180° \Rightarrow \cos\theta^* = f_1\cos\theta_1 + f_1 - 1 \qquad \text{(Eq. 3.14)}$$

Even though, the Wenzel and the Cassie-Baxter states were not used in this research, it is worth to mention.

3.6.2 Instrumentation

Goniometer is the instrument that is used to measure not only the contact angle (both static and dynamic) but the surface tension, and surface energy of a sample. The main components of this instrument are a camera, an illuminator lamp, illuminator power supply, a micro syringe, a sample stage, and lateral and vertical adjustment controls. Fig. 3.9 shows a representation of the Ramè-Hart Model 250 Standard Goniometer which has an accuracy of ±.10° that was used in this work. There is also a computer screen where the measured contact angle is seen and data analysis performed.

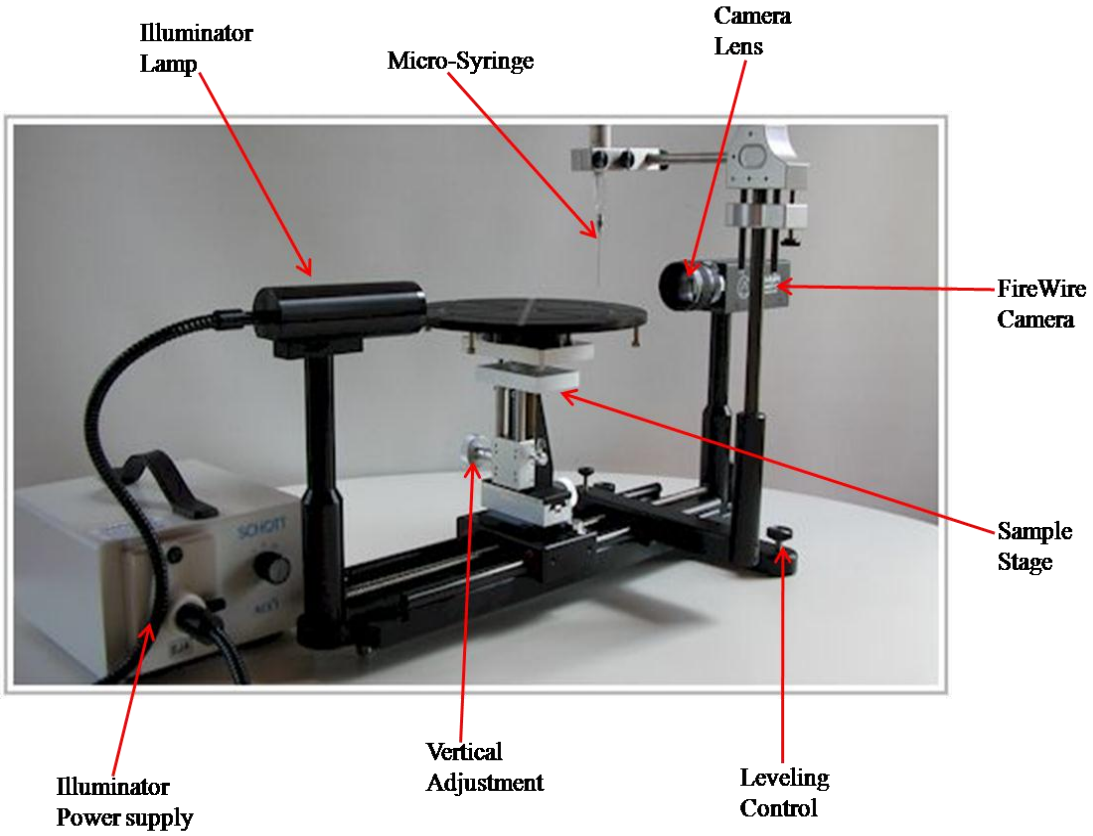

Fig. 3.9. Ramè-Hart Model 250 Standard Goniometer.

The illuminator power supply is used to control the illuminator lamp to adjust the proper illumination level, which helps in getting a good contrast on the darkly outlined defined drop image against a white background. The micro-syringe provides an approximately 2 mm diameter sessile drop through a manually operated capillary needle. The sample to be measured is placed on the sample/specimen stage. A level stage facilitates precise positioning of the liquid droplet to be measured. The vertical adjustment and the lateral adjustment (not shown) are used to correctly adjust the height and the position of the sample and liquid droplet so that it can be well illuminated by the illuminator lamp and also be seen by the camera. The camera captures an image of the sessile dropped liquid, automatically transports it to the computer, and it is then analyzed.

Because of the sensitivity of the measurement, the contact angle goniometer instrument should be positioned away from any possible source of vibration, windows, doors, and fans. Once the liquid is dropped on the sample, the measurement needs to be taken as soon as possible to avoid evaporation of the liquid.

3.7 Atomic Force Microscope (AFM)

3.7.1 Introduction and Fundamentals

The AFM is a very high-resolution type of scanning probe-microscope that has a resolution on the order of fractions of a nanometer. This implies that the AFM can analyze and characterize samples at the microscope level. The AFM was invented by Gerd Binning in 1986 to overcome a limitation of the AFM's predecessor, the scanning

tunneling microscope (STM). The limitation of the STM was that it could only image materials that could conduct a tunneling current.

AFM functions by allowing an extremely fine sharp tip attached to the micro-scale cantilever to come into contact or very close contact to a sample being imaged. This tip usually is just a few microns long. The tip is positioned at the free end of a cantilever. The sample to be characterized is positioned under the tip, and different forces attract or repel the tip thereby making the cantilever to be deflected. A laser is used to measure this deflection by bouncing off the top surface of the cantilever onto a four element diode (Position sensitive photo diode, Fig. 3.10).

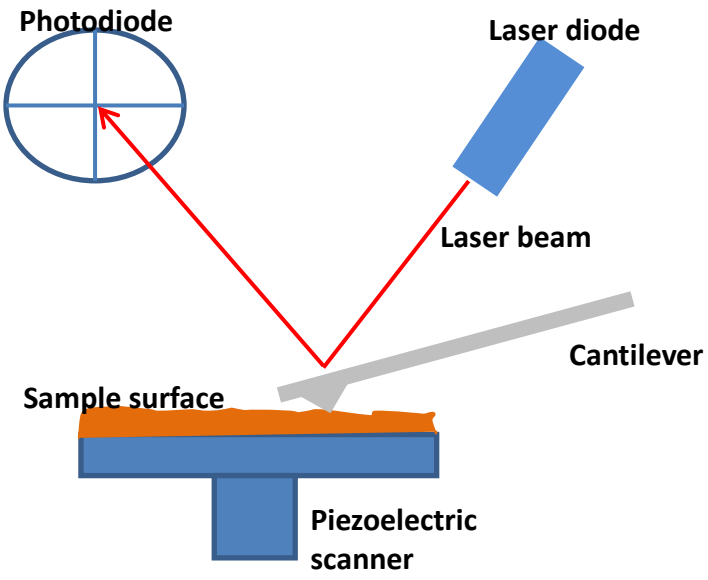

Fig. 3.10. A schematic of an AFM.

In normal operation, the force between the tip and the sample is held constant by a computer controlled feedback loop that examines the force i.e. the bend of the cantilever and signals the piezoelectric scanner whether to move the sample closer or farther away

in order to maintain the set bending of the cantilever. The cantilever is deflected according to Hooke's law (equation 3.15).

$$F = -kx \qquad \text{(Eq. 3.15)}$$

where *F* is the force, *k* is the spring constant and *x* is the cantilever deflection.

There are different types of microscopy instruments in use, namely the scanning electron microscope (SEM), transmission electron microscope (TEM), and the optical microscope, just to name but a few. The AFM is different from these because of the presence of interactive forces between the sample and the tip. The most associated force with AFM is an interatomic force called the Van der Waals force. Fig. 3.11 shows the relationship between the van der Waals force and the distance between the tip and the sample.

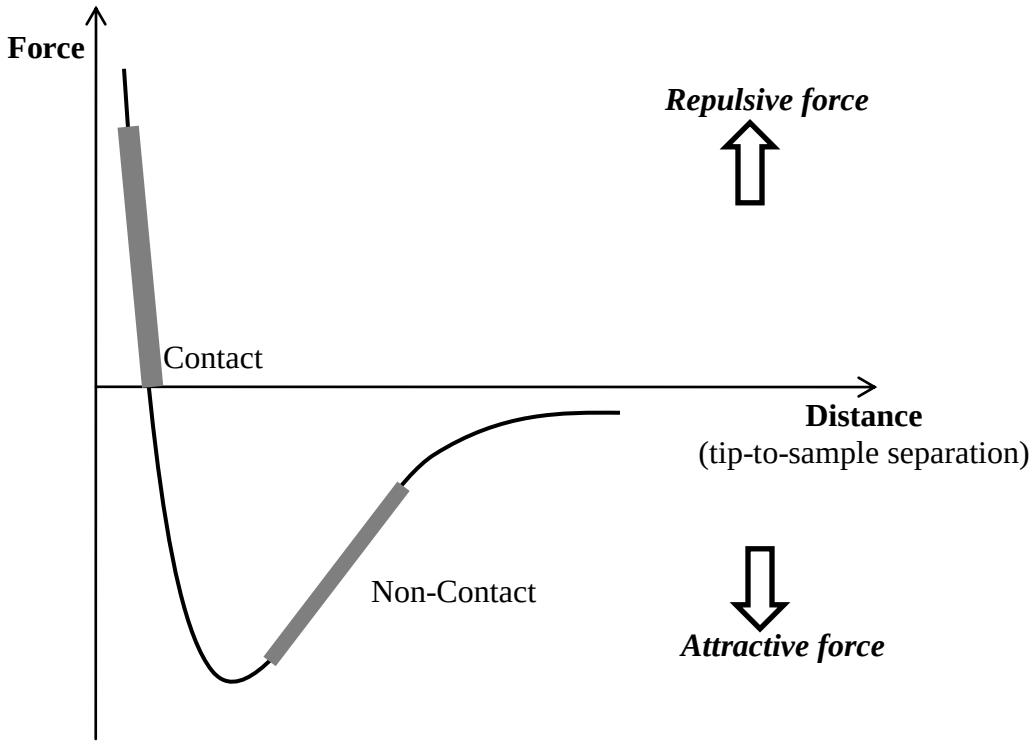

Fig. 3.11. Force vs. distance showing contact and non-contact modes.

The region labeled contact represents a mode of AFM measurement which is the contact mode, where the cantilever is held less than a few angstroms away from the samples surface. In this mode, the interatomic force between the cantilever and the sample is repulsive. This imaging mode is able to achieve lattice resolution with adequate noise isolation. In the non-contact region, the tip and the sample are 10-100 Å apart, and the force is considered attractive. The tapping mode analyzes the sample by making use of both the contact and non-contact region, fluctuating between the two. The main difference between these two modes of data acquisition is the amplitude of the oscillations, tapping mode uses amplitude of 20-100 nm, while the non-contact uses amplitudes of less than 10 nm [27]. For the purposes of this research, tapping mode was used to obtain topographical features of the samples. The advantages to using the tapping mode are [27]:

- Higher lateral resolution on most samples (1 nm to 5 nm).
- Lower forces and less damage to soft samples imaged in air.
- Lateral forces are virtually eliminated, so there is no scraping.

The only disadvantage is the slightly slower scan speed when compared to the contact mode.

3.7.2 Instrumentation

The main components of the AFM are the micro-cantilever, stage, electronic controller, computer and the laser source.

The laser source reflects on the back on the cantilever and sends signals to the photodiode (detector). The cantilever with a tip at the free end is the force sensor. Usually, silicon probes are used for tapping mode in AFM data acquisition. This is because the silicon probes are quite stiffer thereby resulting in larger force constants and resonant frequencies.

The computer contains the software for capturing images and data analysis. Whiles the electronic controller generates electronic signal that controls all functions on the stage.

The stage (Fig. 3.12) includes the scanner, optical microscope, sample stage and the photodiode. Within the scanner, we have the piezoelectric crystal which moves the sample back and forth beneath the probe. As the scanner moves back and forth, the sample moves with it under the stationary probe and the x, y, and z position of the probe is recorded.

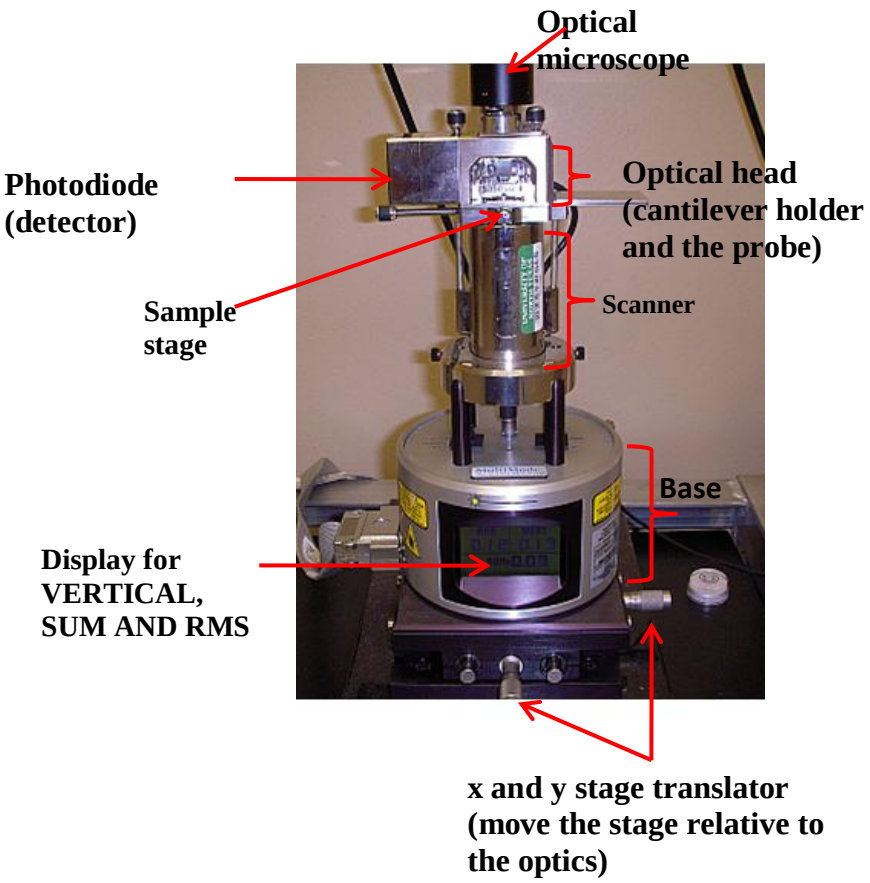

Fig. 3.12. Stage of the Veeco (Digital Instruments) Multimode Nanoscope III.

3.8 References

[1] B. Stuart, W. O. George, P. S. McIntyre, Modern Infrared Spectroscopy, Edited by D.J. Ando, England, John Wiley& Sons Ltd, 1998.

[2] B. Smith, Infrared Spectral Interpretation: A Systematic Approach, CRC Press, 1999.

[3] A. A. Christy, Y. Ozaki, V. G. Gregoriou, Modern Fourier Transform Infrared Spectroscopy, New York, Elsevier, 2001.

[4] G. Socrates, Infrared Characteristic Group Frequencies, Tables and charts, 2nd Edition, England, John Wiley & Sons Ltd, 1994.

[5] N. J. Harrick, Internal Reflection Spectroscopy, USA, John Wiley & Sons, 1967.

[6] FT-IR Spectroscopy – Attenuated Total Reflectance (ATR), Perkin Elmer Life and Analytical Sciences. 2005.

[7] H. Hertz, Ann. Physik 31 (1887) 983.

[8] A. Einstein, Ann. Physik 17 (1905) 132. 1921 Noble Prize in Physics.

[9] K. Siegbhan, Nova ActaRegiae Soc. Sci., Ser. IV, Vol. 20 (1967).1981 Nobel Prize in Physics.

[10] V. Bojan, X-Ray Photoelectron Spectroscopy and Auger Electron Spectroscopy, MCL Open House, 2007.

[11] C. C. Chusuei, D. W. Goodman, Encyclopedia of Physical Science and Technology, 3rd Edition, Vol. 17, Academic Press (2002).

[12] S. Nasrazadani, I. Fritsch, C. S. Henry, "Analytical Techniques for Materials Characterization." In Advanced Electronic Packaging, edited by W.D. Brown, New York, 1999.

[13] C. R. Brundle, “X-Ray Photoelectron Spectroscopy” In Encyclopedia of Materials Characterization, edited by Brundle, C. R., Evans, C. A. Jr, Wilson, S., Massachusetts, Butterworth-Heinemann, 1992.

[14] J. C. Vickerman, Surface analysis – the principal techniques, John Wiley & Sons (1997).

[15] H. Bubert, J. C. Rivière, “Photoelectron Spectroscopy” In Surface and Thin Film Analysis: A Compendium of Principles, Instrumentation, and applications, edited by Bubert, H., Jenett, H., Federal Republic of Germany, Wiley-VCH, 2002.

[16] J. A. Woollam, Co., Inc., Guide to using WVASE 32, 2001.

[17] B. Gruska, A. Röseler, “UV-Vis-IR Ellipsometry” In Surface and Thin Film Analysis: A Compendium of Principles, Instrumentation, and applications, edited by Bubert, H., Jenett, H., Federal Republic of Germany, Wiley-VCH, 2002.

[18] J. A. Woollam, Co., Inc., Guide to using WVASE 32, 2001.

[19] J. A. Woollam, Manual of Ellipsometry, version 3.3.

[20] W. R. Runyan, Semiconductor Measurements and Instrumentation, McGraw-Hill Book Company, 1975.

[21] D. Li, A. W. Neumann, “Thermodynamic Status of Contact Angles” In Applied Surface Thermodynamics, Surfactant Science Series, edited by Neumann, A. W., Spelt, J. K., New York, Marcel Dekker, Inc., 1996.

[22] S. A. Safran, Statistical Thermodynamics of Surfaces, Interfaces, and Membranes, USA, 1994, Addison-Wesley Publishing Company.

[23] K. L. Mittal, Ed., Contact Angle, Wettablilty and Adhesion Vol 2. Utrecht: VSP BV, 2002.

[24] R. J. Stokes, D. F. Evans, Fundamentals of Interfacial Engineering New York: Wiley-VCH, 1997.

[25] R. N. Wenzel, Industrial & Engineering Chemistry, 28 (1936) 988-994.

[26] A. B. D. Cassie, S. Baxter, Transactions of the Faraday Society 40, (1944) 546-551.

[27] SPM Training Notebook; (Copyright 2003 Veeco Instruments Inc.), 8-13.

CHAPTER 4

EFFECTS OF PLASMA TREATMENTS ON POROUS LOW-*K* CVD SIOCH FILMS AND ITS REPAIR USING SUPERCRITICAL CO_2

4.1 Introduction

Low-*k* dielectric films are one of the performance drivers to back end of line (BEOL) integration. These films are needed in microelectronic device interconnects to lower power consumption and minimize cross talk between metal lines. Low-dielectric (*k)* materials currently in production for the 45 and 65 nm nodes are most often organosilicates glasses (OSG) with dielectric constants near 2.8 and nominal porosities of 8-10%. The next generation of low-*k* materials require *k* values 2.3 and below 4 for the 32 nm device generation and beyond [1]. To effectively achieve these dielectric constants, pores must be introduced into these organosilicate matrices. However, porosity in a material reduces its mechanical strength and increases its active surface area, thus, making these films vulnerable to plasma damage and to moisture adsorption when film is rendered hydrophilic.

Porous carbon doped oxide dielectrics (SiOCH) have been widely studied as promising materials for interlayer dielectric applications in multilevel interconnect architectures; however, their porosities have created integration challenges [2]. The high

surface area of these porous materials makes them susceptible to water adsorption and potentially harmful chemical species during device fabrication increasing the dielectric constants [3]. In standard integration processes, different plasmas are used to remove photoresist and to etch patterns. Post-plasma cleaning processes for low-*k* layers are needed to remove photoresist, reveal features, eliminate contamination trapped in pores, remove copper, and repair patterning damage [4]. Plasma treatment processes result in complex combinations of chemical reactions between the surface species and the radicals formed in a discharge volume, and the physical impact by ion bombardment [5]. Interaction of reactive plasmas with SiOCH materials causes carbon depletion that induces silanol formation, film densification and dangling bonds defects, concomitantly, increasing the film dielectric constant [6]. Elimination of the water and silanol from these high surface area materials can be accomplished by chemical modification of the silica surfaces created during plasma processing. Silylating agents such as trimethylchlorosilane (TMCS) [7,8,9] or hexamethyldisilazane (HMDS) [10] have been used to replace surface hydroxyls.

Densified fluids heated and compressed to near or above their critical temperature and pressure have solvating properties that are comparable to liquids and have mass transfer characteristics comparable to gases making them promising candidates for wafer cleaning applications on both the front and back end of line [11]. Super-critical CO_2 has been investigated for cleaning porous materials [12], removing photoresist [13], drying to prevent pattern collapse [14], and repairing plasma damage to low-*k* films [15,16,17]. Supercritical-CO_2 provides an excellent means of transport into and out of porous media

because of its gas-like diffusivities and near liquid densities. In this chapter, I have examined the nature of the plasma damage incurred by these ashes and then studied how the repair processes differ for each ashed film.

4.2 Experimental

The CVD SiOCH low-k films used in this work were synthesized from ringed siloxane compounds and molecular templates. The films had a nominal thickness of 250 nm, a porosity of ~28%, and a dielectric constant of approximately 2.35. The films were exposed to 30 sec He/O_2, 20 sec O_2, and 30 and 60 sec N_2/H_2 plasma ash treatments. Prior to characterization measurements, the wafers were cleaved into multiple pieces. Samples from each of the plasma conditions were subsequently treated with supercritical CO_2 containing HMDS for 5 minutes. Different pieces of these samples were also treated with SC-CO_2 containing diethoxydimethylsilane (DEDMS). The super-critical reactor is a cylindrical design with a 2.5 inch inner diameter and a length of about 6.5 inches. Super-critical (SC) experiments in this study were conducted at 1900 psi (9.6 MPa) and 40 ^{o}C.

Following exposure to the supercritical fluids, de-ionized (DI) water of resistivity 18.2 MΩ-cm and diiodomethane (DIM) contact angle measurements were taken using a sessile-drop goniometric technique on a Ramè-Hart goniometer. Contact angle measurements of the as-received samples were also conducted. Atomic force microscopy (AFM) was employed to measure changes in surface roughness after ashing. Nexus-470 Fourier transform infra-red (FTIR) spectrometer was used to verify the changes in bond chemistry of the films. Changes in film densities, thicknesses and refractive indices, (at

632.8 nm wavelength) were measured using a JA Woollam Variable Angle Spectroscopic Ellipsometer (VASE). Film surface chemistries and depth profiles were studied using an X-ray Photoelectron Spectrometer (XPS) PHI 5000 Versa probe.

4.3 Results and Discussion

4.3.1 AFM Analysis

Three-dimensional AFM images of the SiOCH films treated by the various gas plasmas are represented in Fig. 4.1 these were analyzed using WSxM 4.0 Beta 1.3 software [18] over scanning area of 1 μm^2. The blanket sample (Fig. 4.1a) shows a fine network of structure which forms a smooth surface with R_{rms} of 0.382 nm.

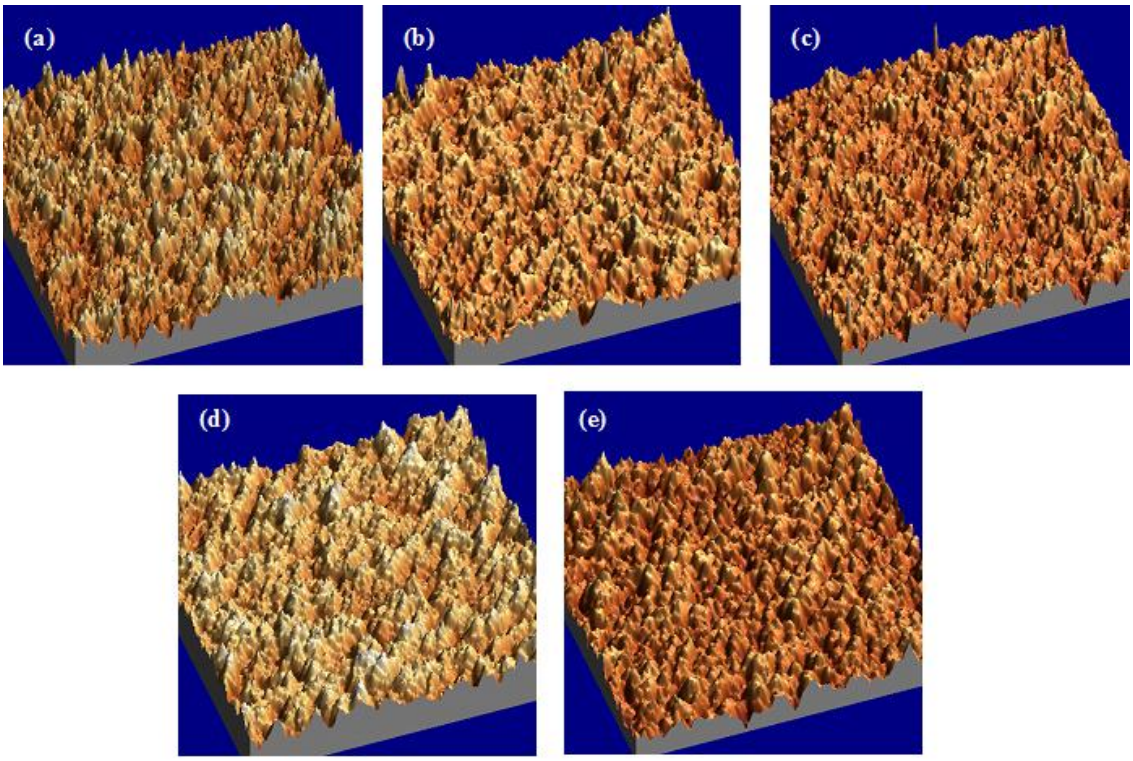

Fig. 4.1. Three-dimensional AFM images (1x1 µm) scan of SiOCH films (a) before and after different plasma treatments, (b) He/O_2, (c) O_2, (d) N_2/H_2 30s, and (e) N_2/H_2 60s.

The He/O_2 and O_2 plasma treated films (Fig. 4.1b and 4.1c) showed a dense arrangement of very fine topographies with R_{rms} of 0.575 and 0.448 nm respectively. When these are compared to the surface morphologies of the samples after N_2/H_2 plasma gas treatments (Fig. 4.1d and 4.1e), it reveals that films subjected to N_2/H_2 for 30s and 60s shows somewhat smoother surfaces with R_{rms} values of 0.421 nm and 0.461 nm respectively.

To quantitatively compare the height dimension for the samples, height histograms (Fig. 4.2) were obtained by graphing number of events (number of feature occurrences) vs. the features height. From the height histograms, all films show a Gaussian height distribution function, a characteristic of regularly rough surface. Compared to the unashed or blanket sample, the curve breadth of the He/O_2 ash sample almost doubles. This can be attributed to the effects caused by the plasma after treatments, the hills begin to connect to each other, via the rough valleys, hence widening up the width/breadth of these peaks. This also causes the development of large asperities; hence the increase in surface roughness of the He/O_2 plasma gas treated film. Moreover, in the case of the O_2 there is a slight increase in the height when compared with the blanket film and a slight increase in the breadth. The corresponding full width half maximum (FWHM) values also show an increase after films were exposed to plasma, showing the unashed film to have a smaller value and the He/O_2 ash film having the highest value.

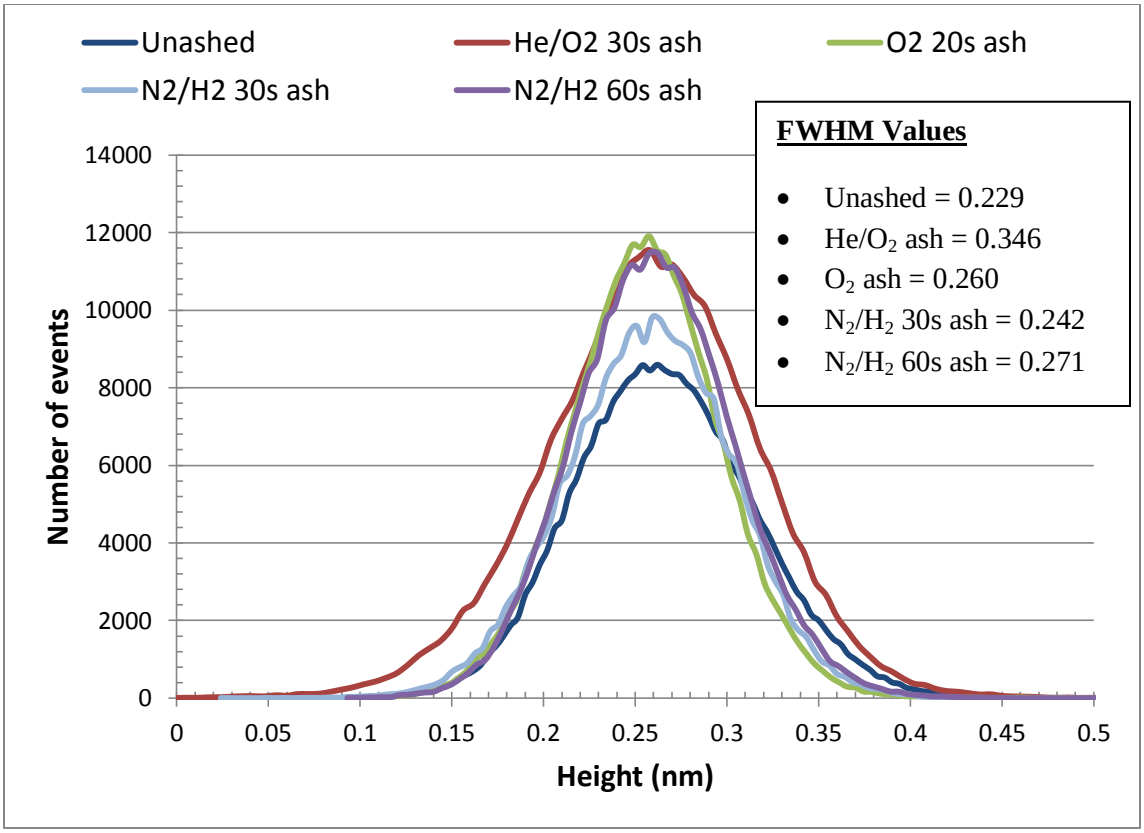

Fig. 4.2. Height histograms of SiOCH surfaces treated with different plasmas.

Even though this has slightly smaller R_{rms} when compared to the He/O_2 treated films, a look at the three dimensional image (Fig. 4.1c) shows similar process of hills beginning to connect with each other. On the other hand, the 30 and 60 s N_2/H_2 treated samples reveals a decrease in the rms roughness. The three dimensional images of these films also exposes the presence of small hills (hillocks) (Fig. 4.1d and 4.1e). This data reveals that when films are exposed to N_2/H_2 gas plasmas, it causes valleys to be developed and causes adjacent peaks to be melded at the same time.

With the O_2 plasma treatments on the film, a number of chemical reactions are possible which causes a change in the film roughness and topography. Oxygen is

generally considered to be the reactive species; therefore it transforms the relatively flat surface into a roughened one, which can cause CO, CO_2 and H_2O to desorb [19]. Adding helium to O_2 is supposed to mitigate this effect, but because of the increase duration of the He/O_2 process (30 s vs. 20 s for the oxygen ash), this process appears to be negated.

Exposure of thin films to plasma has the possibility of causing film shrinkage and film densification. Film densification is prevailing during the initial plasma exposure stage. This can be said to be the reason for the change in roughness observed in the N_2/H_2 plasma ashed films. Thereafter, the plasma bombardment eliminates high secluded peaks, but promotes the amalgamation of the hillocks instead. These effects progresses further as plasma treatment time is increased from 30 to 60 s.

4.3.2 Contact Angle and Surface Free Energy Measurements

Ashed Low-*k* CVD films have been examined to understand the effects of supercritical silylation treatments on the films. Ashing processes can remove the methyl groups which are the hydrophobic carbon species, and significantly lower the contact angle of the films. The average results of five different contact angles and surface free energy readings are shown in Table 1. The surface energy was calculated using the Owens and Wendt method [20,21], utilizing the following equation:

$$\gamma_L(1+\cos\theta) = 2\left[\left(\gamma_S^p\gamma_L^p\right)^{0.5} + \left(\gamma_S^d\gamma_L^d\right)^{0.5}\right] \quad \text{(Eq. 4.1)}$$

where θ is the contact angle, γ_L is the liquid surface tension and γ_S is the solid surface tension, or free energy. The addition of *d* and *p* in the superscripts refer to the dispersive and polar components of each respectively. The dispersive contact angle (Table 1) using diiodomethane (DIM) of the various ashed and unashed samples does not show much

variety, but the polar contact angle measurements using de-ionized (DI) water show the effect of plasma ashing. It can be seen that the unashed film has a contact angle of approximately 92.1˚ (hydrophobic) whiles the ashed samples show much lower contact angles between 43˚-50˚ (hydrophilic). Reducing plasmas such as N_2/H_2 have been found to be capable of removing photoresist efficiently with significantly less damage to siloxane-based low-k films [22]. Film densification and removal was proposed as two mutually limiting processes causing the SiOCH film degradation by N_2/H_2 plasma [23]. Oxygen gas plasma can effectively eliminate methyl groups that are replaced by hydrophilic silanols and bridged oxygens, as shown elsewhere [24,25,26], consequently, low polar contact angle values are observed for He/O_2 and O_2 ashed films.

The decrease in the contact angle for the plasma-ashed low-*k* films (Table 4.1) is as a result of the loss of surface methyl groups, compared to the unashed film that has a very high water contact angle of approximately 92º. The silanol species that remain at the damaged surface due to the plasma ashing process easily absorb water; consequently, the surface contact angle is low suggesting a more hydrophilic surface and higher surface energies. This is evident in the water contact angle values for the 30 sec He/O_2 ashed, 20 sec O_2 ashed, and the 30 and 60 sec N_2/H_2 ashed films.

Table 4.1
The contact angle and surface free energy for water and DIM of As-received samples.

Sample	Contact Angle (^{o})		Surface Free Energy (mN/m)		
	DI H_2O	DIM	γ	γ^d	γ^p
Unashed	92.1 ± 1.2	52.1 ± 1.1	34.4 ± 0.3	33.1 ± 0.3	1.3 ± 0.1
He/O_2 30s	47.0 ± 2.0	46.8 ± 1.8	57.6 ± 0.6	36.0 ± 0.5	21.6 ± 0.6
O_2 20s	43.1 ± 0.9	43.1 ± 1.2	60.9 ± 0.3	38.0 ± 0.3	22.9 ± 0.3
N_2/H_2 30s	48.0 ± 0.8	46.8 ± 2.8	57.0 ± 0.4	36.1 ± 0.7	21.0 ± 0.4
N_2/H_2 60s	50.0 ± 0.4	48.1 ± 2.4	55.5 ± 0.3	35.4 ± 0.6	20.1 ± 0.3

After SC-CO_2/HMDS treatments, all the films appear to make significant recovery of hydrophobicity which is evident by the water contact angle values (Table 4.2) ranging from 77-87˚. It is believed that during the plasma ash process, methyl groups are replaced with hydroxyls, and these functional groups easily react with the HMDS silylating agent to form hydrophobic trimethylsilyls that increase the contact angle. Comparatively, the repaired samples have a lower surface energy approaching that of the unashed film meaning that there are some stable methyl groups on the film surfaces.

Table 4.2
The contact angle and surface free energy for water and DIM of As-Received samples after SC CO_2/HMDS treatment.

Sample	Contact Angle (^{o})		Surface Free Energy (mN/m)		
	DI H_2O	DIM	Γ	γ^d	γ^p
Unashed	90.2 ± 1.3	54.6 ± 0.9	33.6 ± 0.3	31.7 ± 0.3	2.0 ± 0.2
He/O_2 30s	81.3 ± 1.2	63.5 ± 1.8	32.8 ± 0.4	26.6 ± 0.4	6.3 ± 0.3
O_2 20s	76.9 ± 1.4	63.1 ± 1.5	35.0 ± 0.4	26.8 ± 0.4	8.2 ± 0.3
N_2/H_2 30s	86.6 ± 1.1	65.7 ± 2.2	29.7 ± 0.4	25.3 ± 0.5	4.5 ± 0.2
N_2/H_2 60s	85.0 ± 0.5	65.3 ± 2.0	30.5 ± 0.4	25.5 ± 0.5	5.0 ± 0.2

Using DEDMS as the silylating agent recovered the hydrophobicity of the plasma damaged film to some point, as seen in the contact angle measurements (Table 4.3), but it was not close to a full recovery when compared to using HMDS as the silylating agent. DEDMS when used creates dimethylsilyl which have fewer methyl groups, and concurrently less carbon species present, hence the higher surface free energy value. The OC_2H_5 bonds in DEDMS is a weak bond and hence susceptible to dissociation. But we want the alkoxy group to come off, form an alcohol, and allow the siloxane to form. This can cause a limited amount of carbon species to deposit on the films. The use of dimethylsilyl, which are very important in silicone chemistry, are limited in analytical or synthetic chemistry because of the ease with which the derivatives hydrolyze.

Table 4.3
The contact angle and surface free energy for water and DIM of As-Received samples after SC CO_2/DEDMS treatment.

Sample	Contact Angle (^{o})		Surface Free Energy (mN/m)		
	DI H_2O	DIM	Γ	γ^d	γ^p
Unashed	87.5 ± 3.0	52.1 ± 1.1	36.5 ± 0.6	34.3 ± 0.6	2.2 ± 0.4
He/O_2 30s	60.9 ± 4.3	46.8 ± 1.8	49.7 ± 1.1	36.6 ± 0.6	13.1 ± 1.1
O_2 20s	58.2 ± 1.5	43.1 ± 1.1	51.4 ±0.4	36.8 ± 0.4	14.6 ± 0.4
N_2/H_2 30s	63.4 ± 0.7	46.8 ± 2.8	45.9 ± 0.9	32.7 ± 1.6	13.2 ± 0.7
N_2/H_2 60s	61.2 ± 2.1	48.1 ± 2.4	49.1 ± 1.0	35.8 ± 1.4	13.3 ± 0.7

4.3.3 XPS Measurements

XPS experiments conducted confirm that trimethylsilyl groups form on the film surfaces after SC-CO_2 HMDS treatment. From the XPS data (Fig. 4.3) for the as-received samples, the unashed sample showed 28 atomic percent carbon while the N_2/H_2 ashed had about 6%, He/O_2 and O_2 ashed had 7 and 3%, respectively. The 20 sec O_2 ashed sample's carbon atomic percentage of 3% indicates that almost all of the hydrophobic methyls were removed by the plasma ash process. These results agree with the contact angle measurements after the ashing process that shows O_2 ashed samples are the most hydrophilic having the lowest angle (~43º). There is some more residual nitrogen in the N_2/H_2 ashed samples which possibly emanates from the type of plasma used, but the silicon and oxygen concentrations are roughly consistent.

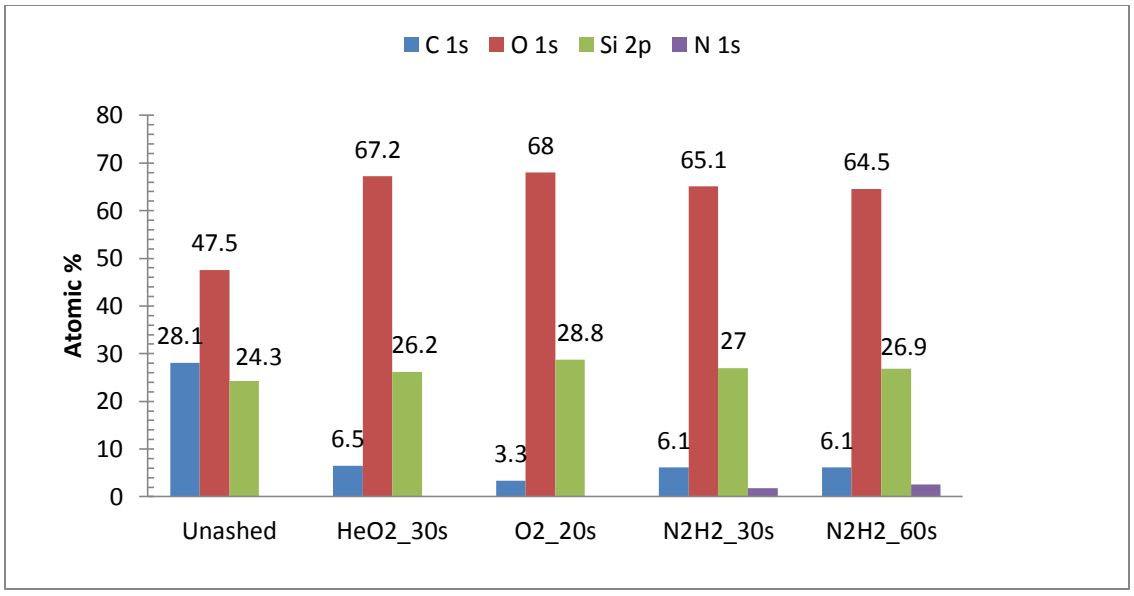

Fig. 4.3. XPS results for as-received unashed and ashed films.

After SC-CO_2/HMDS treatment, there was no effect on the unashed film, which had carbon content of 28% (Fig. 4.4). This is understandable because the unashed film does not have many sites available for silylation and also it has a low surface energy. The He/O_2, O_2, N_2/H_2 30sec and N_2/H_2 60sec ashed samples had approximately the same carbon content of about 12 atomic percent.

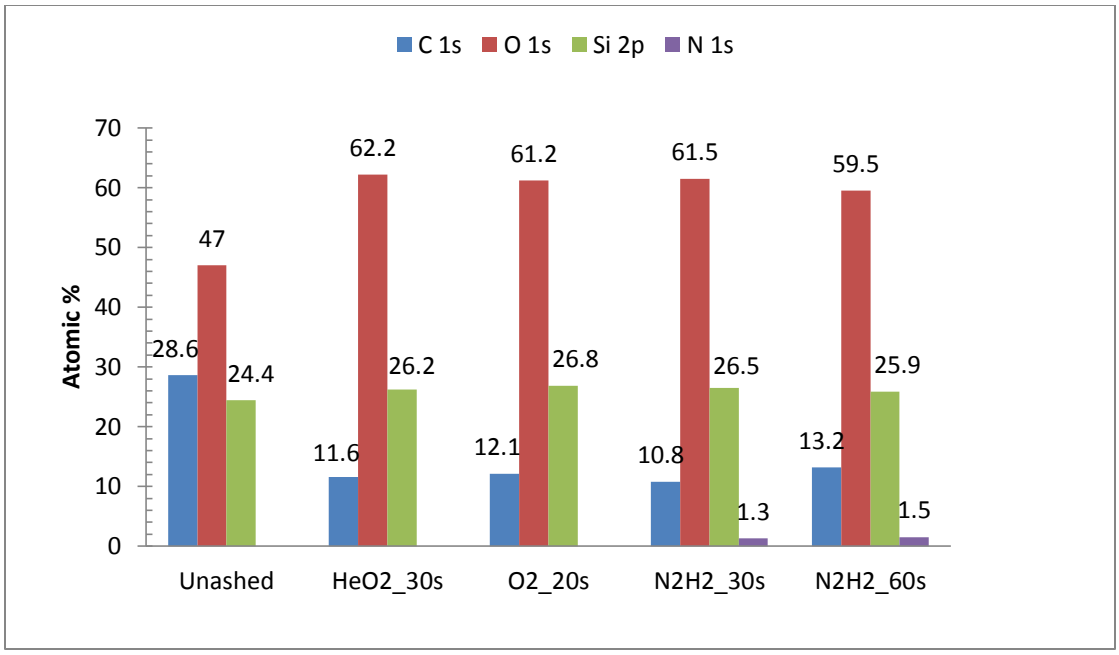

Fig. 4.4. XPS results for unashed and ashed films after SC CO_2/HMDS treatment.

The carbon content after the SC-CO_2/DEDMS treatment as observed from the XPS data (Fig. 4.5) is lower than that obtained after using HMDS as the silylation agent. This buttresses the earlier point made that the creation of dimethylsilyl from DEDMS deposit a lesser amount of carbon on the samples than using HMDS. This is because there are only 2 methyls in DEDMS and they will bond with two silanols while there are 3 methyls in HMDS for every 1 silanol reacted.The number of methyls for HMDS is three times the number for DEDMS per silanol reacted, consequently, HMDS having more carbon content.

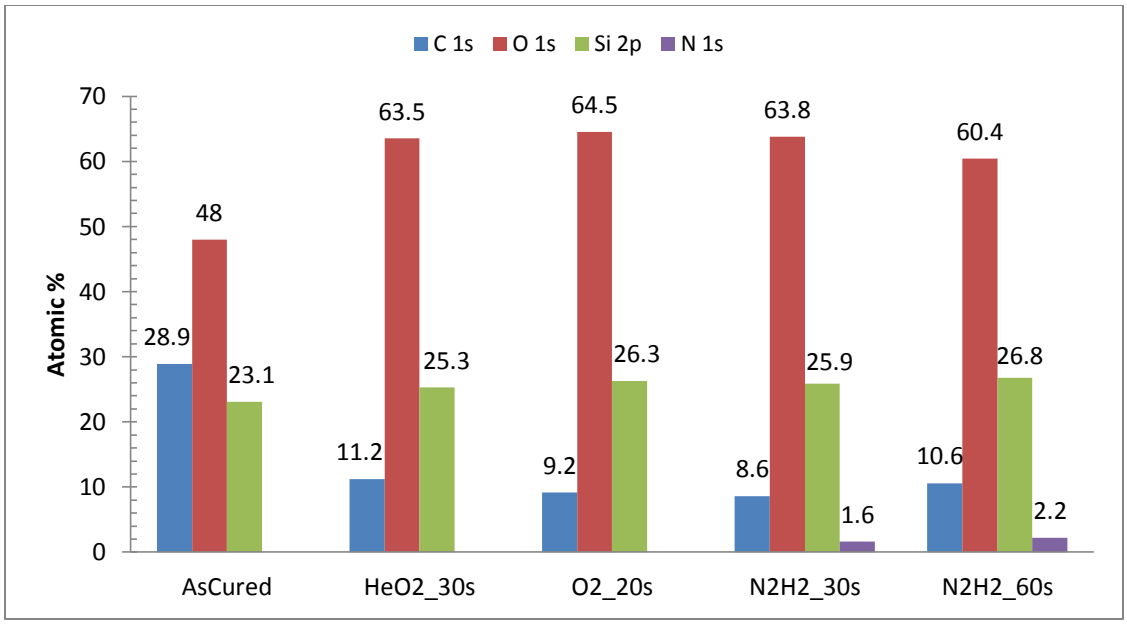

Fig. 4.5. XPS results for unashed and ashed films after SC CO_2/DEDMS treatment.

After SC-CO_2/DEDMS treatment, the carbon concentration of the repaired ashed damaged films (He/O_2 30s, O_2 20s, N_2/H_2 30s and N_2/H_2 60s) ranged from 8-10 atomic percent. Fig. 4.6 shows the sputter depth profile (sputter rate of ~3 nm/min) for carbon before and after exposure of the low-*k* SiOCH thin film to different plasmas. From the depth profile it was found that damage to the films occur on the upper portion of the films approximately to a depth of about 24 nm, where the change in the carbon content of the films are observed. However, after about 3-60 seconds of sputter time, the carbon content increases with depth as the damage lessens showing the inherent carbon content of the bulk film. Hence the loss of carbon moieties occurs mainly at the surface of the low-*k* thin films.The amount of carbon at the beginning of sputter is the same as the carbon concentration during the high resolution scans, but carbon is a lighter element so there is

the tendency of preferential sputtering of the carbon when performing depth profile analysis using an Ar gun.

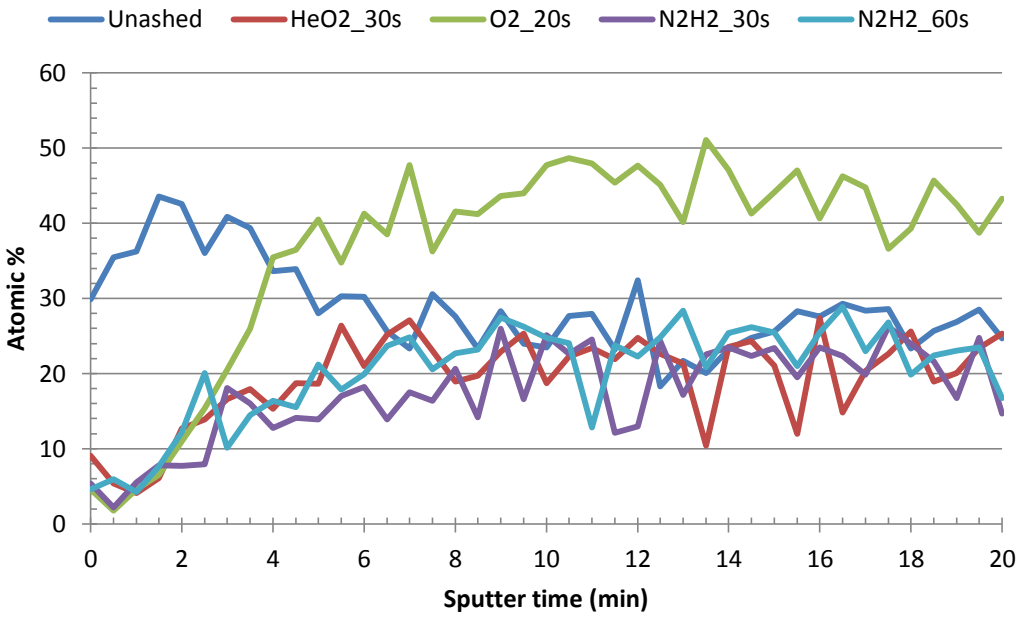

Fig. 4.6. XPS carbon depth profile for unashed and ashed low-*k* CVD films.

From these results, the O_2 20sec ash causes more damage to the film showing the lowest carbon content. He/O_2 30sec and N_2/H_2 60sec ash processes shows higher carbon concentration compared to the N_2/H_2 30sec and O_2 20sec ash. This might be due to the possibility of the He/O_2 30sec and N_2/H_2 60sec ashes causing the film to densify. After SC-CO_2/HMDS treatments, even though the XPS composition data shows an increase in carbon content indicating the presence of trimethylsilyls, the XPS depth profile (Fig. 4.7) does not differ significantly from the ashed samples. This result confirms previously proposed conclusions that the recovery process takes place at the surface of the films and does not occur beyond the depth of 2 nm. The trimethylsilyl groups from the HMDS that are initially deposited seal most of the pores, thereby not allowing for deeper penetration

of the silylating agents. This may be one reason why the ashed damaged film does not seem to be fully repaired after SC-CO_2 HMDS treatment.

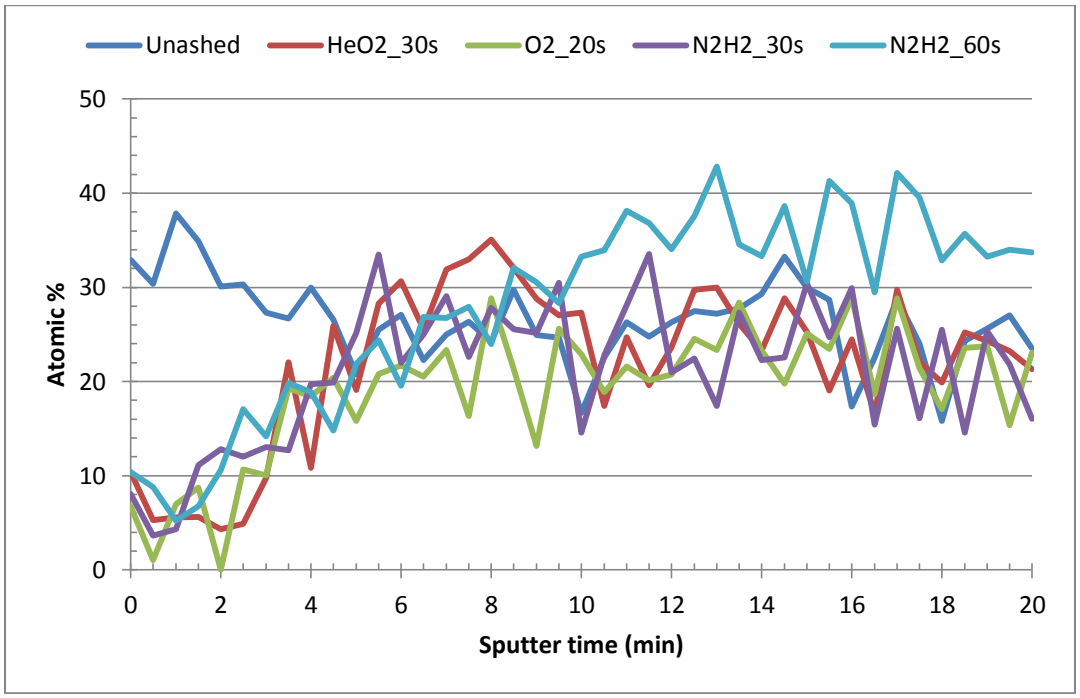

Fig. 4.7. XPS carbon depth profile for unashed and ashed low-k CVD films after SC-CO_2/HMDS treatment.

4.3.4 FTIR Analysis

Fig. 4.8 shows the variation of the FTIR-GATR (grazing angle attenuated total reflectance) absorption spectra over the range of 4000 - 800 cm^{-1} of the SiOCH films for the unashed and plasma ashed films which also shows relevant absorption band assignments. The peaks at around 1248 - 960 cm^{-1} describe the Si-O-Si stretching vibration modes. Those adsorption peaks at approximately 1275 cm^{-1} are from the Si-CH_3 bending mode and those at 3020 – 2815 cm^{-1} are from the C-H_x (x = 2, 3) bending vibrations, which signifies the presence of methyl groups in the film. The reduction of the

C-H_x, and Si-CH_3 peaks illustrates the removal of methyl groups caused by interaction with the plasma species. There is also an increase in the Si-OH adsorptions observed at around 3100-3600 cm^{-1} that suggests the replacement of methyl groups with silanols. This abundance of silanols makes the films susceptible to moisture absorption. The silanols can be located at approximately 3300 cm^{-1}, which is seen as a hump in Fig. 4.8. The absorption band at about 1620 cm^{-1} has been assigned to the deformation mode of the H-OH bond, and is probably due to H_2O trapped inside the pores of the film.

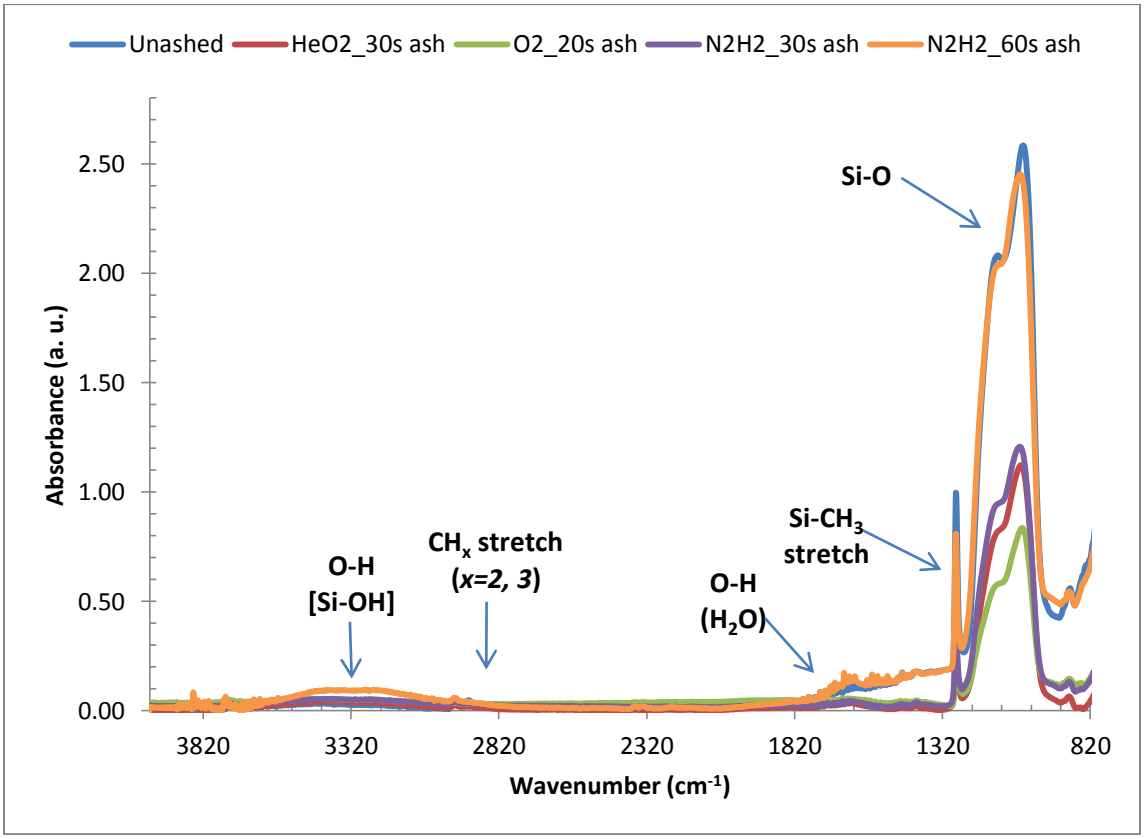

Fig. 4.8. FTIR spectra of unashed and plasma ashed SiOCH films.

Fig. 4.9 shows the transmission FTIR variation from 4000 – 900 cm^{-1} for the repaired plasma ashed SiOCH films using SC-CO_2/HMDS treatment. After the treatment, the

plasma damaged films show significant increase in both the Si-CH_3 and C-H_x (x = 2, 3) peak intensities. The Si-OH peak observed after the plasma damage was not observed after the SC-CO_2/HMDS treatment. This result is likely because most of the hydrophilic silanol (Si-OH) groups have been replaced by the hydrophobic trimethylsilyl (Si-$(CH_3)_3$) groups.

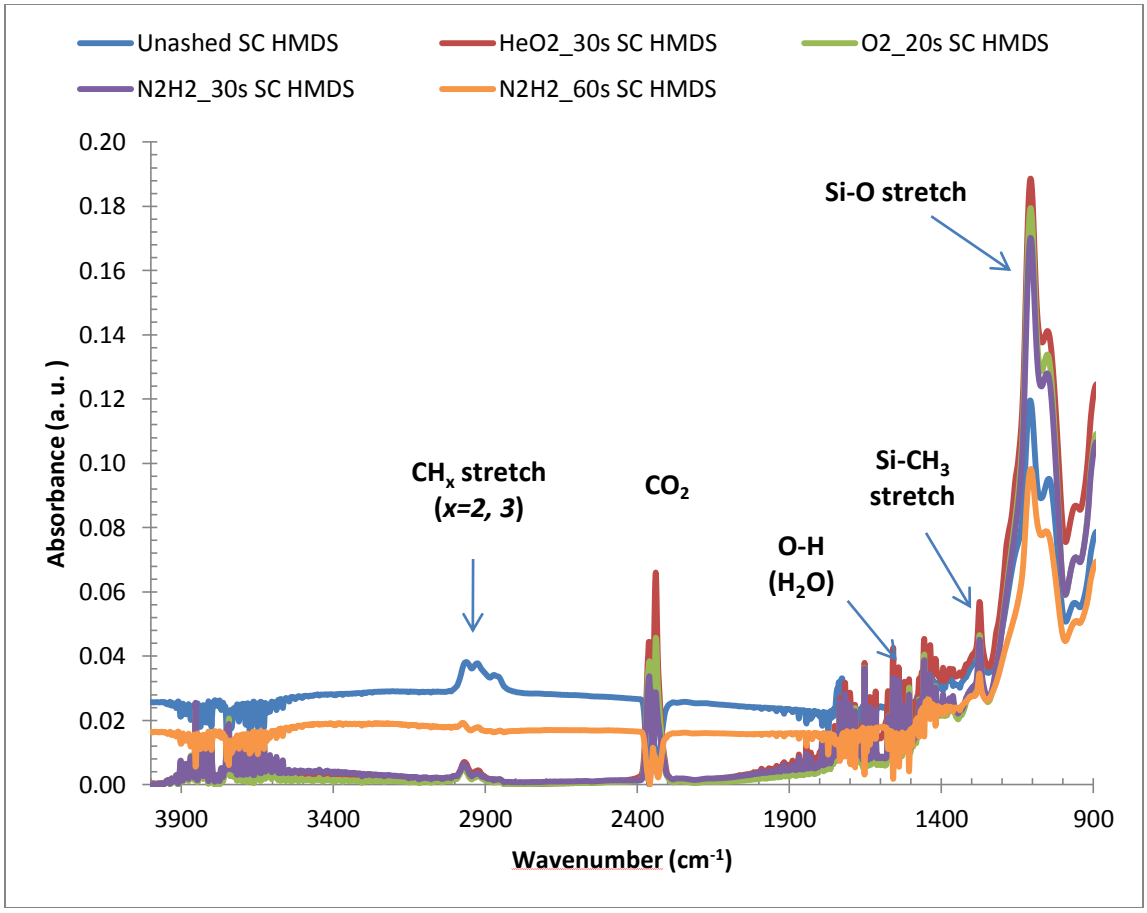

Fig. 4.9 FTIR spectra of repaired ashed low-*k* SiOCH films using SC-CO_2/HMDS.

Table 4.4
Infrared wavenumber and band assignment for low-k thin films.

Wavenumber (cm^{-1})	Band Assignment
3750	Si-OH stretching vibration (isolated) [27]
2960	C-H asymmetric stretching, CH_3 [28,29]
2930	C-H asymmetric stretching, CH_2 [30]
2878	C-H symmetric stretching, CH_3 [31]
2854	C-H symmetric stretching, CH_2 [29]
1275	Si-CH_3 symmetric deformation [32]
1100	Si-O-Si symmetric stretch vibration [33]
1170	Si-O-C asymmetric stretching [31]
970	Si-OH stretching vibration [25]

The use of DEDMS as silylation agent in SC-CO_2 showed the recovery of the films to some extent by the depositing dimethylsilyl, this is observed in the FTIR transmission data (Fig. 4.10) below. This is confirmed by the presence of absorption band of CH_x ($x=2, 3$) at approximately 3000 – 2840 cm^{-1}. This silylation minimizes the availability of sites that can cause additional condensation reactions and also for hydrogen bonding which can induce collapse of the skeletal network during drying. The presence of a sharp and intense band at approximately 1275 cm^{-1} corresponding to the symmetric deformation vibration of the C-H bonds, represents methyl groups attached to silicon [29]. By comparing the as-received samples and the SC-CO_2 DEDMS and HMDS treated film, the introduction of methyl groups on the films surfaces decreases the presence of

silanols. This is verified by the disappearance of the silanol (Si-OH) stretch is located at approximately 3900 cm^{-1} in Fig. 4.8.

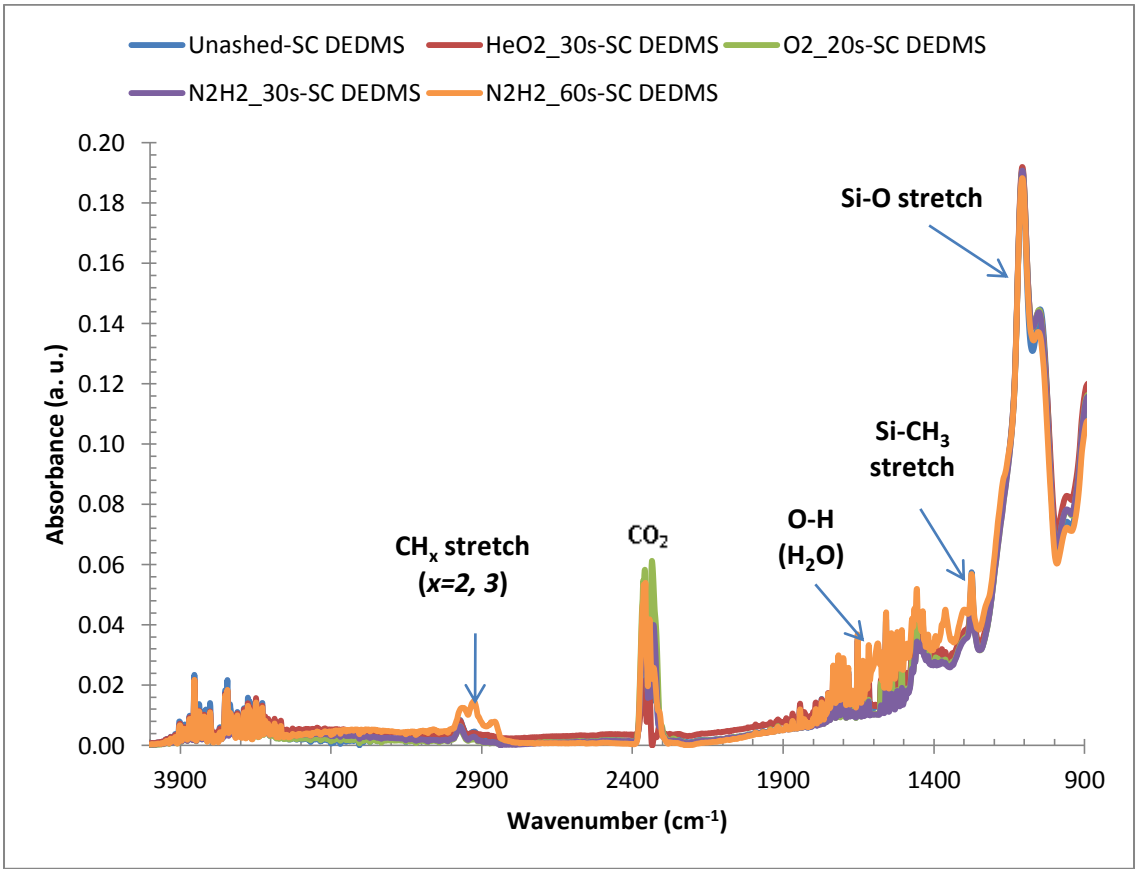

Fig. 4.10. FTIR spectra of repaired ashed low-k SiOCH films using SC-CO_2/DEDMS.

4.3.5 Ellipsometry Measurements

Spectroscopic ellipsometry depth profiles of these films have been studied and the results published elsewhere [34]. From the results, as one would expect, the 60sec N_2/H_2 ashed densifies the film more than its 30sec counterpart. From Fig. 4.11, N_2/H_2 60sec ash suffered some film loss (5 nm). The oxidizing ashes suffered more film loss (18–28 nm)

while the 30sec N_2/H_2 ashed film showed an increase in thickness compared to the unashed film. It is believed that this apparent increase in thickness is due to variations in original CVD low-*k* film deposition on individual wafers prior to ashing.

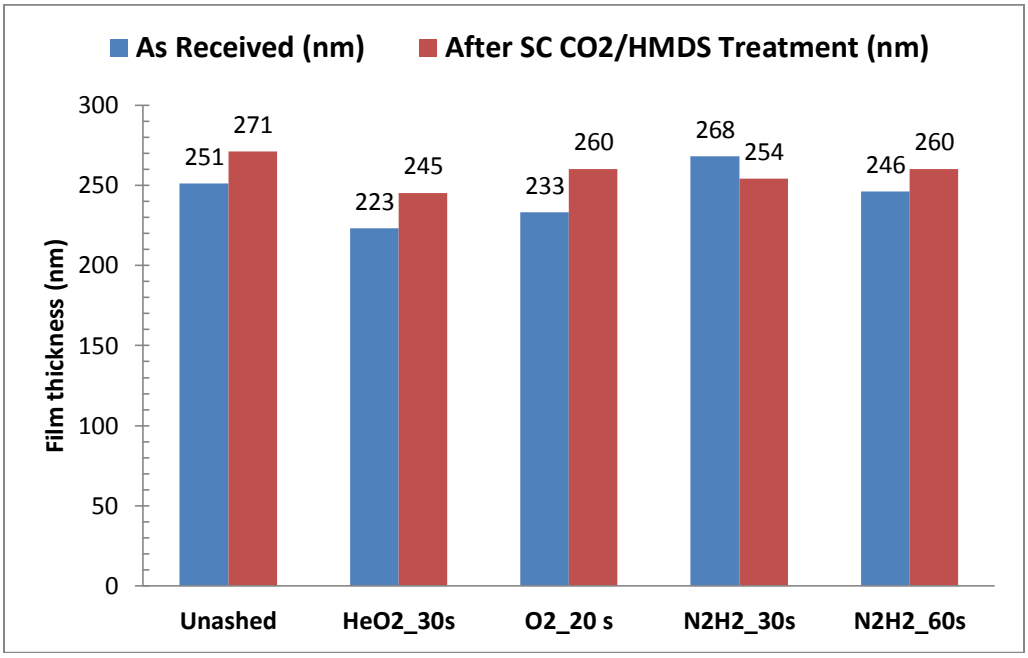

Fig. 4.11. Film thicknesses of unashed and ashed low-k films before and after SC CO_2/HMDS Treatment.

The refractive indices from Fig. 4.12 show that there is a slight difference in the refractive index of the topmost layer of the films after the ashing process. The N_2/H_2 30sec and 60sec and the He/O_2 30sec ashes impart lower refractive index compared to the O_2 20sec ash. The depth profile from Fig. 4.12 also shows the topmost layer of the ashed films to be densified. The He/O_2 30sec ash imparts more densification than the O_2 20sec ash. This is surprising because we did not expect this. As expected the longer duration of the N_2/H_2 60sec ash makes it more compared to the 30sec ash. These films were measured using the Woollam variable angle spectroscopic ellipsometer (WVASE), and

modeled a number of times to optimize the reproducibility of the result, specifically to address the layer thickness and the nature of the density grading.The Cauchy Model was employed in finding the refractive index and the thickness differences. In Cauchy Model, the index of refraction, *n* and extinction coefficient, k are represented by slowly varying them as a function of wavelength, λ, and an exponential absorption tail, respectively [35]:

$$n(\lambda) = A + \frac{B}{\lambda^2} + \frac{C}{\lambda^4} \quad \text{(Eq. 4.2)}$$

$$k(\lambda) = \alpha e^{\beta(12900\left(\frac{1}{\lambda}\times\frac{1}{\gamma}\right))} \quad \text{(Eq. 4.3)}$$

where *A*, *B*, and *C* are known as the Cauchy coefficients. *A* is the dominates *n(λ)* for long wavelengths, *B* controls the curvature of *n(λ)* in middle of the visible spectrum and *C* influences *n(λ)* to a greater extent in shorter wavelengths. The lowest refractive index should be the same for all the samples, but the models performed did not agree with fitting the data that way.

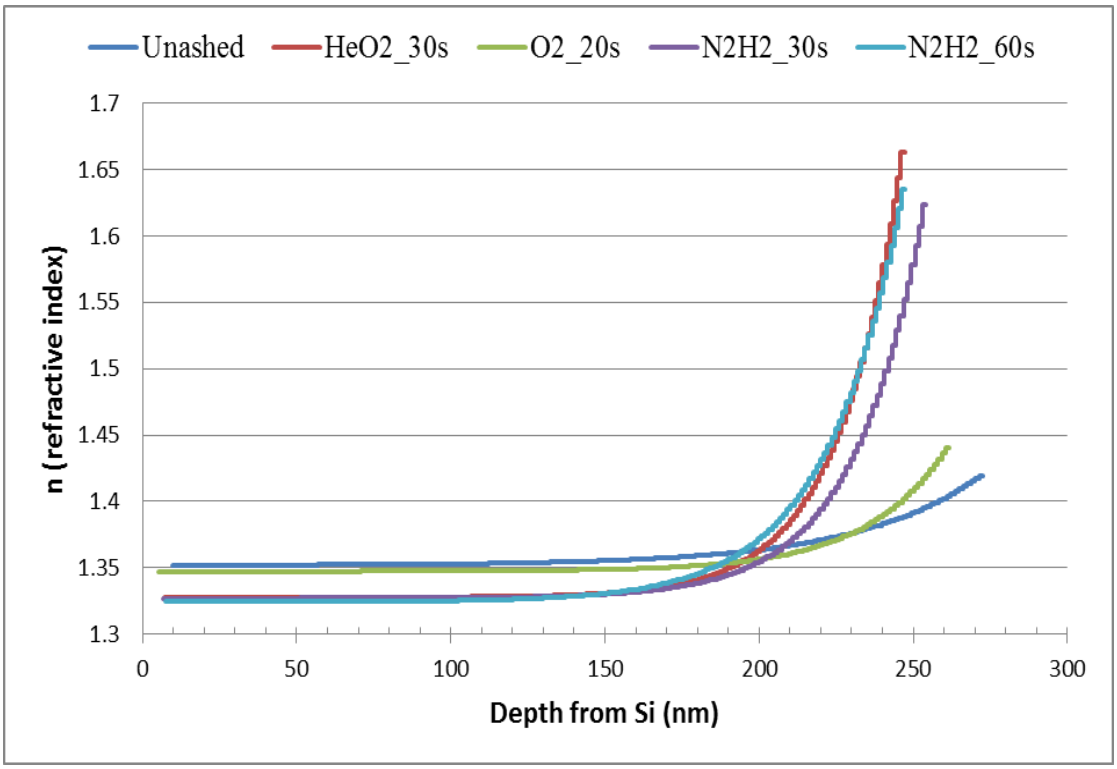

Fig. 4.12. Spectroscopic ellipsometry derived refractive indices and depth profiles of unashed and ashed low-k films.

As seen in Fig. 4.13, there is again an increase in the film thicknesses after SC-CO_2/DEDMS treatment. Even though, the unashed film showed a slight increase in thickness, this is thought of to be possibly due to the unreacted DEDMS on the surface of the films, as the unashed films has lesser or no amount of silanol to aid in the creation of dimethylsilyl. Comparing the HMDS and the DEDMS repaired shows the DEDMS repaired to have slightly higher thickness values than the HMDS value. This was not expected though, HMDS silylates to create trimethylsilyls whiles DEDMS forms dimethylsilyls, which has fewer methyl groups than the former. But this can also be due to the fact that figuratively, trimethylsilyls are bushy than dimethylsilyl, hence the later might be able to penetrate into the available voids, and also form thicker layers.

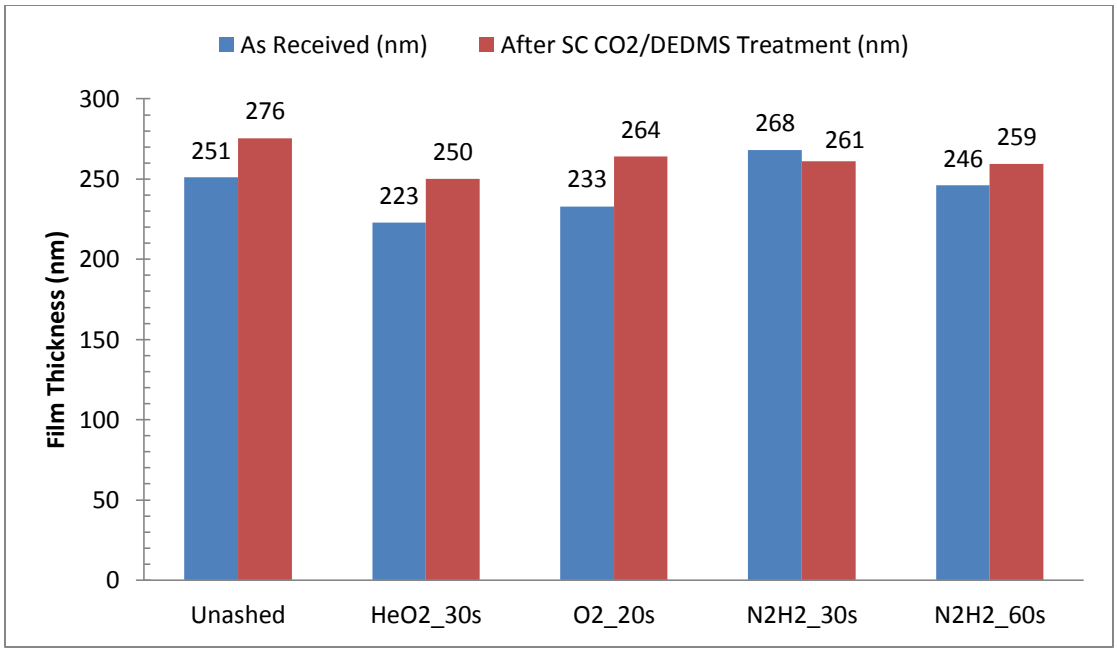

Fig. 4.13. Film thicknesses of unashed and ashed low-k films before and after SC CO_2/DEDMS Treatment.

4.4 Conclusions

The effects of different plasmas on porous low-*k* CVD SiOCH thin films and the use of SC-CO_2/HMDS and SC-CO_2/DEDMS treatment to repair these ashed films were investigated. After different plasma exposures, the topography of these films differed among the different plasma treated films. All ashed films showed similar water contact angles which was attributed to the near similar surface carbon concentration observed using the XPS. The water contact angles increased after modifying the surfaces of the films in SC-CO_2/HMDS and DEDMS. Using HMDS showed a higher recovery effect on the films because of the presence on trimethylsilyls as compared to dimethylsilyl for the DEDMS. The presence of these hydrophobic methyls caused the surface energies to also decrease, hence reducing the amount of moisture and other deleterious chemicals that can

be adsorbed into the films. These carbon deposited on the films through surface modification is assumed to occur up to about 2 nm, as the first few deposited methyl seal the pores thereby preventing others to go though. From the IR studies, it is evident that the Si-OH and the H-O-H groups are removed during silylation and replaced by methyl groups. This is also evident by the increase in the intensity of the CH_x (x=2, 3) and the $Si\text{-}CH_3$ stretches. Ellipsometric measurements also reveal a slight increase in the thicknesses of the films after modifying the surfaces of the films. Ellipsometric depth profile of the films also showed the topmost layer of the ashed films to be densified where the He/O_2 plasma imparted more densification than the O_2 and the other plasmas.

4.5 References

[1] International Technology Roadmap for Semiconductors, 2008 Update.

[2] A. Grill, V. Patel, J. Appl. Phys. 85 (1999) 3314.

[3] L. Hrubesh, S. R. Buckley, Mater. Res. Soc. Symp. Proc. 476 (1997) 99.

[4] B. Xie, A. J. Muscat, Microelectronic Engineering 76 (2004) 52-59.

[5] E. Taglauer, Appl. Phys. A 51 (1990) 238.

[6] E. Kandoh, M. R. Baklanov, H. Bender, K. Max, Electro-Chem. Solid State Lett. 1 (1998) 224.

[7] S. Rogojevic, A. Jain, W. N. Gill, J. Plawsky, Electro-Chem. Solid State Lett. 5, F22 (2002).

[8] J. J. Kim, S. B. Jung, H. H. Park, S. H. Hyun, Thin Solid Films 467 (2000) 377-378.

[9] S. S. Prakash, C. J. Brinker, A. J. Hurd, J. Non-Cryst. Solids 190 (1995) 264.

[10] Y. S. Mor, T. C. Chang, P. T. Tsai, C. W. Chen, S. T. Yan, C. J. Chu, W. F. Wu, F. M. Pan, W. Lur, S. M. Sze, J. Vac. Sci. Technol. B20 (2002) 1334.

[11] B. Xie, A. J. Muscat, Microelectronic Engineering 76 (2004) 52-59.

[12] R. F. Reidy, Z. Zhang, R. A. Orozco-Teran, B. P. Gorman, D. W. Mueller, MRS Proceedings, Materials, Technology, and Reliability for Advanced Interconnects and Low-k Dielectrics, Vol. 766 (2003) 303-308.

[13] K. L. Chavez, G. L. Bakker, D. W. Hess, J. Vac. Sci. Technol. B19 (2001) 2144-2148.

[14] D. L. Goldfarb, J. J. de Pablo, P. F. Nealey, J. P. Simons, W. M. Moreau, M. Angelopoules, J. Vac. Sci. Technol. B18 (2000) 3313-3317.

[15] R. A. Orozco-Teran, B. P. Gorman, Z. Zhang, D. W. Mueller, and R. F. Reidy, MRS Proceedings Vol 766, Materials, Technology, and Reliability for Advanced Interconnects and Low-k Dielectrics, Editors: A. McKerrow, J. Leu, O. Kraft, T. Kikkawa, 2003, E8.20.

[16] B. P. Gorman, R. A. Orozco-Teran, Z. Zhang, P. D. Matz, D. W. Mueller, R. F. Reidy, Journal of Vacuum Science and Technology B: Microelectronics and Nanometer Structures, v 22, n 3, p 1210-1212 (May/June 2004).

[17] B. Lahlouh, J. A. Lubguban, G. Sivaraman, R. Gale, S. Gangopadhyay, Electrochemical and Solid-State Letters, v 7, n 12, p G338-41, Dec. 2004.

[18] I. Horcas, R. Fernandez, J. M. Gomez-Rodriguez, J. Colchero, J. Gomez-Herrero, and A. M. Baro, Rev. Sci. Instrum. 78, 013705 (2007).

[19] M. Nakahara, Y. Sanada, J. Mater. Sci. 29 (1994) 3193.

[20] D. K. Owens, R. C. Wendt, J. Appl. Poly. Sci. 13 (1969) 1171.

[21] S. Wu, Polymer Interfaces and Adhesion, Marcel Dekker, New York, 1982.

[22] E. Vinogradova, E. Osei-Yiadom, C. E. Smith, D. W. Mueller, R. F. Reidy, Microelectronic Engineering 86 (2009) 176-180.

[23] H. Cui, R. J. Carter, D. L. Moore, J. Appl. Phys. 97 (2005) 113302.

[24] J. J. Kim, S. B. Jung, H. H. Park, and S. H. Hyun, Thin Solid Films 467 (2000) 377-378.

[25] P. D. Matz, R. F. Reidy, Solid State Phen. 315 (2005) 103-104.

[26] C. E. Smith, D. W. Mueller, P. Matz, R. F. Reidy, Mater. Res. Soc. Symp. Proc. 914 (2006).

[27] C. J. Brinker, G. W. Scherer, Sol-Gel Science, The Physics and Chemistry of Sol-Gel Processing, Academic Press, San Diego, 1990.

[28] A. V. Rao, E. Nilsen, M. A. Einarsrud, J. Non-Cryst. Solids 296 (2001) 165.

[29] N. Yamada, T. Takahashi, J. Electrochem. Soc. 147 (2000) 1477.

[30] A. L. Smith, Spectrochem. Acta 16 (1960) 87.

[31] J. Workman, Handbook of Organic Compounds: NIR, IR, Raman, and UV-Vis Spectra Featuring Polymers and Surfactants, Methods and Interpretations, vol. 1, Academic Press, San Diego, 2001.

[32] S. V. Nitta, V. Pisupatti, A. Jain, P. C. Wayner Jr., W. N. Gill, J. L. Plawsky, J. Vac.Sci. Technol. B 17 (1999) 205.

[33] G. Socrates, Infrared Characteristics Group Frequencies, John Wiley, New-York, NY, 1980.

[34] E. Vinogradova, E. Osei-Yiadom, C. E. Smith, D. W. Mueller, R. F. Reidy, Microelectronic Engineering 86 (2009) 176-180.

[35] J. A. Woollam, Co., Inc., Guide to Using WVASE 32 Spectroscopic Ellipsometry Data Acquisition and Analysis Software (2008) 190.

CHAPTER 5

TEMPERATURE EFFECTS ON REPAIRED PLASMA DAMAGED LOW-*K* SIOCH FILMS

5.1 Introduction

Silicon dioxide (SiO_2) had been the principal insulator in semiconductor devices for many years. As the device features of integrated circuits (ICs) continues to shrink, the resistance × capacitance (RC) delay greatly limits their performance and reliability due to the increased power dissipation and metal line cross-talk which arise in multilevel interconnects, in the copper damascene process [1]. The improvement in device performances in terms of speed and power consumption required new materials in order to decrease metal line resistances and reduce parasitic capacitances between metal lines [2]. In other to reduce these parasitic capacitances, materials having low-dielectric (low-*k*) constant is been studied for use as interlayer dielectrics. The *k* values of these dielectric materials were initially lowered by adding fluorine to silica films. Later low-*k* replacements included hydrocarbon films, oxide films with organic functional groups (organosilicate glasses or SiOCH films) [3], and these SiOCH films that included porogens during processing to create porosity. Several thin films synthesized by various chemical vapor deposition (CVD) methods have been studied to replace SiO_2. Porous carbon

doped oxide dielectrics (SiOCH) have been widely studied as promising candidates for interlayer dielectric applications in multilevel interconnect architectures [4]. SiOCH structure is composed of Si-O backbone with methyl (CH_3) incorporation. Methyl groups have lower polarizations and can reduce the film's density, thus decreasing the dielectric constant while, on the other hand, the main Si-O component in the film provides other good properties similar to silicon dioxide (SiO_2) [5].

With the aim of lowering the dielectric constant and having a good thermal stability, several groups have deposited low-*k* films using a mixture of hydrocarbon and precursors containing Si-O. Grill et al. reported the plasma enhanced chemical vapor deposition (PECVD) deposition of SiCOH-CH films with a mixture of SiCOH and hydrocarbon precursors [6,7]. Lubguaban and Rajagopalan reported the PECVD deposition of organosilicate glass (OSG) films with tetravinyl-tetramethylcyclotetrasiloxane (TVTMCTS) precursors using lower pressure and power [8]. They reported the films to be having *k* values of 2.05 and 2.65 with good thermal stability after annealing at 400 °C.

In this work, I report the effect of temperature on a SiOCH low-*k* CVD thin film. The film was also damaged using He/O_2, O_2 and N_2/H_2 plasma sources at different durations, so we also report the effects of temperature on these films after they have been repaired using hexamethyldisilazane (HMDS, as will be referred in this work; $(CH_3)_3Si\text{-}NH\text{-}Si(CH_3)_3$) and diethoxydimethylsilane (DEDMS, as will be referred to in this work; $(CH_3)_2Si(OC_2H_5)_2$) as silylation agents in supercritical carbon dioxide.

5.2 Experimental

The CVD SiOCH low-*k* films used in this work were synthesized from ringed siloxane compounds and molecular templates. The films had a nominal thickness of 250 nm, a porosity of ~28%, and a dielectric constant of approximately 2.35. The films were exposed to 30 sec He/O_2, 20 sec O_2, and 30 and 60 sec N_2/H_2 plasma ash treatments respectively. Prior to characterization measurements, the wafers were cleaved into multiple pieces. Samples from each of the plasma conditions were subsequently treated with supercritical CO_2 containing HMDS as the silylating agent for approximately 5 minutes. Other samples were also treated with SC-CO_2 DEDMS for approximately the same duration. The super-critical reactor is a cylindrical design with a 2.5 inch inner diameter and a length of about 6.5 inches. Supercritical (SC) experiments in this study were conducted at 1900 psi (9.6 MPa) and 40 ^{o}C.

Following exposure to the supercritical fluids, the films were heat treated using an in-situ FTIR heating stage, varying temperatures from room temperature (25°C) to 400 °C at 100 °C increments. At each increase in temperature, Fourier transform infrared spectroscopy (FTIR) transmission spectra were obtained using a Nexus 470-FTIR to study the films surface chemistry and the effect the heat treatment has on the hydrophobic methyl groups and the backbone Si-O bonds of the film. This was repeated for the as-received unashed film. An X-ray photoelectron spectrometer (XPS) PHI 5000 Versa probe was used to study the films surface composition before and after each process. Changes in thicknesses and refractive indices, (at 632.8 nm wavelength) were measured using a JA Woollam variable angle spectroscopic ellipsometer (VASE).

5.3 Results and Discussions

5.3.1 FTIR Analysis

Fig. 5.1 shows the variation of the FTIR transmission absorption spectra over the range of 4000–900 cm^{-1} of the SiOCH film for the in-situ FTIR temperature variation process. The peaks at around 1250 – 980 cm^{-1} are from the Si-O related stretching vibration modes, those at around 1300 – 1240 cm^{-1} are from the $Si-CH_3$ bending mode [9,10], those at around 1500 – 1350 cm^{-1} are from CH_2+CH_3 bending vibrations [11], and those at around 3100 – 2800 cm^{-1} are due to the CH_x (x=2, 3) stretching vibrations. Relevant absorption band assignments are shown in Table 5.1.

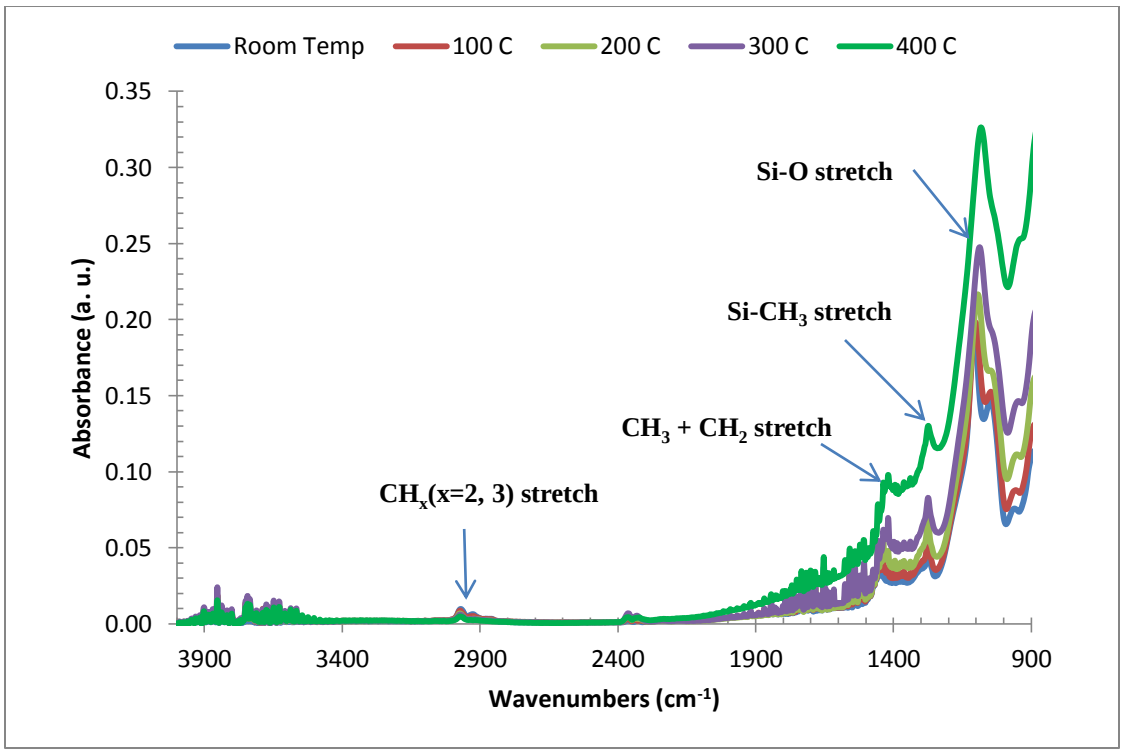

Fig. 5.1. Change of the FTIR transmission absorption spectra of the as-deposited SiOCH film as a function of temperature.

The data above shows a correlation between the Si-CH_3 peaks intensity and the temperature treatments. As the temperature increases, the intensity of the peaks decreases and also increases in their FWHM indicating stretching of the bonds. This is in agreement with the results of other researchers. Lin et al. reported that for the methyl groups we can expect mechanical properties such as the stiffness, hardness and/or fracture toughness of the OSG coating to depend strongly on each other [12]. Nakano et al. reported that the film properties of a spin-on-glass (SOG) film formed from synthesized coating solutions were evaluated as a function of Si-CH_3 concentration [13]. As temperature increases, there is also the possibility of an increase in open void appearances in the oxide, which will alter the mechanical properties of the film and might also cause for a decrease in the dielectric constant, *k* which was observed by W. C. Ee et al [14].

Table 5.1
Infrared wavenumber and band assignment for low-k thin films.

Wavenumber (cm^{-1})	Band Assignment
3750	Si-OH stretching vibration (isolated) [15]
2960	C-H asymmetric stretching, CH_3 [16,17]
2930	C-H asymmetric stretching, CH_2 [18]
2878	C-H symmetric stretching, CH_3 [19]
2854	C-H symmetric stretching, CH_2 [29]
1275	Si-CH_3 symmetric deformation [20]
1100	Si-O-Si symmetric stretch vibration [21]
1170	Si-O-C asymmetric stretching [31]
970	Si-OH stretching vibration [25]

The CH_x peak (Fig. 5.2) of the as-deposited film as a function of increasing temperature using an in-situ FTIR heating stage shows the presence of four hydrocarbon peaks which include the C-H_3 asymmetric (2970 cm^{-1}), C-H_2 asymmetric (2926 cm^{-1}), C-H_3 symmetric (2875 cm^{-1}), and C-H_2 symmetric (2857 cm^{-1}) vibrations respectively. As temperature increases from room temperature (25 ºC) to 400 ºC, the area of all the CH_x peaks decreases. At 400 ºC the areas of all the peaks tend to be approximately zero with exception of the CH_3 asymmetric peak. The C-H_2 (asymmetric and symmetric) peaks provide direct evidence of the presence of ethylene groups in the SiOCH films [22]. It is believed that the disappearance of the other CH_x peaks gives an evidence of the removal of thermally unstable C-H fragments.

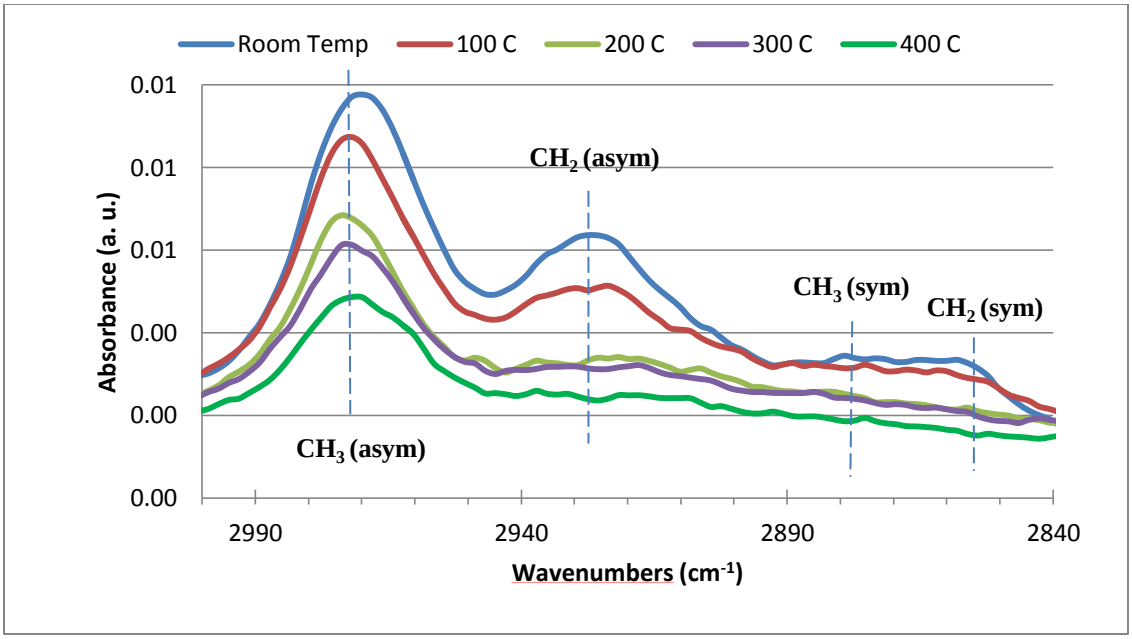

Fig. 5.2. CH_x peak of the as-deposited blanket film as a function of temperature.

The peak at approximately 1275 cm^{-1} is attributed to the Si-CH_3 bending mode. The intensity of the Si-CH_3 peak decreases with increasing temperature indicating the removal of organic fragments. The relation between the intensity of the Si-CH_3 peaks and the temperature is in agreement with other researchers results. S. Lee et al. reported that at temperature of 400 ºC, they saw reduction in their CH_3 peaks [23].

Figs. 5.3(a) – 5.3(d) shows the de-convolution of the Si-O-Si stretching band of the unashed film after subjecting it to different temperature treatments. For the as-received film at room temperature, four bands appeared with peaks at approximately 1047 [7], 1106 [7], 1145 [7], and 1198 [22] cm^{-1} respectively.

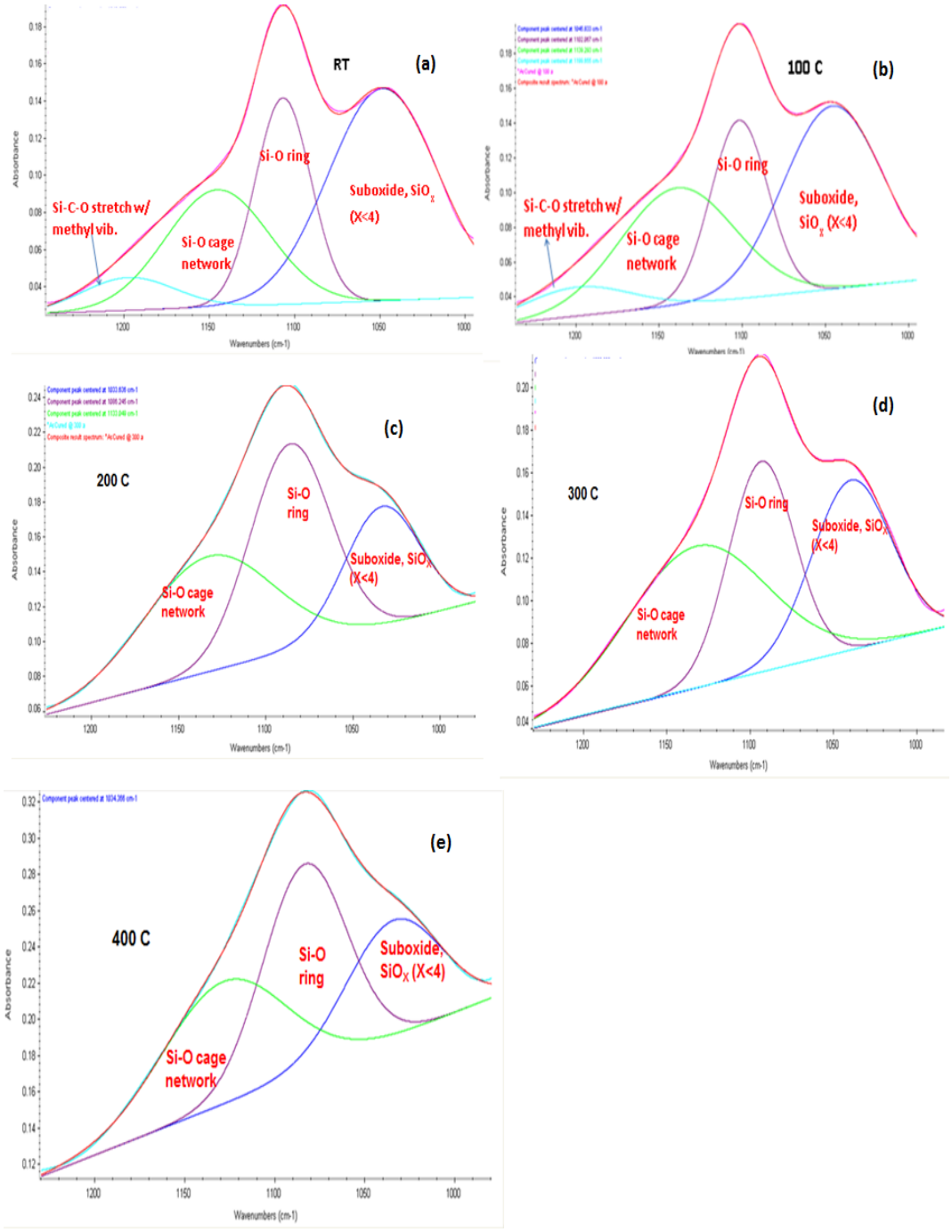

Fig. 5.3. De-convolution of the Si-O stretching band of the unashed film at different heat treatments (a) room temperature (25 °C) (b) 100 °C (c) 200 °C (d) 300 °C (e) 400 °C.

For the film at room temperature, the peaks correspond to various suboxidized states of the siloxane network, SiO_x (x<4) (1047 cm^{-1}), Si-O ring formation (1106 cm^{-1}), Si-O cage network (1145 cm^{-1}) and Si-C-O stretching with methyl/hydroxyl vibration modes (1198 cm^{-1}) [3]. As temperature was increased to 100 °C, the same peaks for the film at room temperature were observed, but there were some shifts in the peak positions to lower values. These shifts can be attributed to changes in Si-O-Si bond angle, which is indirectly related to the stretching frequency [24]. At higher temperatures (200 – 400 °C) the peaks for Si-C-O stretching with methyl/hydroxyl was reduced until it could not be detected. This also causes the remaining peaks of sub-oxide (SiO_x, x<4), Si-O ring formation, and Si-O cage network to have an increased FWHM value. This indicates the stretching of the Si-O-Si bond. Wong et al. reported that the cage structure of Si-O-Si can produce a microporous structure and a lower film density [25].

Supercritical carbon dioxide (SC-CO_2) and HMDS have been used to repair the plasma damaged low-*k* CVD SiOCH films details of which has been presented earlier in Chapter 4. A second silylation agent, DEDMS was also used to repair these damaged films. Temperature treatments were performed on these films. In an earlier chapter, it was discussed that these functionalizing agents are able to recover the plasma damaged films by depositing methyl groups on the films. Fig. 5.4 shows the FTIR-transmission in-situ heat treatment spectrum in the wave range of 4000 –900 cm^{-1} for the repaired He/O_2 30 sec ash damaged film.

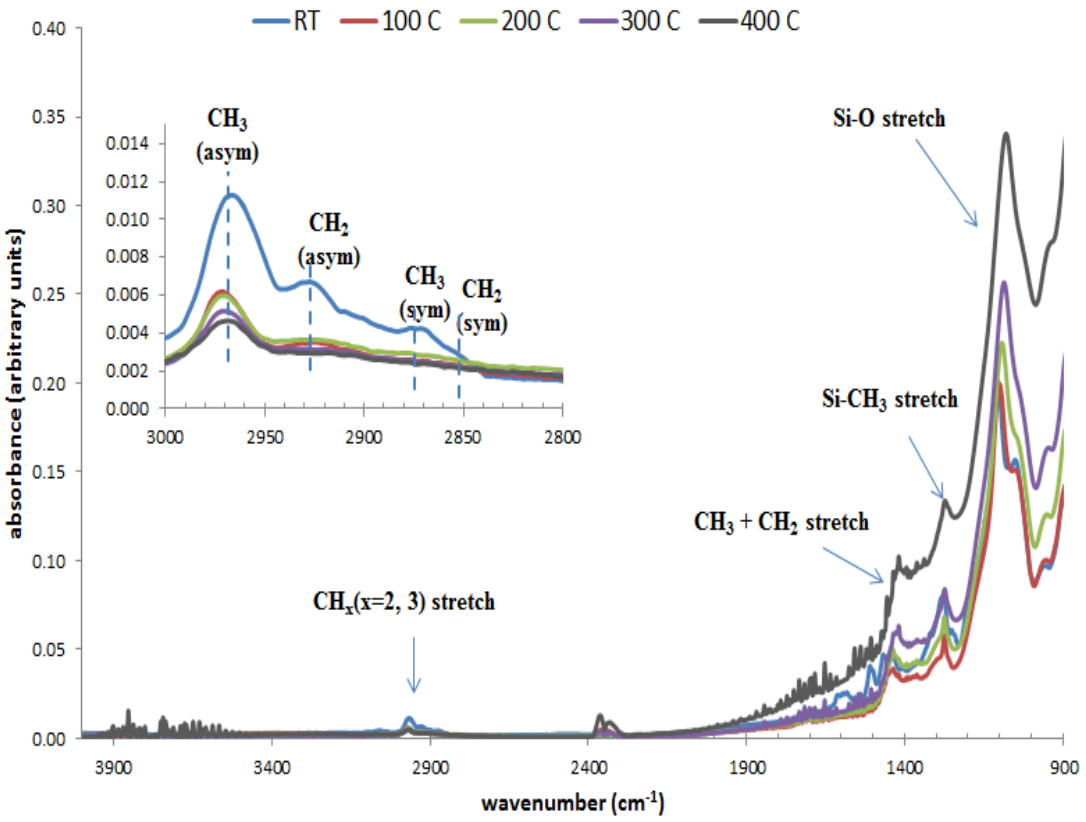

Fig. 5.4. FTIR transmission absorption spectra (CH_x peak insert) of the HMDS repaired He/O_2 30s plasma ashed SiOCH film as a function of temperature.

The SC-CO_2/HMDS treatment introduced some trimethylsilyls on the surfaces of the film. This is seen with the Si-CH_3 peak located at 1275 cm^{-1}. The peaks at around 1220 – 975 cm^{-1} are from the Si-O related stretching modes, and those at around 3010 – 2840 cm^{-1} are from the CH_x (x=2, 3) bending vibrations. As the treating temperature was increased, the intensity of the Si-CH_3 peak located at 1275 cm^{-1} decreased. There was also a decrease in the CH_x (x=2, 3) peaks especially the CH_3 (symmetric) and the CH_2 (symmetric) modes. This indicates the removal of hydrocarbons. But at 900 °C, only the CH_3 (asymmetric) mode remains. As can be seen in Fig. 4 above, as treatment temperature increases, there was a stretching of the CH_3+CH_2 stretch located at

approximately 1500 – 1350 cm^{-1}. Si-O stretching mode at around 3010 – 2840 cm^{-1} also reduced in intensity at increasing temperature. A de-convolution of the Si-O (Fig. 5.5) peak shows that the hump at around 1198 cm^{-1} which represents Si-C-O stretching with methyl/hydroxyl vibration modes intensity decreased until it was not possible to be detected at higher temperatures.

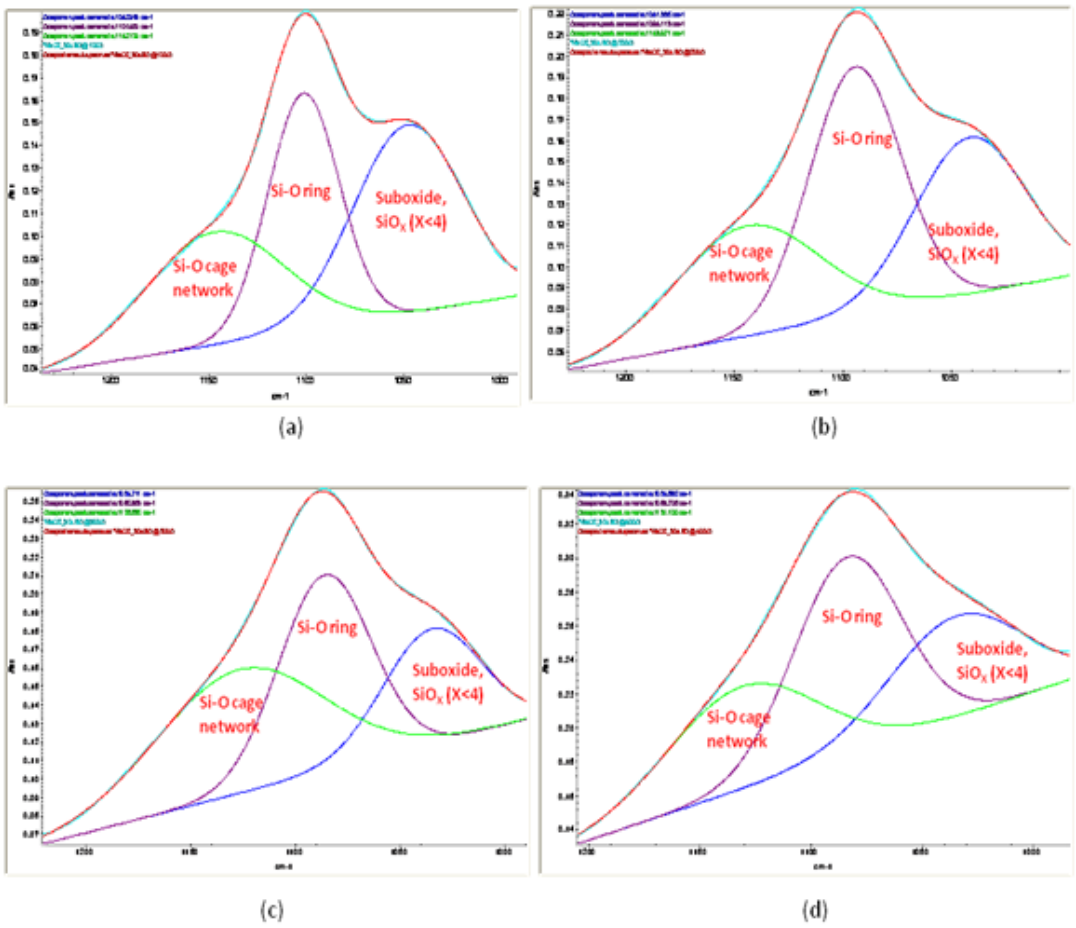

Fig. 5.5. De-convolution of the Si-O stretching band of HMDS repaired He/O_2 ash film at different heat treatments (a) 100 °C (b) 200 °C (c) 300 °C (d) 400 °C.

This increase in temperature causes shifts in the peaks. The peak shifts at 300 and 900 °C are the same.

Fig. 5.6 shows the variation of the FTIR absorption spectrum over the range of 4000 – 900 cm^{-1} of the repaired O_2 plasma ashed film at different temperature treatments. The insert peaks which is from 3010 – 2840 cm^{-1} representing the CH_x (x=2, 3) shows that as temperature increases, the intensity of the CH_3 (symmetric) and CH_2 (symmetric) reduced. At 400 °C, only the CH_3 (asymmetric) peak was detected at approximately 2962 cm^{-1}. Compared to the as-deposited blanket film, the strength of the methyl bonded to silicon is stronger for the as-deposited than the repaired film, as at around 300 °C the CH_3 and CH_2 (asymmetric) peaks could be detected but not for the repaired films. This is because the trimethylsilyls has three methyls bonded to a single silicon that is attached to the silica backbone while the "native" methyls are directly bonded to the silica-the trimethylsilyls are easier to remove than the "native" methyls. The Si-CH_3 stretch at around 1275 cm^{-1} also decreased in intensity and there was a change in the FWHM as temperature increased. These were due to the loss of unstable methyl groups and also because of the stretching of the bonds with increasing temperatures. The Si-O-Si stretch (1250 – 993 cm^{-1}) also decreases in intensity with increasing temperature. The positions of these peaks also vary with temperature; the positions of these peaks shifted to lower wavenumbers and these shifts are believed to be caused by changes in the bond angle [26].

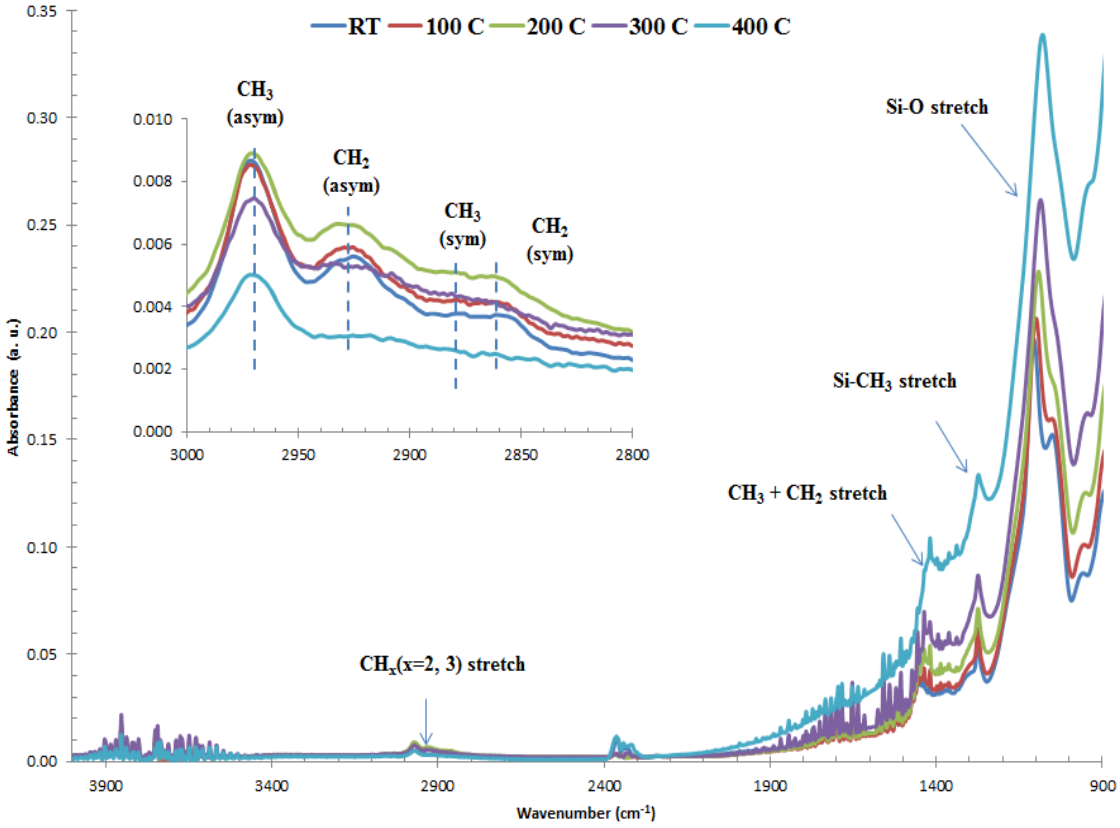

Fig. 5.6. FTIR transmission absorption spectra (CH_x peak insert) of the HMDS repaired O_2 plasma ashed SiOCH film as a function of temperature.

These were also observed in the repaired N_2/H_2 30 and 60 sec ashes (Fig. 5.7 and Fig. 5.8). As temperature increases the Si-CH_3 peak at 1275 cm^{-1} decreases in intensity and also the FWHM changes signifying changes in the bond due to stretching of these bonds.

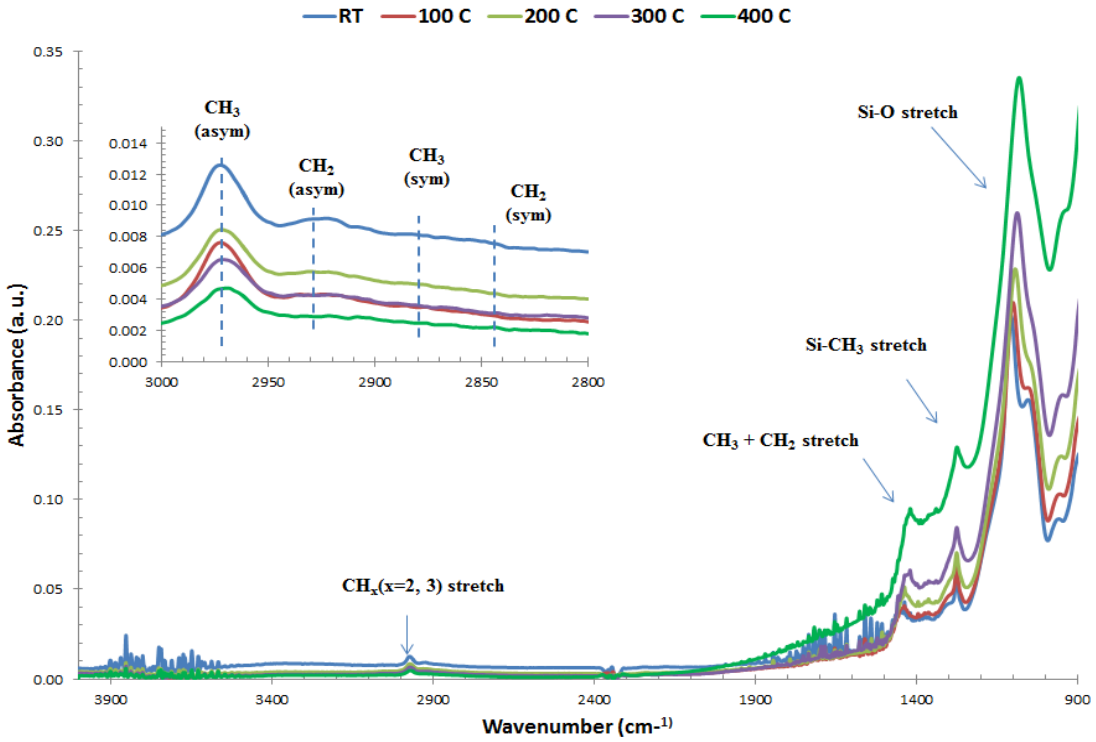

Fig. 5.7. FTIR transmission absorption spectra (CH_x peak insert) of the HMDS repaired N_2/H_2 30s plasma ashed SiOCH film as a function of temperature.

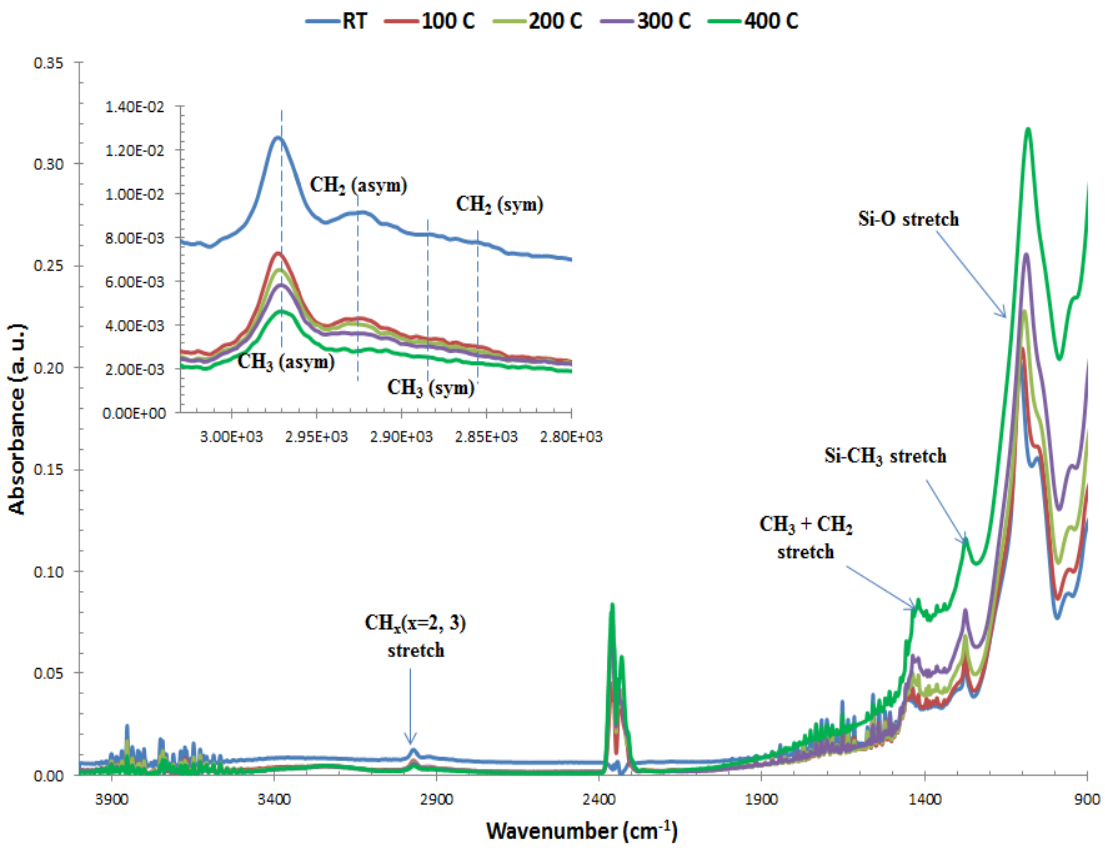

Fig. 5.8. FTIR transmission absorption spectra (CH_x peak insert) of the HMDS repaired N_2/H_2 60s plasma ashed SiOCH film as a function of temperature.

Figs. 5.9 and 5.10 show the FTIR transmission absorption spectra in the wave range of 4000 cm^{-1} – 900 cm^{-1} for the repaired He/O_2 and O_2 ashed damaged film using DEDMS as a function of varying temperatures. After the silylation process using DEDMS, silanol groups were replaced by dimethylsilyl. The coverage of DEDMS is different from HMDS because DEDMS can bond with two silanols rather than one and only has two methyl groups rather than three for HMDS. With increase in temperature, the Si-O related stretching modes at around 1220 – 975 cm^{-1}, lost the hump that is located at around 1198 cm^{-1} which represents Si-C-O stretching with methyl/hydroxyl vibration modes. This temperature increase also caused the $Si-CH_3$ located at around 1275 cm^{-1} to

decrease in intensity signifying the loss of hydrocarbons and also changes in the FWHM. The CH_x *(x=2, 3)* bending vibrations located at around 3010 – 2840 cm cm^{-1} shows only small significant amount of CH_3 (asymmetric) and CH_2 (asymmetric). The DEDMS shows a little effect of CH_3 loss than HMDS. This is because the two siloxane bonds in dimethylsilyls are stronger than one in trimethylsilyls.

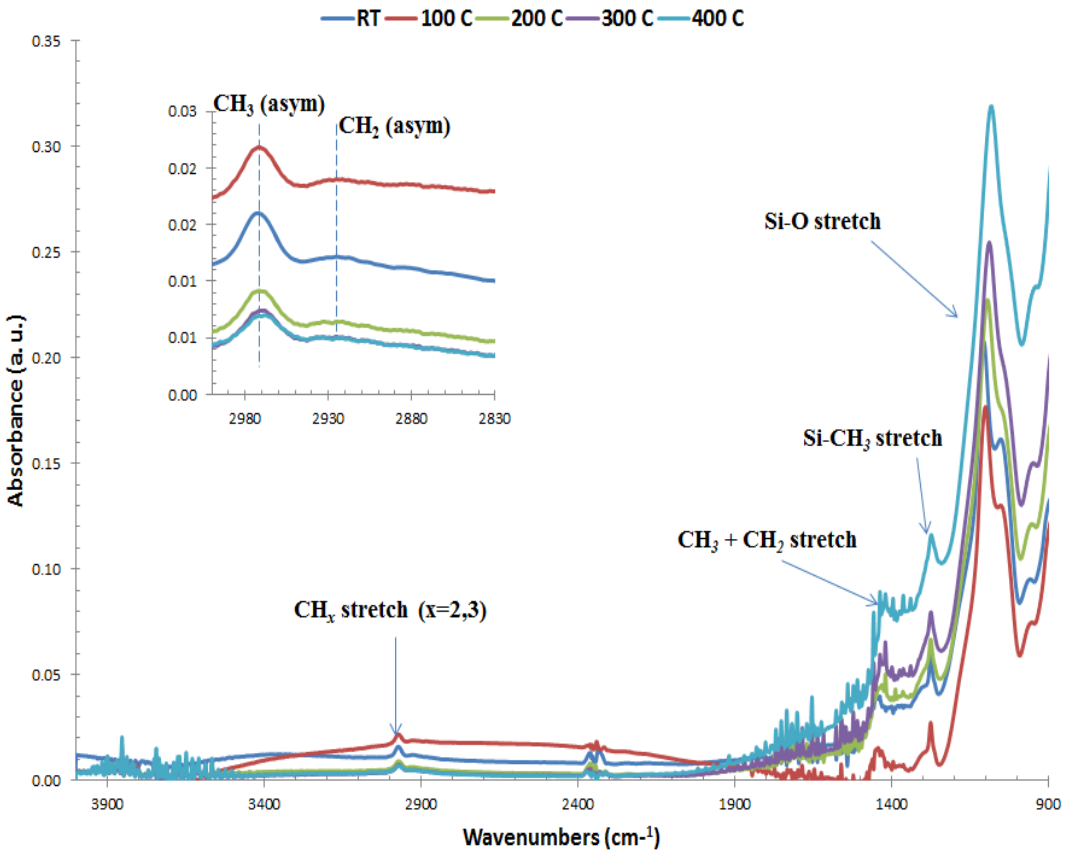

Fig. 5.9. FTIR transmission absorption spectra (CH_x peak insert) of the DEDMS repaired He/O_2 30s plasma ashed SiOCH film as a function of temperature.

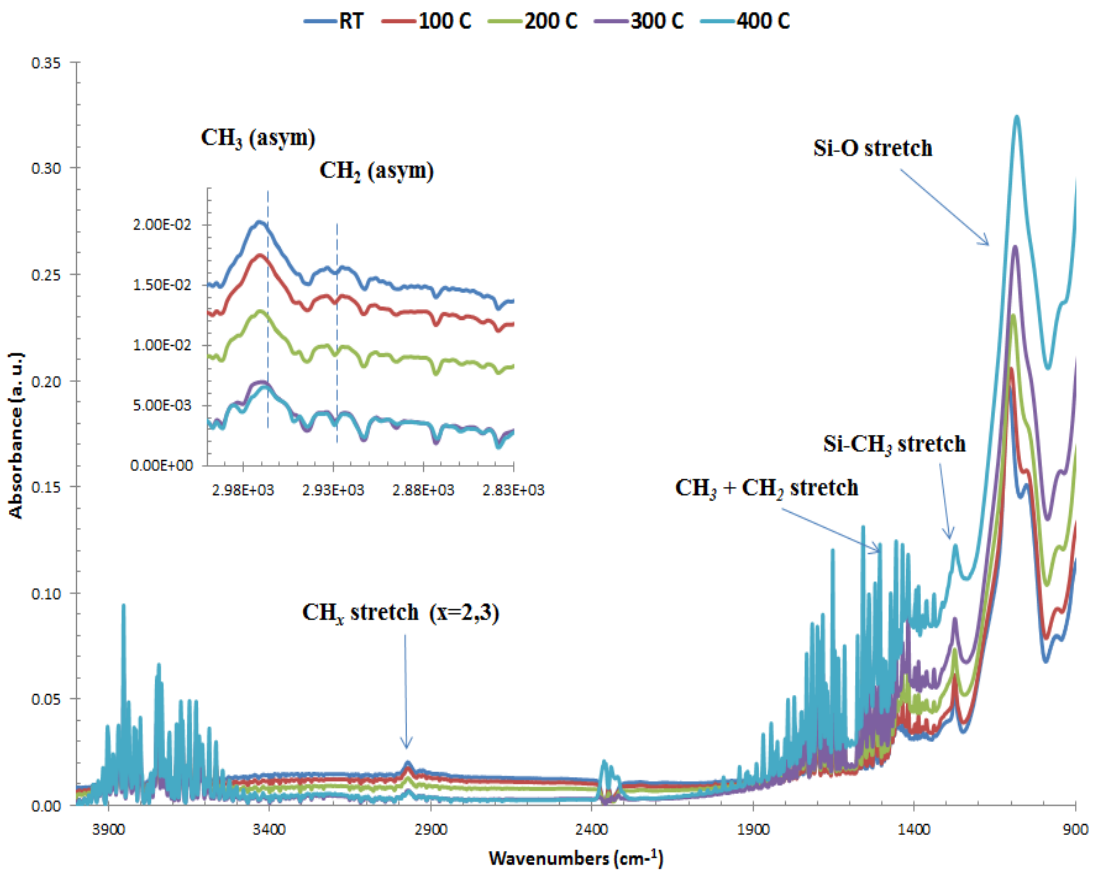

Fig. 5.10. FTIR transmission absorption spectra (CH_x peak insert) of the DEDMS repaired O_2 20s plasma ashed SiOCH film as a function of temperature.

The reducing plasmas of N_2/H_2 30s and 60s which are represented in Figs. 5.11 and 5.12 respectively show different results with regards to the CH_x *(x=2, 3)* stretch located at around 3010 – 2840 cm cm^{-1}. The oxidizing plasma damaged films of O_2 and He/O_2 showed only the presence of asymmetric CH_3 and CH_2 peaks, but the reducing plasmas of N_2/H_2 30s and 60s showed both asymmetric CH_3 and CH_2 peaks as well as the symmetric peaks of CH_3 and CH_2. In addition, the N_2/H_2 damaged films were easily repaired using DEDMS as the silylation agent. Further investigation is still ongoing as to why this was the case, but with increasing temperatures, methyl groups and concurrently

unstable hydrocarbons were lost, and also bond changes were observed which have been explained earlier in this work. It has been reported elsewhere that a temperature of 400 ºC, some mechanical properties of SiOCH film such as hardness and elastic modulus are affected indicating some change in the network bonding [27].

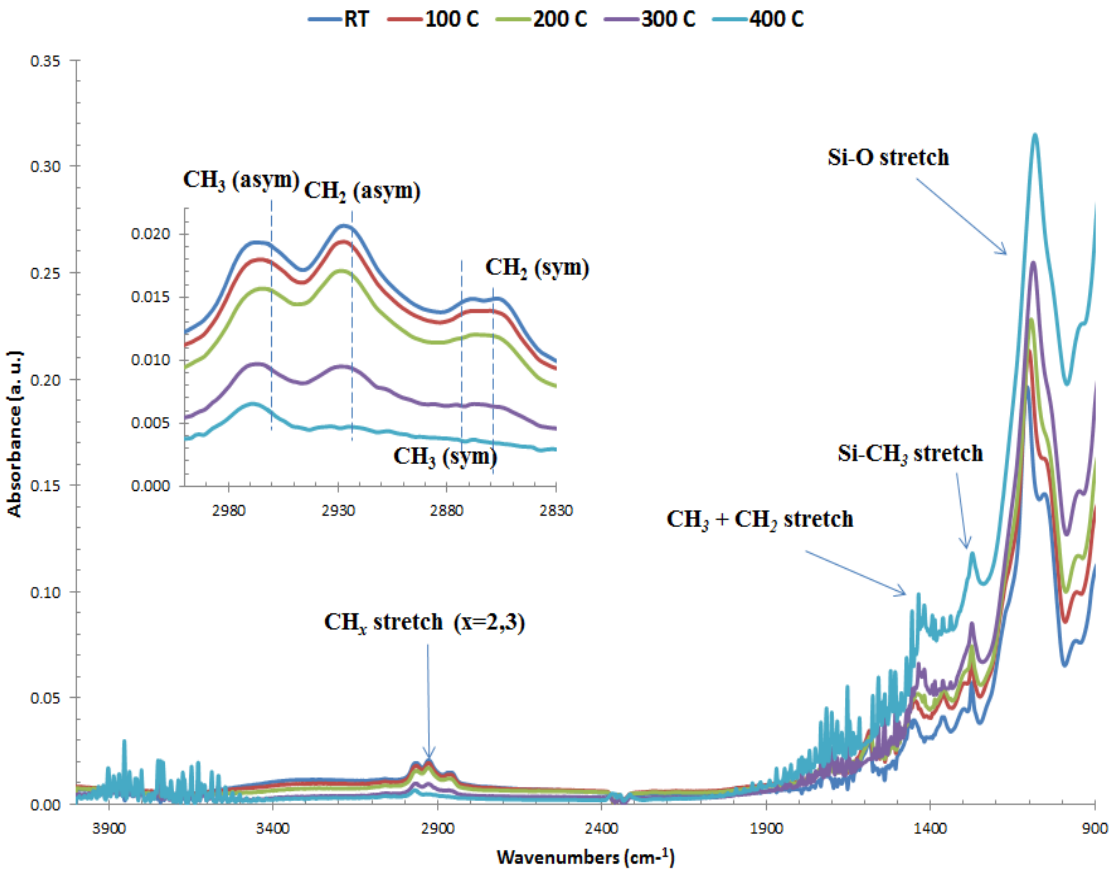

Fig. 5.11. FTIR transmission absorption spectra (CH_x peak insert) of the DEDMS repaired N_2/H_2 30s plasma ashed SiOCH film as a function of temperature.

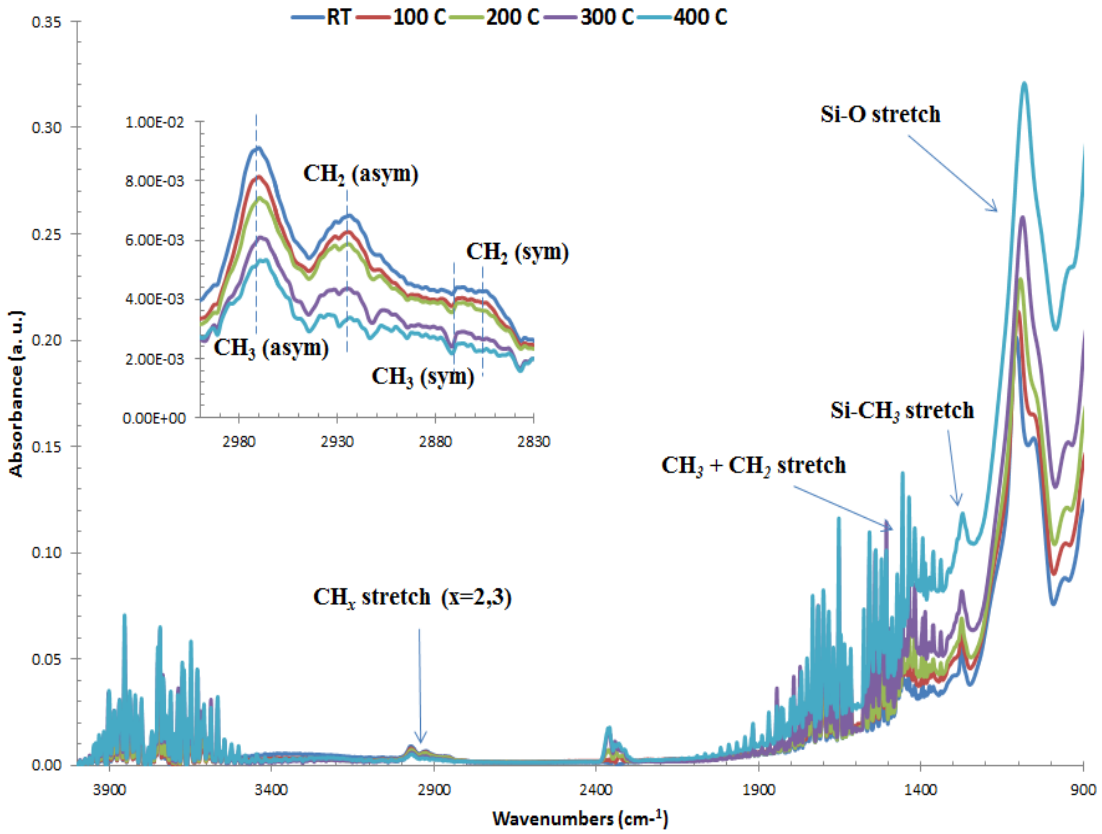

Fig. 5.12. FTIR transmission absorption spectra (CH_x peak insert) of the DEDMS repaired N_2/H_2 60s plasma ashed SiOCH film as a function of temperature.

5.3.2 XPS Analysis

Figs. 5.13, 5.14, and 5.15 give the XPS chemical composition for the films before and after SC-CO_2/HMDS repair and heat treatment. The deposited SiOCH film (Fig. 13) shows about 28% atomic composition of carbon which signifies the presence of methyl groups in the film, but after different plasma procedure, the carbon concentration dropped to about 6 atomic percent for the He/O_2, N_2/H_2 ashed processes, with O_2 ash showing just 3 percent carbon concentration. Clearly, the ash process rids the film of its surface and near surface hydrocarbon components. The loss of carbon leads to the creation of

hydroxyl groups in the film, which is verified by the relative increase in oxygen concentration.

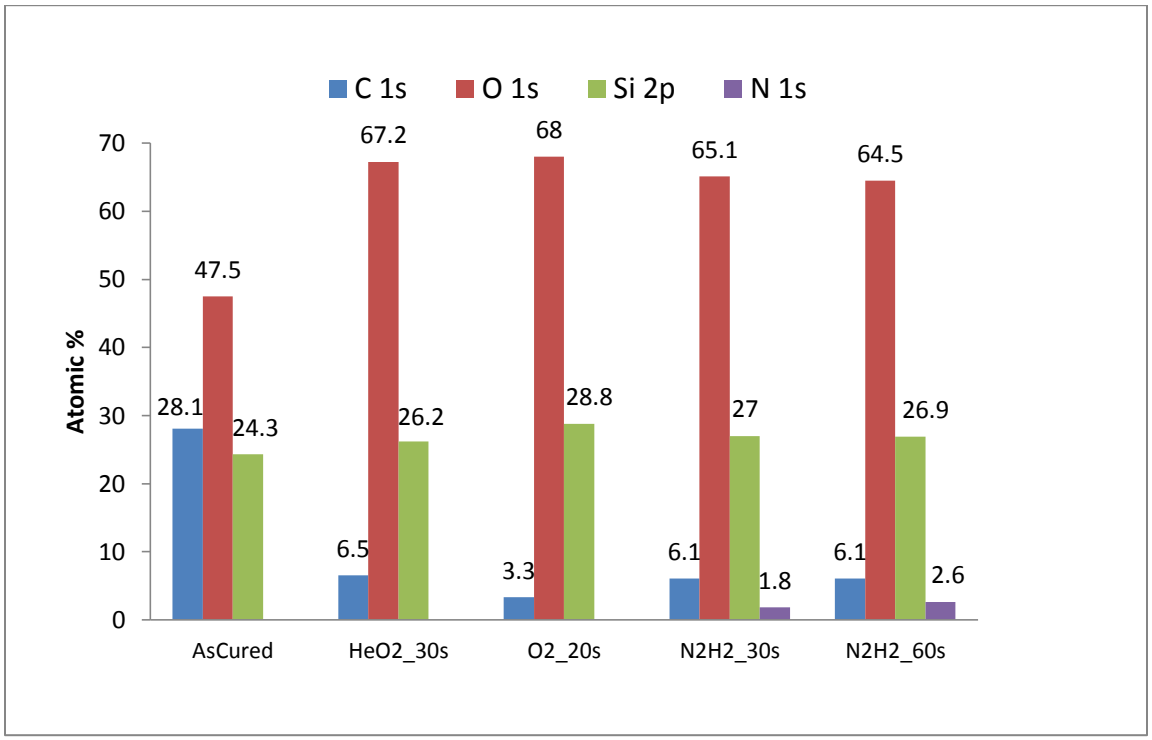

Fig. 5.13. XPS results for as-received ashed and unashed samples.

After SC-CO_2/HMDS treatments, Fig. 14(a), the carbon concentration of the ashed films increased because the repair process introduces trimethylsilyls to the film. The carbon concentration did not increase to the level of the unashed film because this silylation process occurs on the surface of the film and does not penetrate deeper. It is believed that the first few layers of trimethylsilyls deposited onto the surface seals the pores preventing the infiltration of others getting deep into the film. The He/O_2 showed about 12 atomic percent of carbon, O_2 showed 12 percent and N_2/H_2 30sec and 60sec showed about 11 and 13 atomic percent respectively. This is also observed after the SC-CO_2/DEDMS treatment (Fig. 14b) as the recovery is basically happening at the surface of the film.

Because DEDMS adds fewer methyls groups per reaction with a silanol compared to the HMDS, the carbon concentration after repair is marginally less than that of the HMDS treated film, aside the He/O_2 damaged film which showed about the same carbon concentration. In fact, because there are fewer methyl groups resulting from each silylation reaction with DEDMS (one methyl/reaction versus three methyls/reaction for HMDS), the number of silanols reacted is likely to be greater for DEDMS based on these results. The He/O_2 showed about 11 atomic percent of carbon, O_2 showed 9 percent, and N_2/H_2 30s and 60s showed about 9 and 11 atomic percent of carbon respectively.

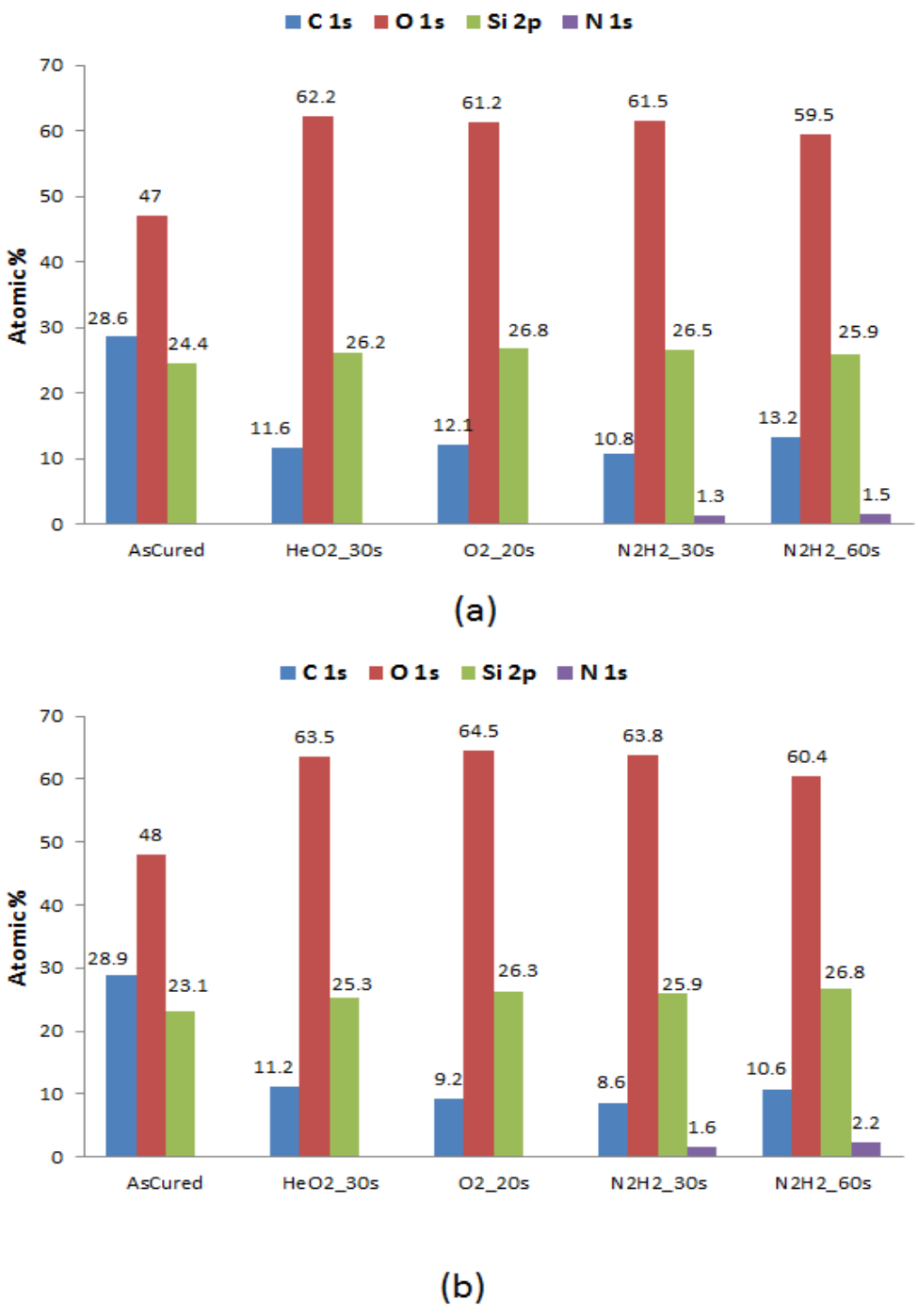

Fig. 5.14. XPS results for (a) SC-CO_2/HMDS repaired films and (b) SC-CO_2/DEDMS repaired films.

After heat treatment Figs. 15(a) and 15(b), for the HMDS and DEDMS respectively, the carbon and oxygen concentrations of all the films decreased because at higher temperatures, most of the hydrocarbons (trimethylsilyls and dimethylsilyls for the repaired films and methyls from the unashed films) are lost. This confirms the FTIR data which showed a decrease in the Si-CH_3, CH_x and Si-O stretching modes. Interestingly the small amount of nitrogen introduced during the N_2/H_2 plasma ashing appears to withstand heat treatments.

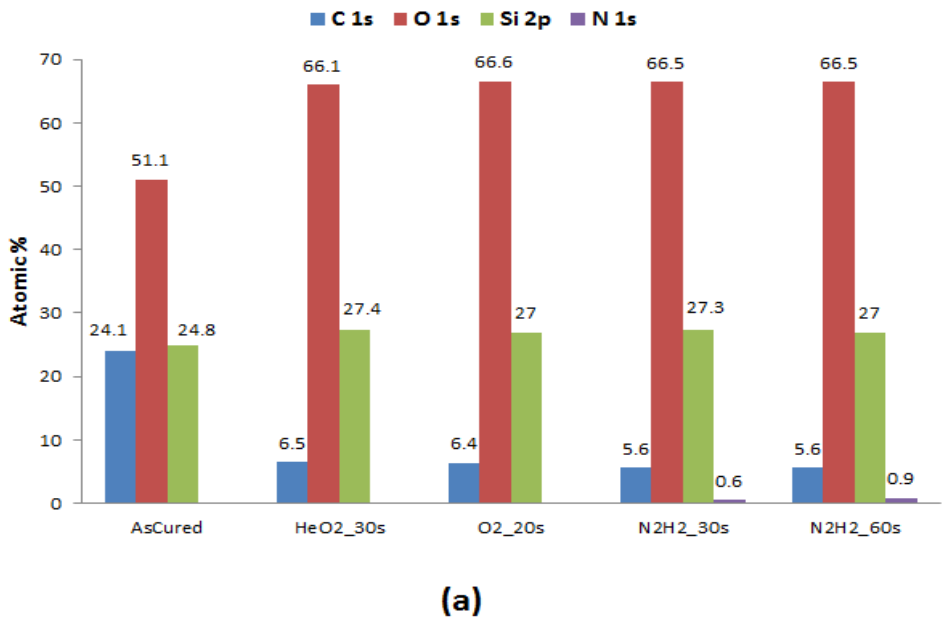

(a)

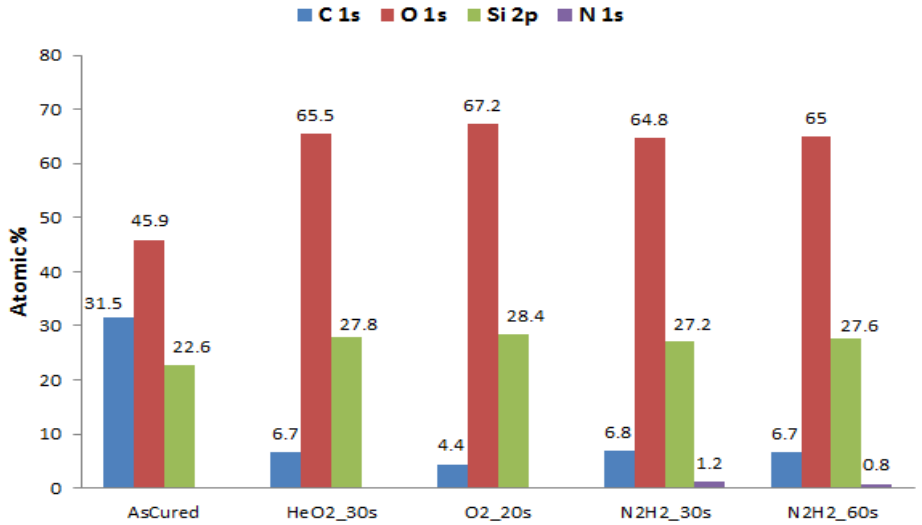

(b)

Fig. 5.15. XPS results after (a) SC-CO_2/HMDS repair and heat treatment and (b) SC-CO_2/DEDMS repair and heat treatment.

A comparison of the amount of carbon lost during heat treatment for the HMDS and DEDMS repaired films reveals that the dimethylsilyls introduced by DEDMS are more stable than the trimethylsilyls formed during HMDS treatments (Fig. 5.16). With the

exception of the O_2 ash film, all the other films show much less carbon loss for the DEDMS repaired films than the HMDS repaired films. This is logical since each dimethylsilyl has two groups that can react with silanols rather than only one in trimethylsilyls. The similarity of the carbon loss in the oxygen ashed films would suggest that something may be inhibiting the formation of two siloxanes during the silylation with dimethylsilyls. The silylation mechanism of dimethylsilyls requires the availability of two adjacent silanols to form both siloxanes. If a plasma process does not create as many silanols, then the probability of both siloxanes forming is less likely. In addition to silanols, oxygen ashing can create surface (bridged) siloxanes between adjacent silicons creating a surface with a mixture of silanols and siloxanes (prior to silylation). HMDS needs only one silanol to silylates, so the extent of the silylation reactions will be only somewhat affected. However, if DEDMS only forms one siloxane, then it is more weakly bonded than if it had formed two siloxanes and be as vulnerable to temperature driven removal as a trimethylsilyl (perhaps even weaker due to the unreacted alkoxy group). He/O_2 plasma ashed film lost lesser amount of carbon after both HMDS and DEDMS repair than O_2 ash film did. This might be due to the O_2 plasma creating siloxanes on the surface of the film even before the silylation process. This causes lesser amount of methyl groups to be formed on the film surfaces. The amount of carbon species lost for the oxygen ash film for DEDMS is more compared to HMDS because DEDMS needs two silanols to silylates so because of the formation of siloxanes on the film surface before silylation, DEDMS might have formed only one siloxane which makes it vulnerable to temperature.

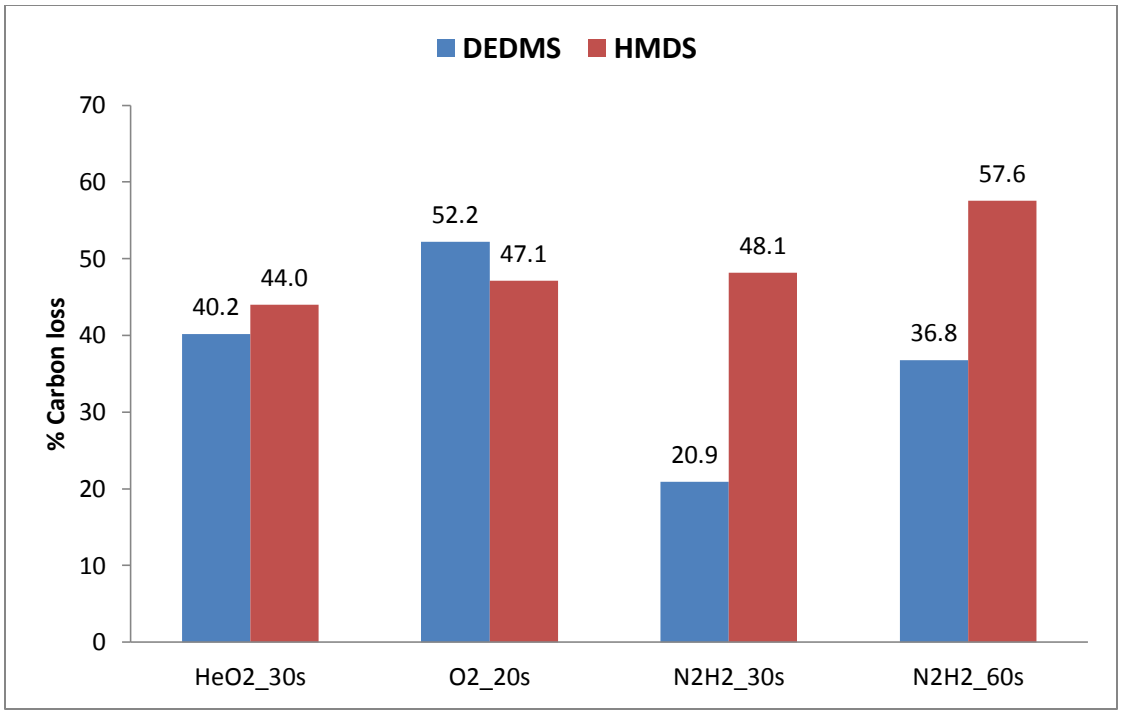

Fig. 5.16. Atomic % of carbon loss after SC-CO_2 (HMDS/DEDMS) and heat treatment.

5.3.3 Ellipsometry measurements

Spectroscopic ellipsometry is an indirect way of measuring the refractive index and the thicknesses of films. These films were modeled using a functionally graded Cauchy model. Comparatively, after the heat treatment, there were decreases in thicknesses for all the films. This is shown in Fig. 5.17a below. The decreases in thicknesses range from about 1 – 3 %. The unashed sample showed the least decrease in thickness because it has more stable methyl groups compared to the trimethylsilyls of the HMDS repaired film. This is because for the repaired films, the repair takes place on the surfaces of the films. Grill and Neumayer reported that the removal of the organic CH_x phase through the heat treatments causes a reduction of the film thickness [28].

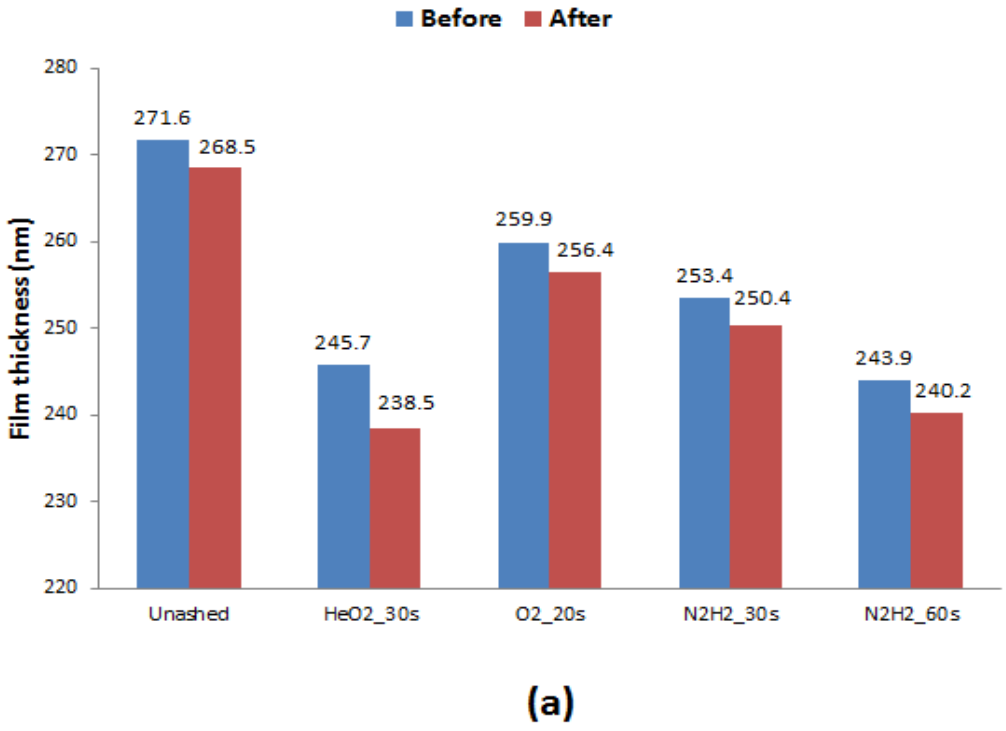

(a)

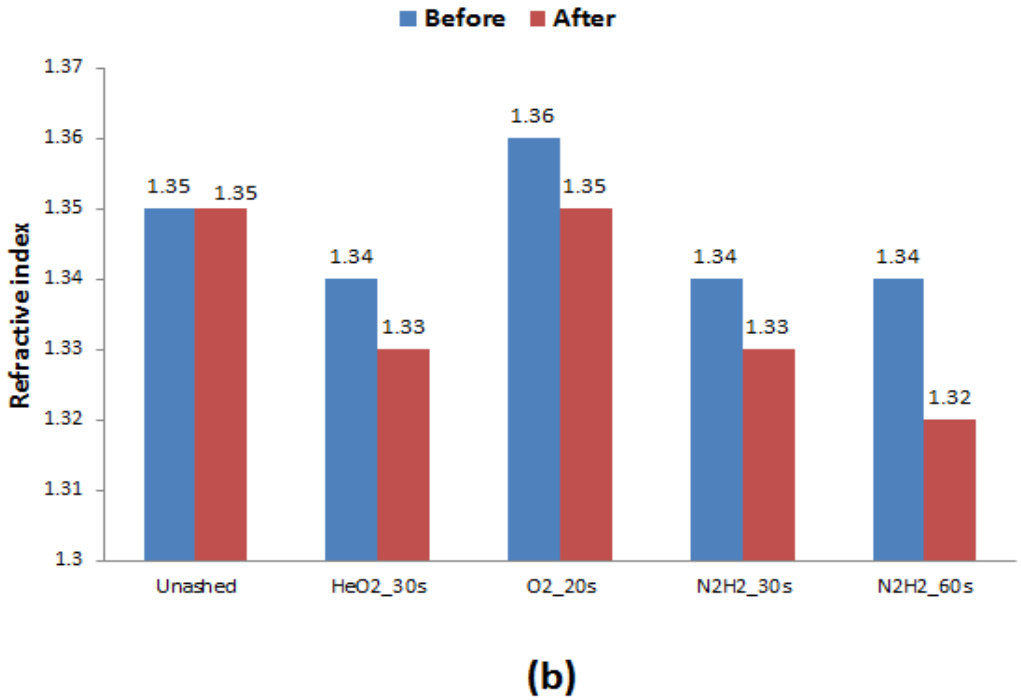

(b)

Fig. 5.17. Spectroscopic ellipsometer derived (a) film thickness and (b) refractive indices for SC-CO_2/HMDS repaired films before and after heat treatment.

The refractive indices were measured after temperature treatments (Fig. 17b). The refractive index of a film reflects the film's density. The higher the refractive index, the higher is the films density and vice versa [29]. With the exception of the as-deposited film, the refractive index of all the ash/repaired samples decreased after the heat treatment. These were also observed in the DEDMS repaired films which are given in Figs. 18(a) and 18(b) for the film thicknesses and refractive indices respectively. This might be due to an un-cooperative modeling.

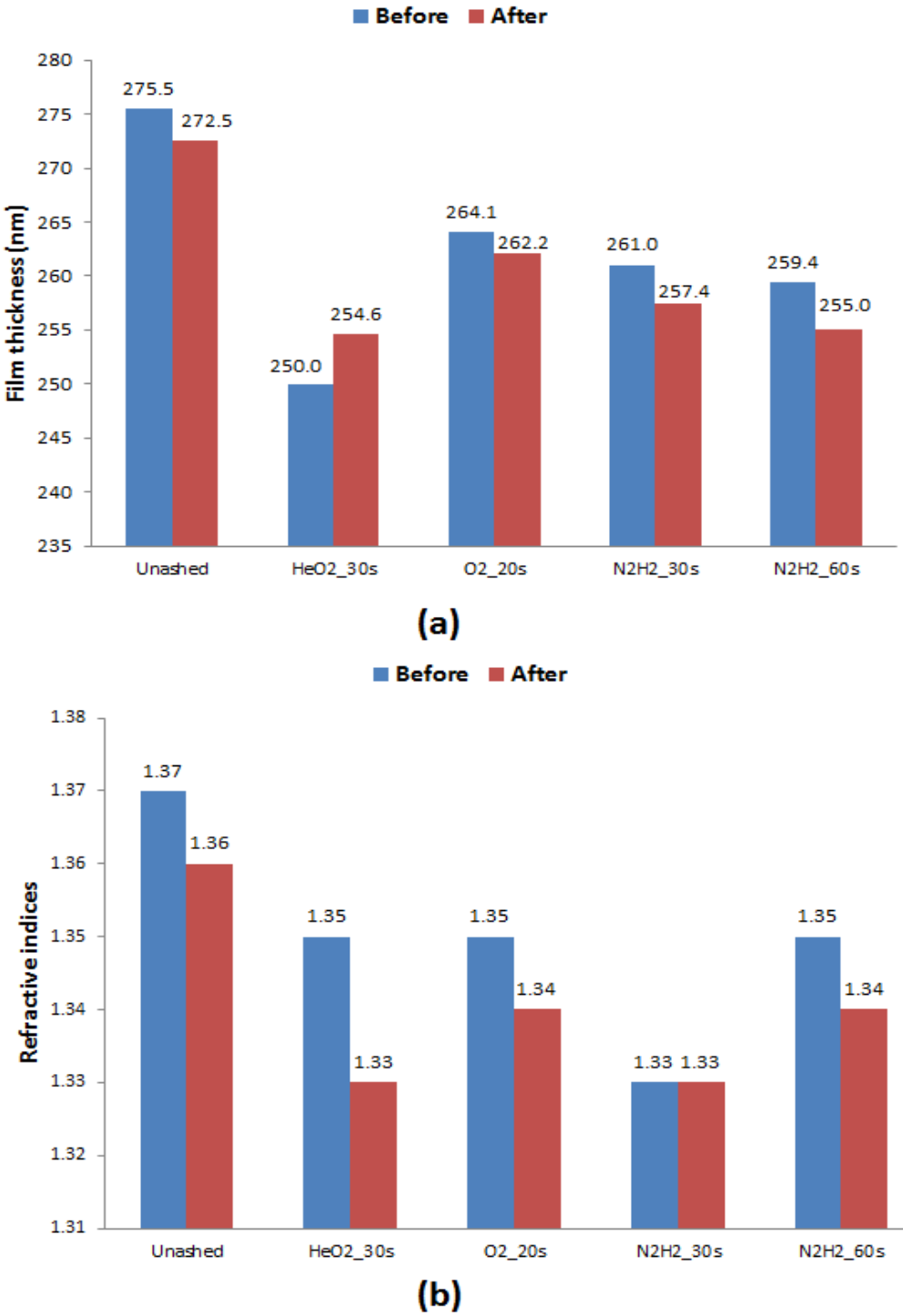

Fig. 5.18. Spectroscopic ellipsometer derived (a) film thickness and (b) refractive indices for SC-CO_2/DEDMS repaired films before and after heat treatment.

5.4 Conclusion

The effects of temperature treatments on unashed and repaired plasma ashed low-*k* CVD SiOCH films were investigated. The ashed films were repaired using SC-CO_2/HMDS and SC-CO_2/DEDMS treatment. Using an in-situ FTIR heat treatment, as the treatment temperature was increased from 25 to 400 °C, the intensity of the Si-O-Si peaks at (1250 - 993 cm^{-1}) decreases for both the as-deposited films and the ash repaired films. The infra-red analysis also shows a decrease of the Si-CH_3 stretch (1340 – 1250 cm^{-1}) and also C-H_x stretch (3100 – 2800 cm^{-1}) with increase in temperature. At even higher temperatures, CH_2 and CH_3 (symmetric) peaks are so limited they could not be detected. These were observed for both the HMDS and DEDMS repaired films. XPS data also shows a decrease in the carbon concentration with increasing temperature. The results described above shows that with increasing temperature, methyl groups are lost for the as-deposited films and trimethylsilyls are lost for the HMDS ash repaired films and dimethylsilyls for the DEDMS repaired films. Because of different coverage effects for HMDS and DEDMS, the carbon concentration was greater for the HMDS (as it has trimethylsilyls) repaired films than the DEDMS (have dimethylsilyls) repaired films. Comparison of the amount of carbon loss after the heat treatments for the HMDS and DEDMS repaired films showed HMDS losing a higher percentage than DEDMS. This shows that DEDMS better bonded than HMDS. As a result of the loss of carbon species, ellipsometry measurements also show a decrease in all the films thicknesses.

5.5 References

[1] M. Bohr, IEDM Tech. Dig. (1995) 241.

[2] J. Yang, C. Shim, and D. Jung, Japan J. Appl. Phys. 39 (2000) L 1324-L 1326.

[3] S. Lee, D. Jung, J. Yang, J. H. Boo, H. Kim, J. Lee, H. Chae, J Mater. Res. Vol. 23, No. 3 (2008) 856-861.

[4] A. Grill, V. Patel, J. Appl. Phys. 85 (1999) 3314.

[5] T. K. S. Wong, B. Liu, B. Narayanan, V. Ligatchev, R. Kumar, Thin Solid Films 462-463 (2004) 156-160.

[6] A. Grill, V. Patel, Appl. Phys. Lett. 79 (2001) 803.

[7] A. Grill, and D. Neumayer, J. Appl. Phys. 94 (2003) 6697.

[8] J. Lubguban Jr., and T. Rajagopalan, J. Appl. Phys 92 (2002) 1033.

[9] J. Yang, S. Lee, H. Park, D. Jung, and H. J. Chae, J. Vac. Sci. Technol. A 24 (2006) 165.

[10] J. Yang, C Shim, D. Jung, J. Mater. Res. 17 (2002) 1248.

[11] S. Lee, J. Yang, S. Yeo, J. Lee, D. Jung, J. Boo, H. Kim, H. Chae, Japanese J. of Appl. Phys. 46 (2007) 536-541.

[12] Y. Lin, T. Y. Tsui, J. J. Vlassak, J. Electrochem. Soc. 153 (2006) F144.

[13] T. Nakano, K. Tokunaga, T. Oannealinga, J. Electrochem Soc. 142 (1995) 1303.

[14] W. C. Ee, K. Y. Cheong, Physica B403 (2008) 611-615.

[15] Brinker, C. J., Scherer, G. W., Sol-Gel Science, The Physics and Chemistry of Sol-Gel Processing, Academic Press, San Diego, 1990.

[16] A. V. Rao, E. Nilsen, M. A. Einarsrud, J. Non-Cryst. Solids 296 (2001) 165.

[17] N. Yamada, T. Takahashi, J. Electrochem. Soc. 147 (2000) 1477.

[18] A. L. Smith, Spectrochem. Acta16 (1960) 87.

[19] J. Workman, Handbook of Organic Compounds: NIR, IR, Raman, and UV-Vis Spectra Featuring Polymers and Surfactants, Methods and Interpretations, vol. 1, Academic Press, San Diego, 2001.

[20] S. V. Nitta, V. Pisupatti, A. Jain, P. C. Wayner Jr., W. N. Gill, J. L. Plawsky, J. Vac. Sci. Technol. B 17 (1999) 205.

[21] G. Socrates, Infrared Characteristics Group Frequencies, John Wiley, New-York NY, 1980.

[22] S. Lee, J. Yang, S. Yeo, J. Lee, D. Jung, J. Boo, H. Kim, H. Chae, Japanese J. of Appl. Phys. 46 (2007) 536-541.

[23] S. Lee, J. Yang, S. Yeo, J. Lee, D. Jung, J. Boo, H. Kim, H. J. Chae, J. Mater. Res. 23 (2008) 865-861.

[24] G. Lucovsky, M. J. Manitini, J. K. Srivastava, E. A. Irene, J. Vac. Sci. Technol. B, 5 (2), (1987) 530.

[25] T. K. S. Wong, B. Liu, B. Narayanan, V. Ligatchev, R. Kumor, Thin Solid Films 156 (2004) 462-463.

[26] G. L. Lucovsky, M. J. Manitini, J. K. Srivastava, E. A. Irene, J. Vac. Sci. Technol. B 5 (1987) 530.

[27] S. Lee, J. Yang, S. Yeo, J. Lee, D. Jung, J. Boo, H. Kim, H. Chae, J. Mater. Res. 23 (2008) 865-861.

[28] A. Grill, and D. J. Neumayer, J. Appl. Phys. 94 (2003) 6697.

[29] L. Han, J. S. Pan, S. M. Chen, N. Balasubramanian, J. Shi, L. S. Wong, and P. D. Foo, J. Electrochem. Soc. 148 (2001) F148.

CHAPTER 6

SURFACE MODIFICATION AND UV-CURING OF LOW-K POROUS FILMS

6.1 Introduction

The continuous shrinkage in the dimensions of ultra-large scale integrated circuit (ULSI) has called for the replacement of the conventional back-end-of-the line (BEOL) dielectric materials, in other to reduce the permittivity. Many of these materials that have a low dielectric constant are but not limited to spin-coated organic polymers [1], silsesquioxanes [2], templated sol-gel silicas [3], chemical vapor deposited carbon [4], and fluorine doped silicon oxide [5]. The dielectric constants of the inorganic films can be reduced by introducing chemical substituents such as alkyl (CH_3) groups. Even though the introduction of alkyl groups reduces the dielectric constant, research has shown that this strategy does not lower *k* below 2.5 [6]. However, to further decrease the dielectric constant, nano-level pores or voids are incorporated into the dielectric matrix during ULSI fabrication. One such film that has been studied to be used as interlayer dielectric application is the porous carbon-doped oxide dielectric (SiOCH). An increase in these nano-level pores results in fewer Si-O bonds than in fully dense SiOCH materials and, hence, a degradation in the mechanical strength. To avoid peeling or cracking of the film during chemical mechanical polishing (CMP) processes, an inter-connected porous oxide

with high mechanical strength is required necessitating careful selection of the fabrication of the porous low-*k* [7].

To transfer pattern into low-*k* films, plasma dry etch techniques are used because of the high anisotropy of the process. Plasma treatment is also used in post-etch treatment, such as etch residue cleaning or resist strip. These traditional plasma ash processes using either reducing or oxidizing chemistries significantly damage the low-*k* material by depleting the carbon atoms in the film through Si-C bond attack, creating dangling bonds defects, and film densification. This damage usually results in the replacement of hydrophobic methyl groups with hydrophilic hydroxyl (-OH) species. This increases adsorption of water and other deleterious chemicals. Elimination of the water and silanol from these high surface area materials can be accomplished by chemical modification of the silica surfaces created during plasma processing. Silylating agents such as trimethylchlorosilane (TMCS) [8,9,10] or hexamethyldisilazane (HMDS) [11] have been used to replace surface hydroxyls. Silylating agents have thus shown to recover surface hydrophobicity and to prevent water and precursor moieties from intruding into porous silica-based low-*k* films and also preventing thickness losses during wet etch/cleans.

Ultra-violet (UV) irradiation curing has shown to be the most promising method for increasing the mechanical strength of low-*k* SiOCH materials. It can also be used to reduce the dielectric constant of low-*k* materials it does not always do that-often increases *k*. Because the silylating species react most effectively within the few 20 Å of the film surface, these species may readily react with UV radiation to form very thin barrier

layers. A UV light source emits energy in the form of photons, and the energy delivered is inversely proportional to the wavelength of the light source. With UV curing, the cross-linking kinetics can be enhanced by just increasing the intensity of the UV.

In this study, plasma-ash films repaired by supercritical CO_2 (SC-CO_2)/tetramethylorthosilicate (TMOS) are subjected to UV curing. The effect of UV cure on the silylating species is investigated because as these silylating species react most effectively within 20 Å, it is believed that these species may readily react with UV radiation to form very thin barrier layers. The thin barrier layers can act as a protective layer for the films to be able to prevent the intrusion of metallic barrier precursors and other undesirable species.

6.2 Experiment

CVD SiOCH low-*k* films which were synthesized from ringed siloxane compounds and molecular templates were used in this work. The films have a nominal thickness of approximately 250 nm, a porosity of approximately 28%, and a dielectric constant (*k*) of approximately 2.35. The films were exposed to 30 s He/O_2, 20 s O_2, 30 and 60 s N_2/H_2 plasma ash treatments. These wafers were then cleaved in multiple pieces. Samples from each of the plasma conditions were subsequently treated with supercritical CO_2 containing TMOS ($Si(OCH_3)_4$) for about 5 minutes. The films were then exposed to UV irradiation using an Omnicure Series 2000 UV source having a maximum UV lamp power of 200 W and a wavelength range of 320-500 nm. This UV source has an iris setting of 0-100% which corresponds to irradiance level of 0.2 W/cm^2 – 40 W/cm^2. A

10% iris setting was used which corresponds to an irradiance level of approximately 4 W/cm^2. UV curing time ranged from 0 to 10 min with the film positioned approximately 50 mm from the UV source. Atomic force microscopy was used to study the surface topography of the films before and after SC-CO_2 TMOS and UV curing. AFM scans were performed using the tapping mode on a Veeco Multimode AFM with Nanoscope IIIa controller. The typical scan rate was 0.5 Hz with 512 samples per line at a 1 μm^2 scan size.

The film thicknesses and densities were measured using a JA Woollam variable angle spectroscopic ellipsometer (VASE) and functionally graded layers were used to model them. Nexus-470 Fourier transform infra-red (FTIR) spectrometer was used to verify the changes in bond chemistry of the films while an x-ray photoelectron spectrometer (XPS) PHI 5000 Versa probe was used to study the film surface compositions before and after each process.

6.3 Results and Discussion

6.3.1 FTIR

The FTIR spectra of SiOCH low-*k* films were taken before and after being irradiated by UV light following SCCO_2-TMOS treatment, to analyze the structure changes in the films. Fig. 6.1 shows the FTIR spectra of the unashed film cured for 0, 2, 5 and 10 min with UV radiation in the wavelength range between 900 and 4000 cm^{-1}.The peaks of interest are the absorption by Si-O and Si-CH_3 located at approximately 995-1300 cm^{-1},

Si-OH stretching vibration (isolated) at approximately 3750 cm^{-1} and CH_x(x=2,3) stretch at approximately 2840-3010 cm^{-1}.

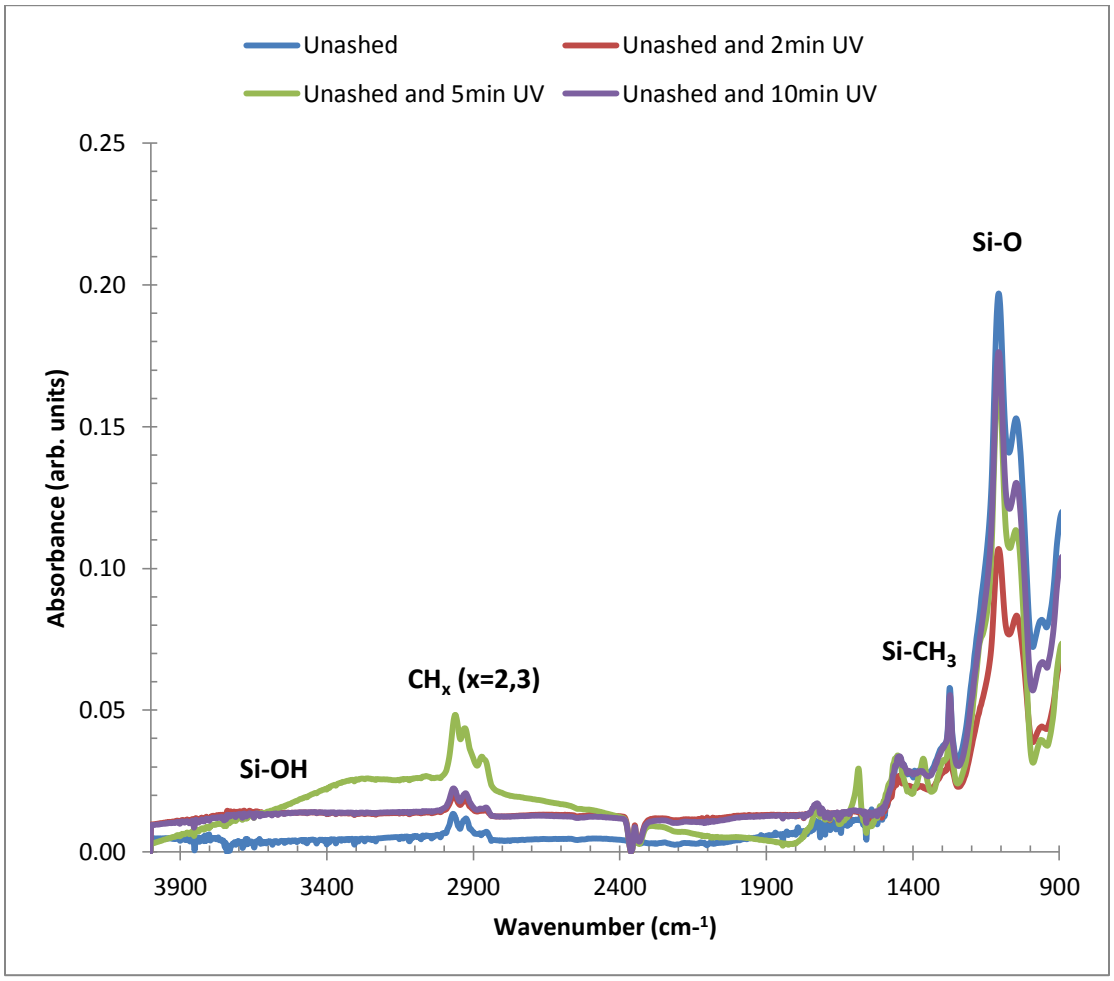

Fig. 6.1. FTIR spectra of unashed low-k film after different UV irradiation times.

With an increase in UV curing time, unexpectedly the absorption by CH_x (x=2, 3) increased especially after the 10 min UV treatment. The $Si-CH_3$ stretch located at approximately 1275 cm^{-1} did not show much decrease except for the 2 min cured sample which showed a significant decrease of the peak. This is consistent with the CH_x stretch where the 2 min cure seemed to have more impact on the removal of the unstable methyl

groups. This can be attributed to the possibility of inhomogeneous distribution of methyl groups on the film surface compared to deep within the sample. The Si-O stretch shows that 2 min curing time have more effect on the Si-O stretch than the other curing times. A de-convoluted peak for the Si-O stretch (Fig. 6.2) shows four peaks; the sub-oxide (SiO_x, x<4), Si-O ring, Si-O cage network, and the Si-C-O stretch with methyl vibrations located at approximately 1048, 1106, 1142 [12], and 1193 cm^{-1} respectively.

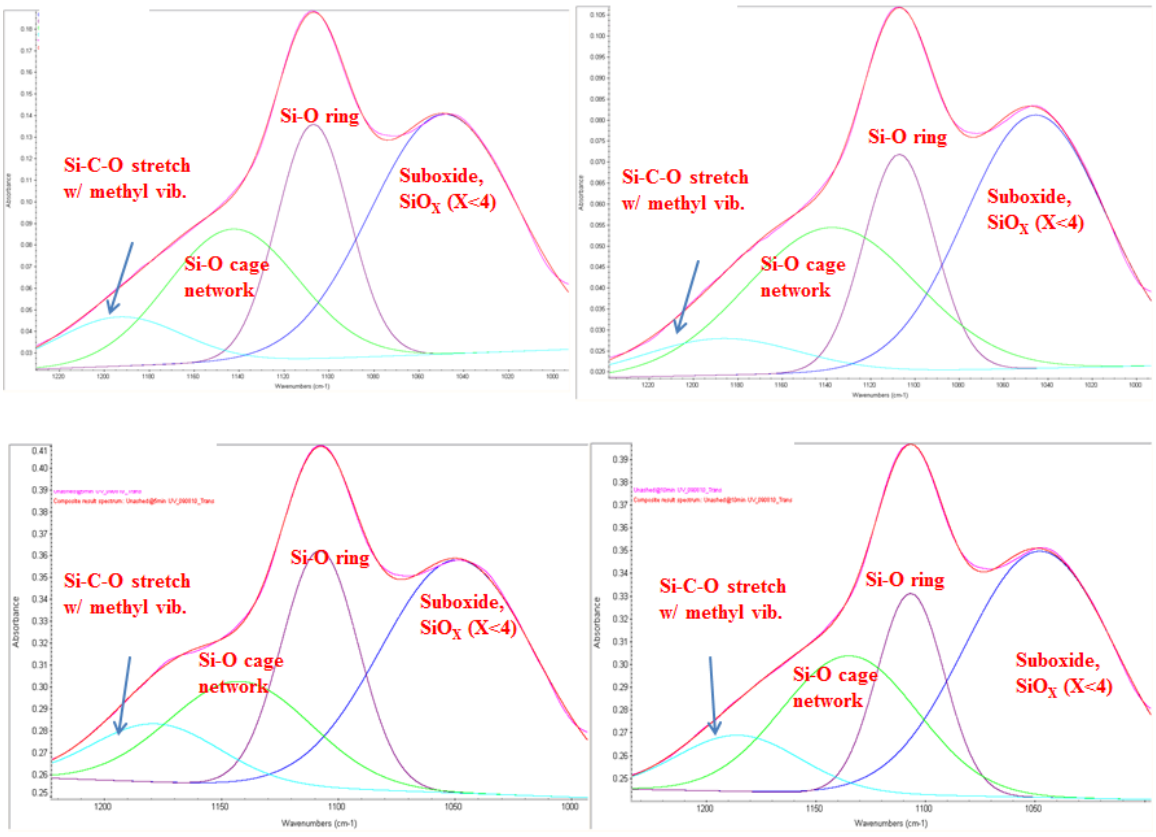

Fig. 6.2. De-convoluted Si-O stretch for unashed films after UV cure.

The bond angle of the cage-like structure is approximately 150° [13], while the network structure is reported to be 144° [14]. Aside from the 2 min cure where the sub-oxide peak area decreased, the peak area increased with increasing time for the 5 and 10 min cures

respectively. It is assumed that the C atom in CH_3 bonds is not only removed from the film, but also become integrated into the Si-O network [15]. This can lead to an increase in the low-*k* density. The increase of the Si-C-O with a decrease in methyl groups indicates the C atoms from the removed CH_3 have become incorporated into the film. The Si-O ring at around 1106 cm^{-1} decreased for the 2 min UV cure and marginally increases for 5 and 10 min cure times. This suggests that 6-hold ring of Si-O bond increases [15]. The Si-O cage network centered at around 1142 cm^{-1} decreased with increased UV cure time.

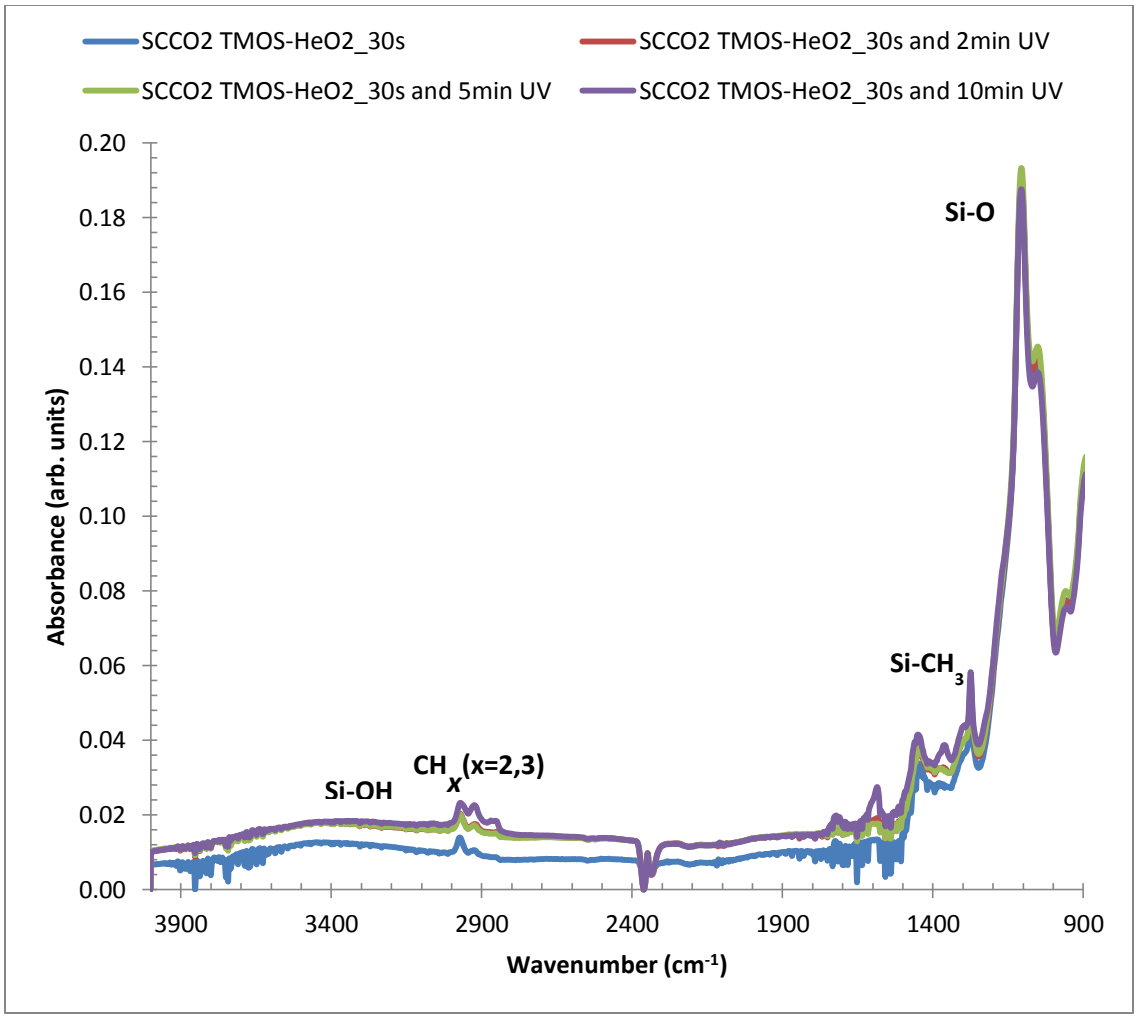

Fig. 6.3. FTIR spectra of repaired plasma He/O_2_30s low-k film after different UV irradiation times.

Fig. 6.3 shows the FTIR transmission spectrum ranging from 900-4000 cm^{-1} for the He/O_2_30s ash damaged film which was repaired using SC-CO_2/TMOS. The Si-O absorption stretch in this spectrum, located at approximately 1000-1250 cm^{-1} shows only a marginal decrease with increasing UV cure time. The de-convoluted peak for the Si-O absorption stretch show an increase in the Si-C-O peak with increasing UV cure time. As has been noted earlier an increase of the Si-C-O peak has been thought of as the

beginning of the transformation of the low-*k* film. All other peaks, namely the Si-O ring, Si-O cage network, and the sub-oxide SiO_x ($x < 4$) did not change within error. The CH_x ($x = 2,3$) stretch at approximately 2840-3010 cm^{-1} decreased with an increase in UV time up to 5 min and abruptly increase at 10 min. This can be as a result of the UV source removing all the available CH_3 bonds available on the surface that were deposited after the SC-CO_2/TMOS treatment. Hence after 10 min, it is possible the UV was able to readily react with the silylating species thereby incorporating it into the bulk film. The FTIR transmission spectrum ranging from 900-4000 cm^{-1} for the O_2_20s ash damaged film repaired using SC-CO_2/TMOS (Fig. 6.4) shows a decrease in the CH_x (x=2, 3) peak intensity for the 2 and 10 min treatments, but increased for the 5 min cure time. After de-convolution of the curve, it was again observed the sub-oxide peak again showed an increase with increases in curing time. Increases in curing time also caused the absorption by cage type Si-O to increase, while the absorption by the Si-C-O with methyl vibrations increased a little. It can be thought of that the C atom from the removed CH_3 bonds were not incorporated in the Si-O network as was observed in other samples. This could be due to the presence of bridge siloxanes on the film surface that limit the TMOS reaction. The Si-CH_3 stretch centered at approximately 1275 cm^{-1} also saw a reduction in the peak especially after 5 min UV exposure, but increased again for the 10 min. This result could be because silylation or recovery process takes precedence in the first few nanometer of the film surface; therefore exposure to UV for a longer time can rid the films surface of the methyl groups deposited by TMOS, and then exposes the methyl groups embedded in the film.

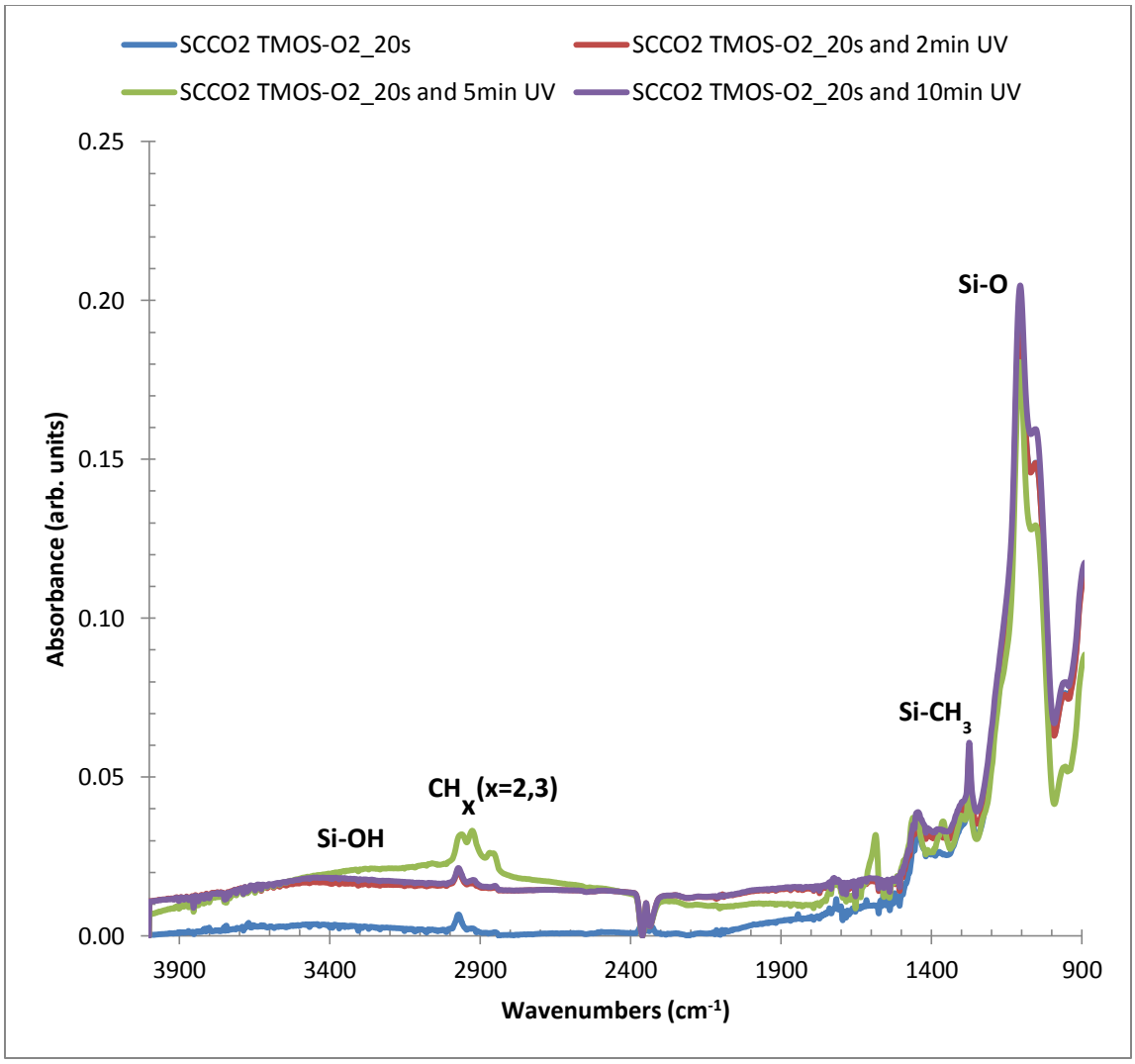

Fig. 6.4. FTIR spectra of repaired plasma O_2_20s low-k film after different UV irradiation times.

After the recovery process for the plasma damaged N_2/H_2_30s thin film, the film with no UV exposure and 5 min UV exposed showed similar amounts of CH_x (x=2, 3) while the 2 and 10 min UV exposed films showed increases in the CH_x peaks, which was observed in the FTIR spectra (Fig. 6.5). The effect of UV cure on the Si-O stretch is

different for this film than the others because, as with an increase in UV cure time a decrease in the Si-O peak was observed.

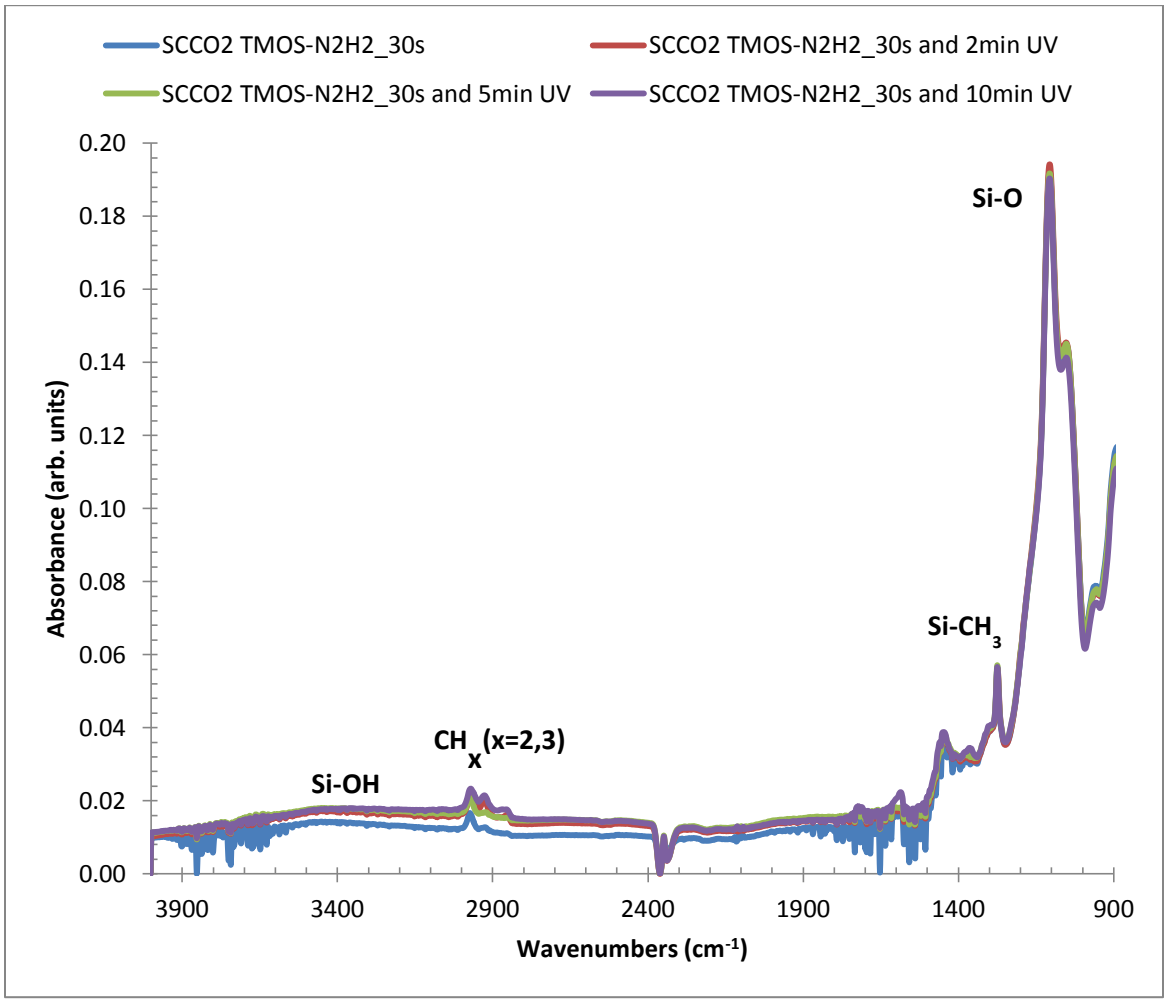

Fig. 6.5. FTIR spectra of repaired plasma N_2/H_2_30s low-*k* film after different UV irradiation times.

A de-convolution of the Si-O stretch showed an increase in the sub-oxide peak after 2 min, but any further increase in UV cure times (5 and 10 min) showed a decrease. The Si-C-O stretch with methyl vibration centered at approximately 1205 cm^{-1} increased with increase in UV cure times. This shows that the transformation of the low-*k* film started [15] after 2 min UV cure time and there was no further transformation after that. This is

possibly due to the loss of C atoms in the films resulting from the removal unstable methyl groups. There was no apparent change in the Si-O ring and the Si-O cage network peaks. The FTIR transmission spectrum ranging from 900-4000 cm^{-1} for the N_2/H_2_60s ash damaged film repaired using SC-CO_2/TMOS (Fig. 6.6) showed that after the recovery process and several UV cure times, there was no change in the CH_x (x=2, 3) peak after the 10 min UV cure, but at 5 min, there was a decrease, and 2 min showed an increase. Ultimately, there was no change regardless of the duration time.

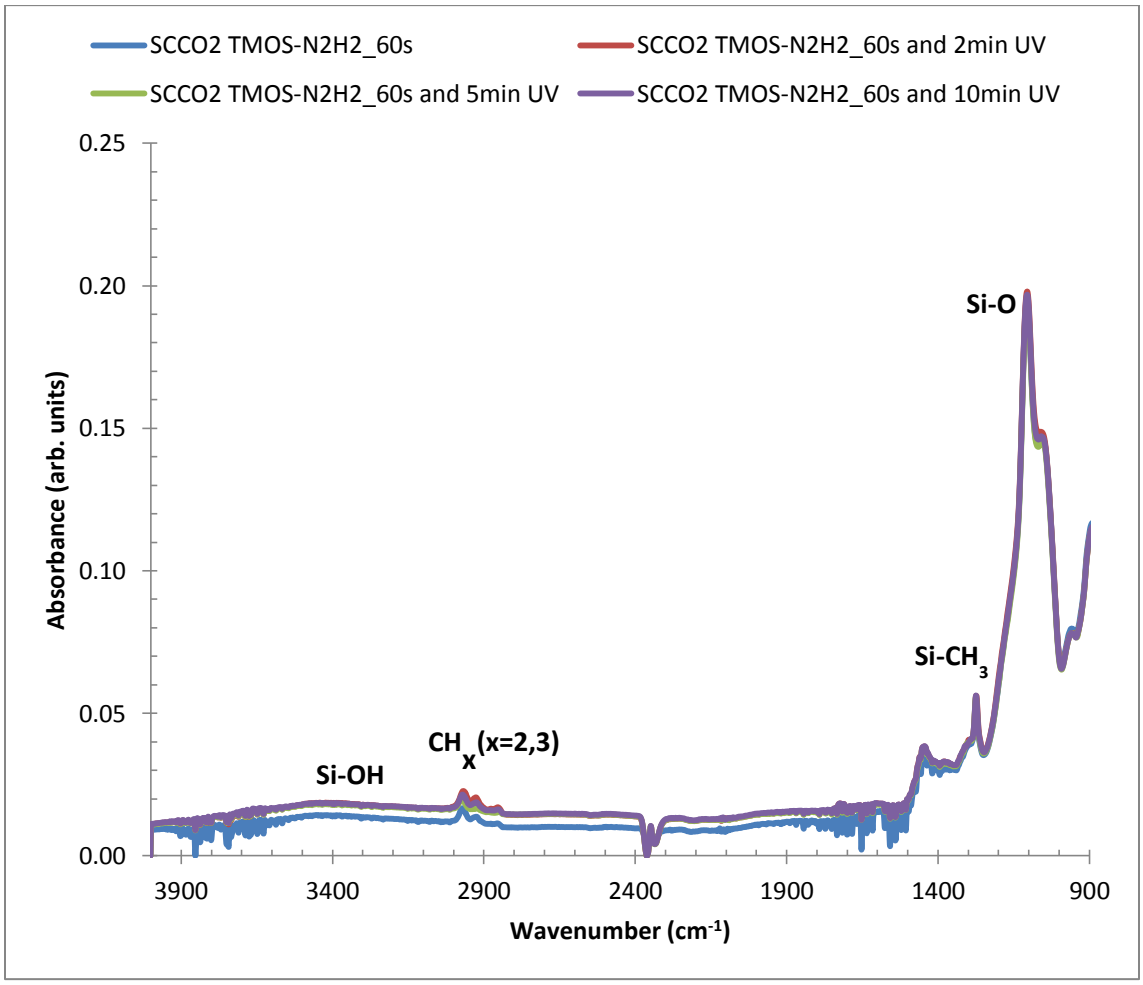

Fig. 6.6. FTIR spectra of repaired plasma N_2/H_2_60s low-k film after different UV irradiation times.

These FTIR results shows an increase in the methyl groups of the plasma damaged films after they were repaired, when they are compared to the as-received films which the data was presented in earlier chapters. These films demonstrated that in general, an increase in the UV curing time causes and increase in the absorption by the cage type of Si-O bonds to up to 5 min. This suggests that 6-hold ring of Si-O bond increases. On the other side, the Si-C-O stretch with methyl vibrations increases with increases in cure time which means that transformation of the low-*k* films has begun. Other researchers [15] have shown that carbon atoms when removed incorporate themselves in the Si-O network, making the low-*k* films dense. There was also an increase of the sub-oxide SiO_x ($x < 4$) structure. Shioya et al. [15] have demonstrated that the mechanical strength of low-*k* films unfailingly increases with increasing UV anneal time enabling the film to withstand CMP processes.

6.3.2 AFM

Three-dimensional AFM images of the unashed SiOCH films exposed to UV for various durations are presented in Fig. 6.7. These were analyzed using WSxM 4.0 Beta 1.3 software [16] over a scanning area of 1 μm^2. The unashed film (Fig. 6.7a) showed a fine network of structure (R_{rms} = 0.310 nm). After 2 min UV cure, the film showed a dense arrangement of fine topography (Fig. 6.7b) with a surface roughness of R_{rms}=0.345 nm. This was also observed after the film was exposed to UV source for 5 min (Fig. 6.7c), where the peaks has an R_{rms} of 0.353 nm. After 10 min cure time (Fig. 6.7d), a somewhat smoother film surface was observed (R_{rms} = 0.323 nm) when compared to the 2 and 5 min UV cure times. This can be attributed to the fact that after the 10 min cure

time, the hills begin to connect with each other, hence the peaks or hills seem a little wider.

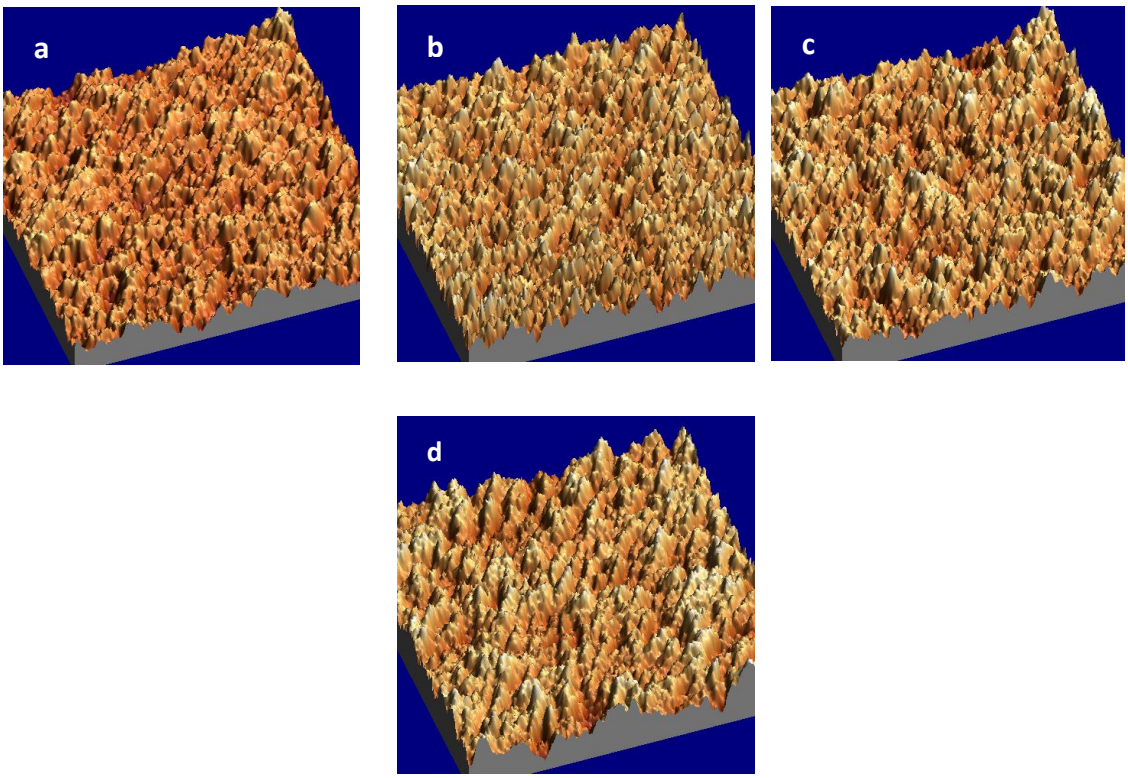

Fig. 6.7. Three-dimensional AFM images (1×1 um scan) [16] of the SiOCH (a) before and after different UV cure times, (b) 2 min, (c) 5 min, (d) 10 min.

After exposing the films to He/O_2 plasma for 30s (Fig. 6.8a), the heights or the roughness value nearly doubled (R_{rms} = 0.575 nm) because there were the development of large asperities. After SC-CO_2-TMOS treatment (Fig. 6.8b), there was a 14% increase in the roughness (R_{rms} = 0.658 nm) of the film. This was possibly due to the recovery process, where recovery takes place in the first few nanometers, thereby stopping other methyl groups from penetrating the film; therefore the silylating species settle on the already rough peaks resulting in an increase in the surface roughness value. Exposing the films to UV for 2 and 5 min (Figs. 6.8c and 6.8d) showed a surface roughness value of

0.678 and 0.684 nm respectively. Hence, there was not much effect on the films. This can be due to the TMOS forming stronger bonds with the low-*k* film or not reacting at all.

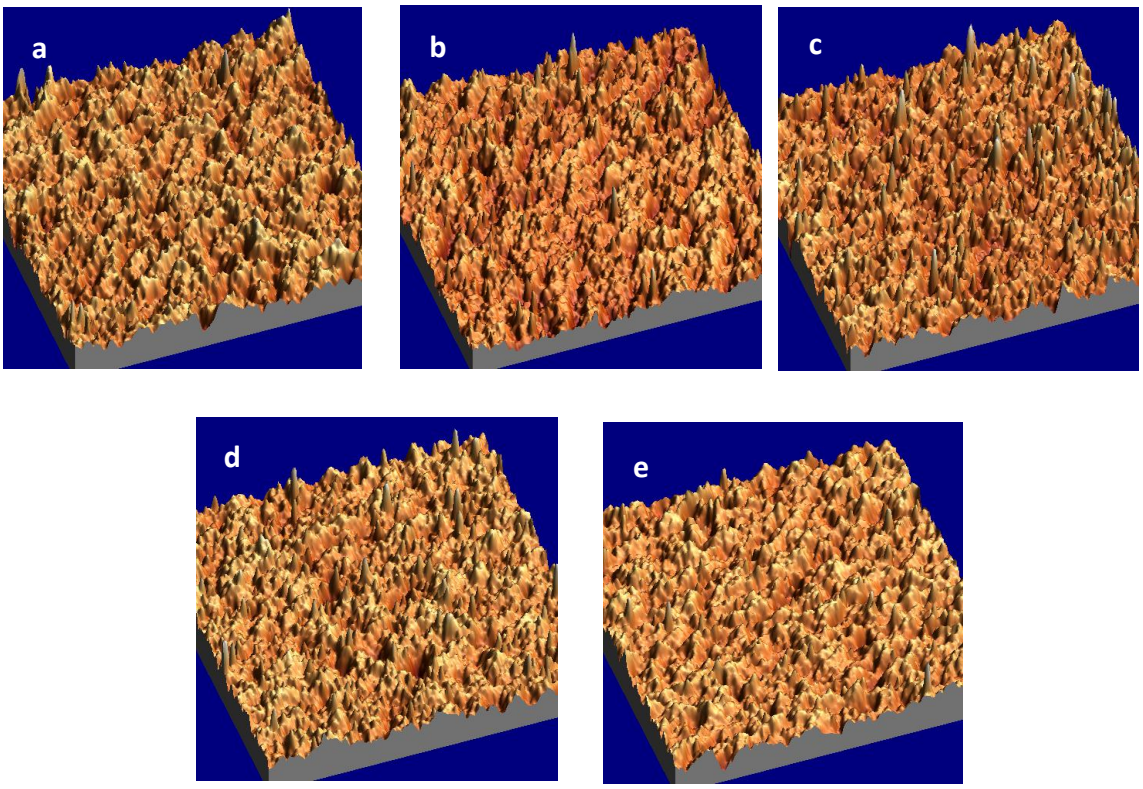

Fig. 6.8. Three-dimensional AFM images (1×1 um scan) of the He/O_2 plasma treated SiOCH (a) before and (b) after SC-CO_2 TMOS treatment with different UV cure times, (b) 2 min, (c) 5 min, (d) 10 min.

But a higher cure time of 10 min (Fig. 6.8e) caused the film to decrease in surface roughness value (R_{rms} = 0.585) to a value closer to the original value. This is because the 10 min UV cure seems to promote the development of valleys while at the same time appearing to join adjacent peaks. It is also possible that at 10 min, the silylating species reacted with the UV radiation.

The O_2 plasma has a different effect on the low-*k* SiOCH film than the He/O_2 plasma. Fig. 6.9a shows that even though there was an increase in the surface roughness

(R_{rms} = 0.448 nm), surprisingly the effect of the plasma was not severe as the He/O_2 plasma was. But both of them Figs. 6.8a and 6.9a shows that the hills begin to connect with each other by the highly rough valleys, in a way that the surface features tend to have similar heights to those of the adjacent points. When O_2 plasma is used, there is the possibility of a lot of chemical reactions because oxygen atoms are generally considered to be the primary reactive species [17,18]. The reaction between the hydrogen or carbon atoms and the reactive oxygen species progressively transforms the relatively flat surface into a roughened one from which CO, CO_2 and H_2O can desorb [19].

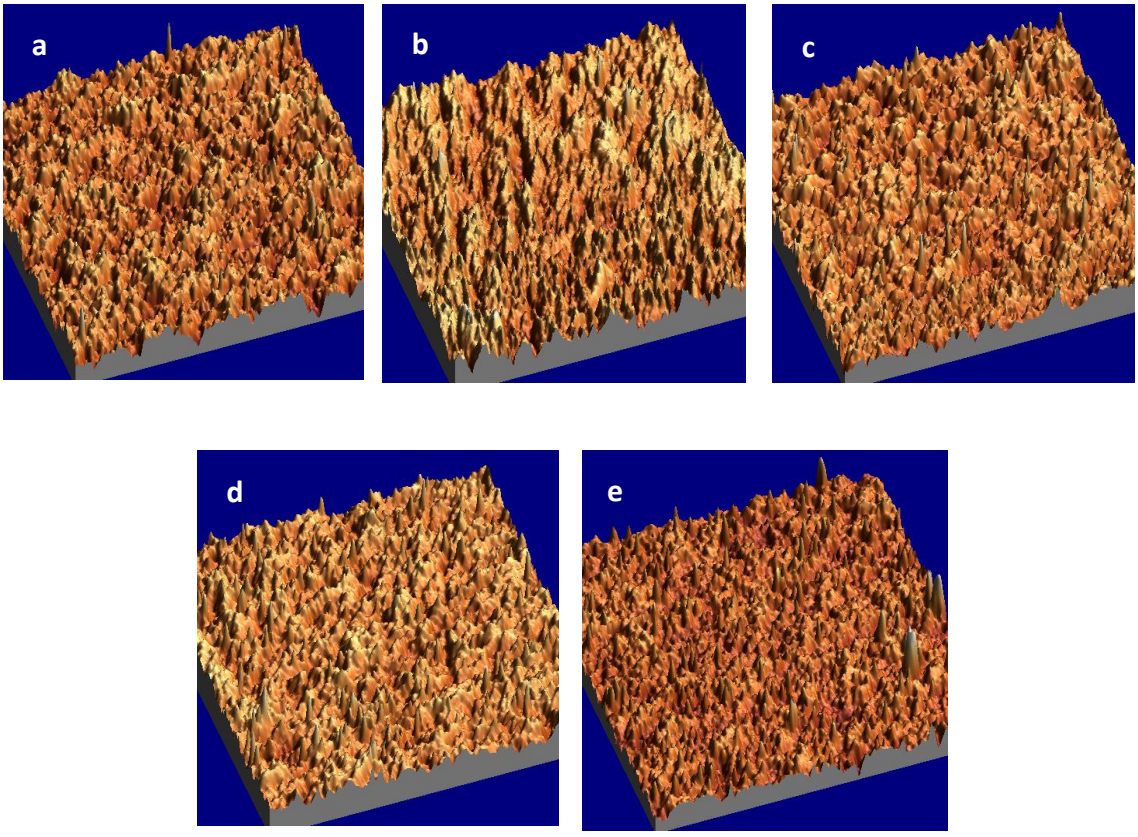

Fig. 6.9. Three-dimensional AFM images (1×1 um scan) of the O_2 plasma treated SiOCH (a) before and (b) after SC-CO_2 TMOS treatment with different UV cure times, (b) 2 min, (c) 5 min, (d) 10 min.

The silylation process causes surface roughness to increase (Fig. 6.9b) to 0.491 nm, but 2 and 5 min UV cure times (Figs. 6.9c and 6.9d) reduces the surface roughness to 0.468 and 0.485 nm respectively. The surface roughness increases (Fig. 6.9e) to 0.520 nm after 10 min UV cure. These surface roughness values validate the point that the O_2 and He/O_2 ash creates a greater number of asperities. The reducing plasma of N_2/H_2 for 30 and 60s respectively on the other hand appear to broaden the asperities. The three dimensional images of these films (Figs. 6.10 and 6.11) reveals the presence of merging hillocks. After silylation process and UV cure, the N_2/H_2 60s showed the merging of adjacent peaks (Figs. 6.11d and 6.11e), which made the films smoother especially after 10 min with a surface roughness of 0.396 nm.

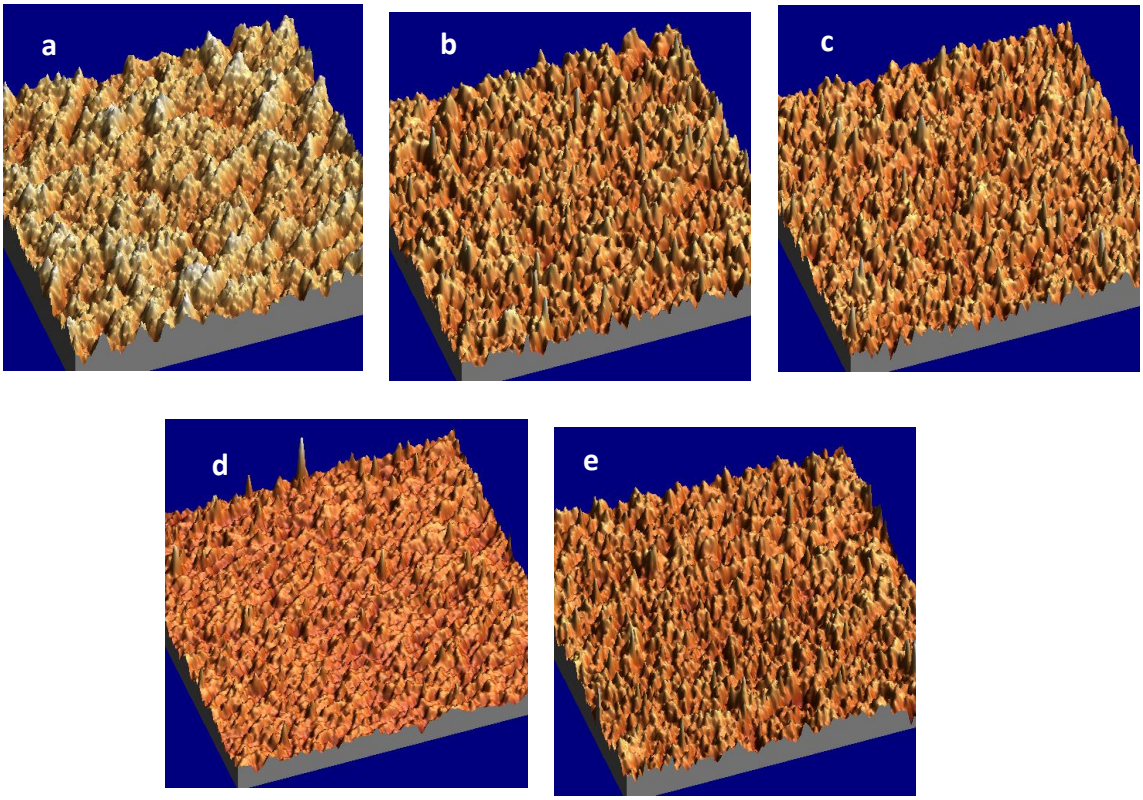

Fig. 6.10. Three-dimensional AFM images (1×1 um scan) of the N_2/H_2_30s plasma treated SiOCH (a) before and (b) after SC-CO_2/TMOS treatment with different UV cure times, (b) 2 min, (c) 5 min, (d) 10 min.

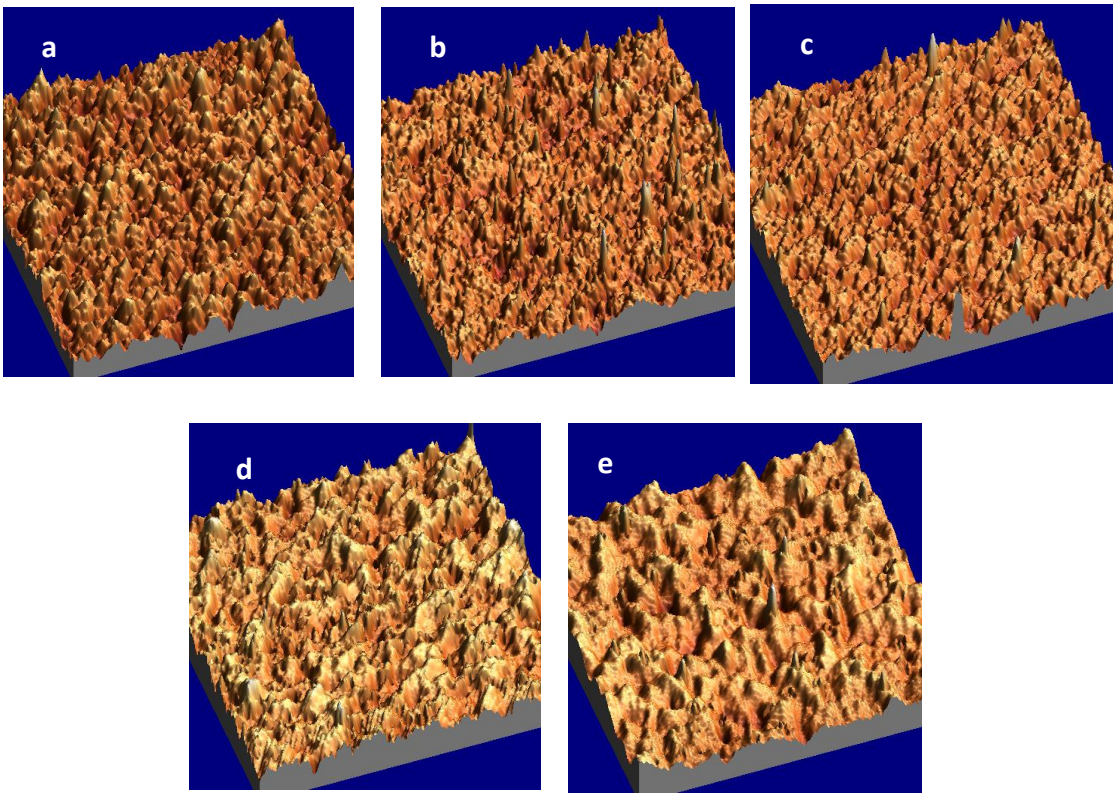

Fig. 6.11. Three-dimensional AFM images (1×1 um scan) of the N_2H_2_60s plasma treated SiOCH (a) before and (b) after $SCCO_2$ TMOS treatment with different UV cure times, (b) 2 min, (c) 5 min, (d) 10 min.

6.3.3 XPS

XPS experiments conducted to study the effect of UV cure on the films shows that the C atom concentration for the unashed film decreased with increasing curing time (Fig. 6.12). This is possibly due the loss of unstable methyl groups in the film. These decrease in carbon concentrations corresponded to increases in oxygen concentration. This is likely due to formation of additional siloxane bonds (Si-O-Si) at the expense of lost methyls. This data supports FTIR results showing an increase in Si-O peak after UV cure.

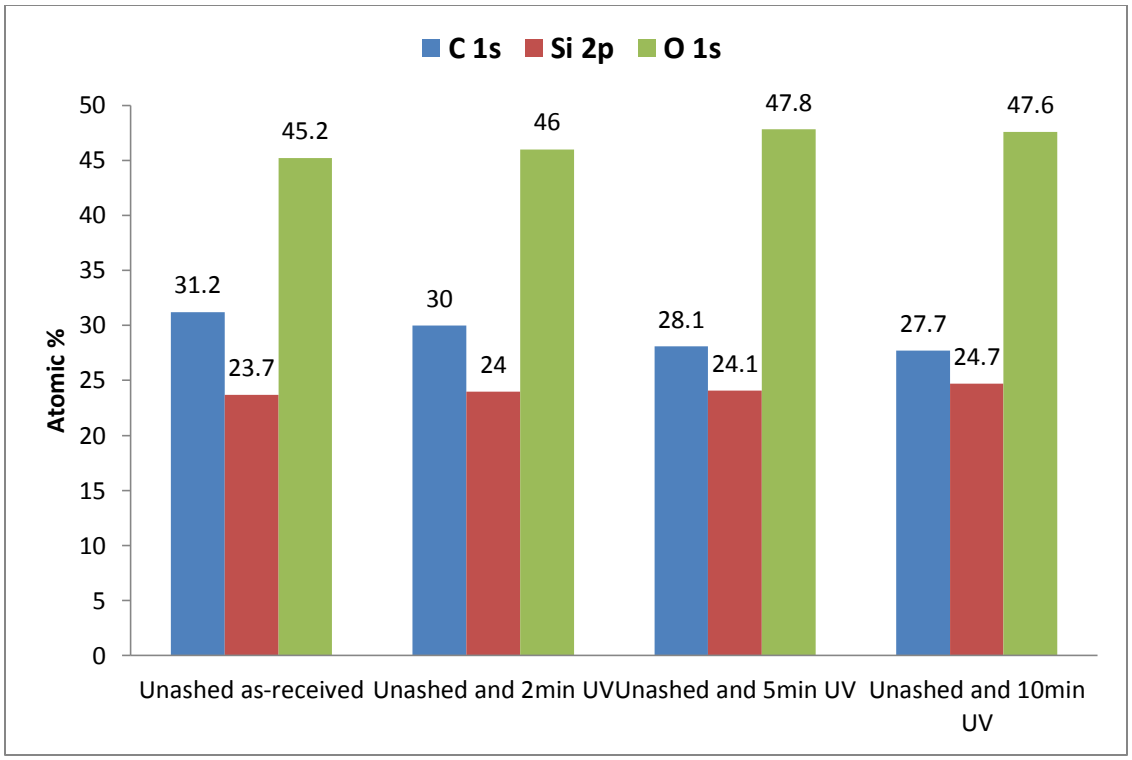

Fig. 6.12. XPS results for unashed films before and after UV curing.

After the silylation process, the He/O_2 ash film showed a significant increase in the carbon concentration suggesting the presence of methyl groups on the film surface. As the silylating species react most effectively within the few 20 Å, there is the possibility of the first few reactions preventing other species from penetrating the film. The carbon increased from an initial value of 6.5 atomic % to 19.8 atomic % (Fig. 6.13).

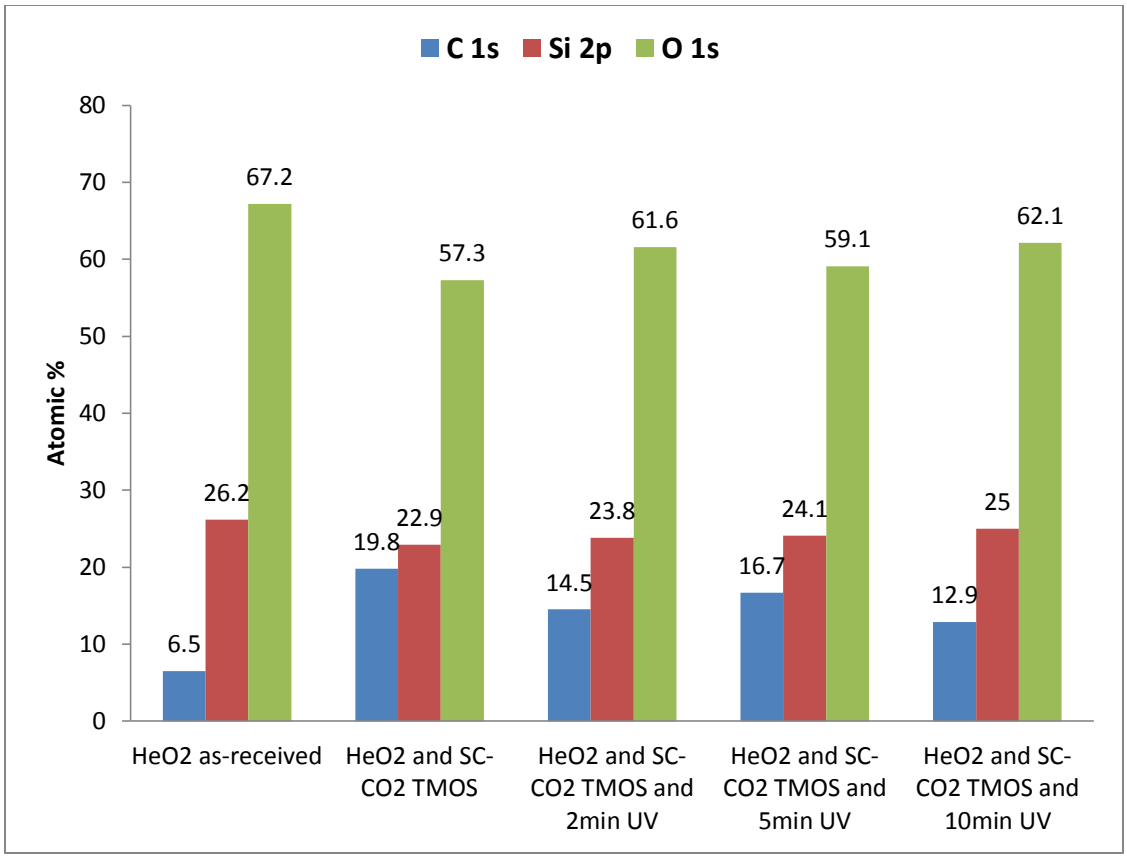

Fig. 6.13. XPS results for silylated He/O_2 plasma ashed film and UV cured.

Even though an increase in UV cure time seemed to remove the C atoms on the films surface, there is the possibility of a thin protective been formed, which prevents the UV from ridding the film of all the deposited species. After the SC-CO_2 treatment, the TMOS is at least partially unreacted on the film surface leaving methoxy groups. Some of these groups react or become incorporated within the film.

Even though the carbon content after the silylation process were similar for the He/O_2 and the O_2 ash, the O_2 ash film was more susceptible to the UV cure. After 2 min UV cure, the carbon content reduced from 16.4 atomic % to 9.6 atomic % (Fig. 6.14).

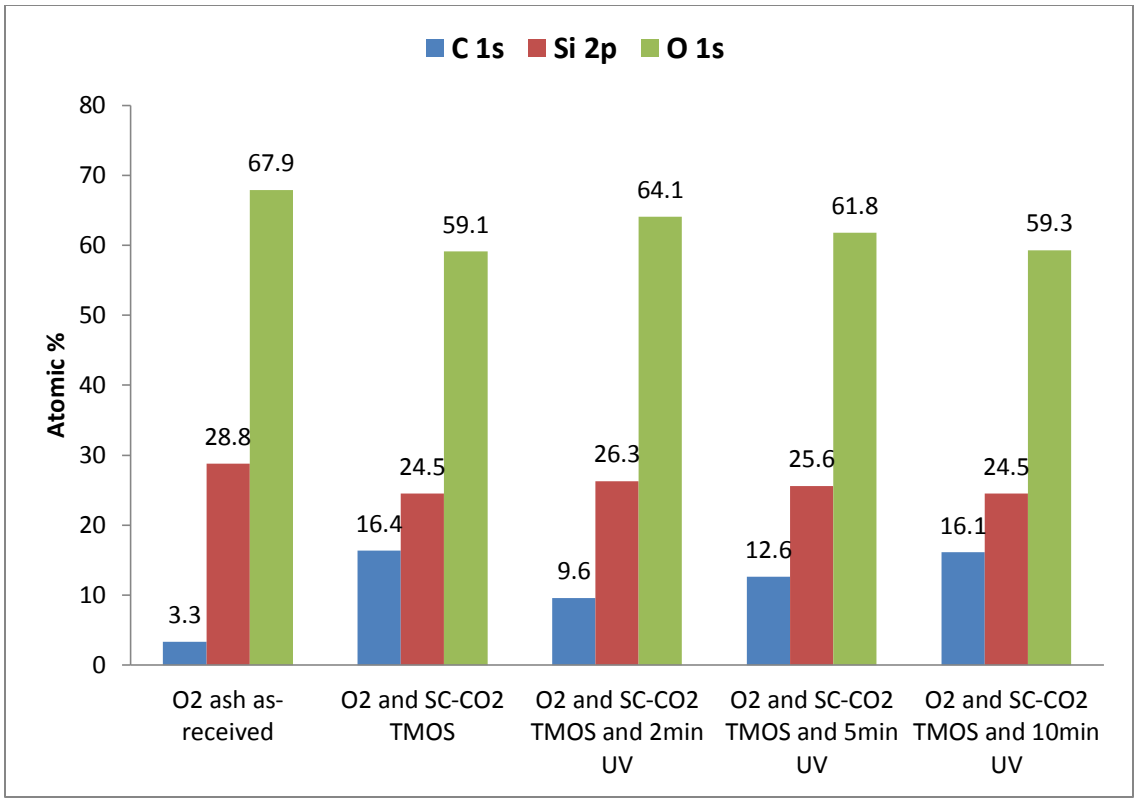

Fig. 6.14. XPS results for silylated O_2 plasma ash film and UV cured.

Because of this decrease, the O atom content also increased. These XPS data agree with the variation of the Si-O-Si peaks that was observed in the FTIR data. But strangely, further increase in UV cure time to 5 and 10 min saw an increase in the carbon content to 12.6 and 16.1 atomic % respectively. This agrees with the FTIR data where after 10 min of curing the CH_x peak was highest. There are two possible reasons for this behavior, the first after increasing the UV cure time, the UV was able to remove all the available methyl groups or silylation species deposited after the silylation process or the methyl species incorporate into the film and create a thin barrier layer.

The effect of the silylation process was different for the N_2/H_2 30s and 60s ash films; as the 30s ash was able to bond with more silylation species than the 60s ash film.

But the effect of the UV cure on the carbon concentration was similar if not the same after the 10 min cure, the 30s and 60s had carbon content of 12.0 and 11.6 atomic % respectively (Figs. 6.15 and 6.16).

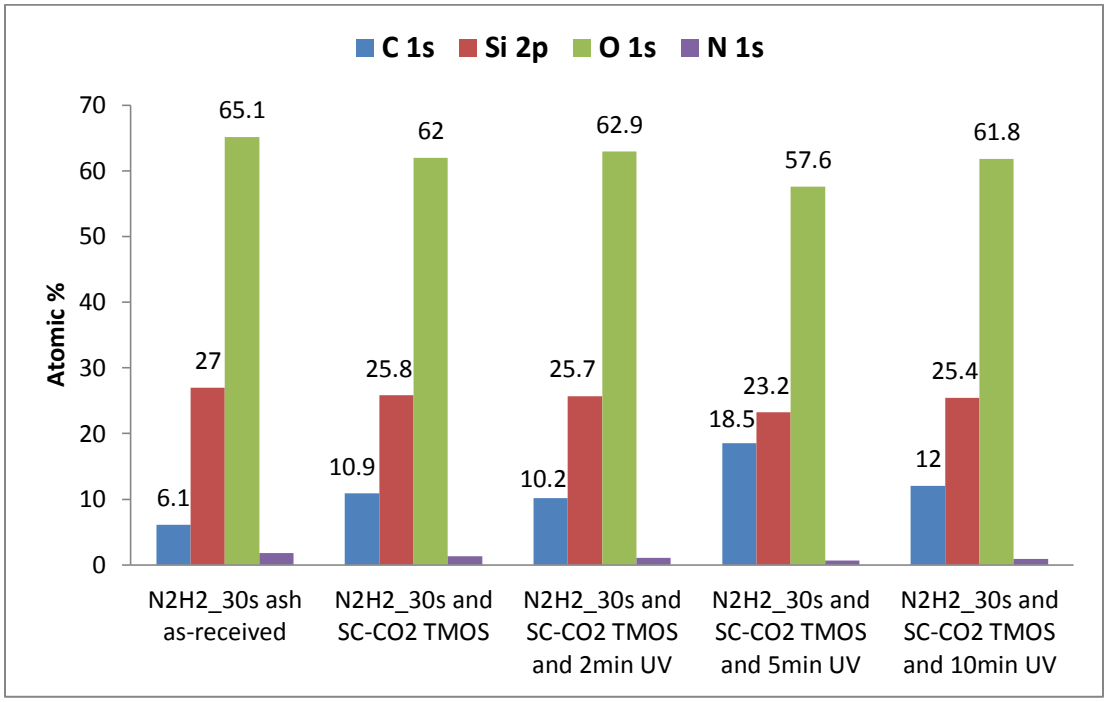

Fig. 6.15. XPS results for silylated N_2/H_2_30s plasma ash film and UV cured.

The small concentration of nitrogen present in the film is the result of residues left behind by the reducing plasma, N_2/H_2.

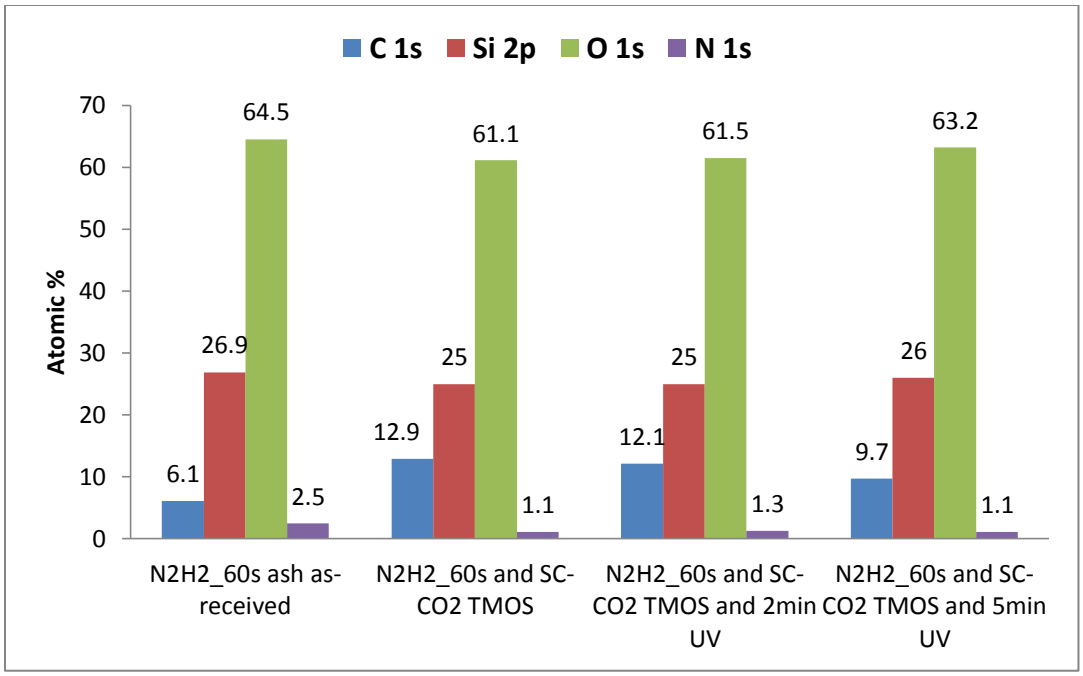

Fig. 6.16. XPS results for silylated N_2/H_2_60s plasma ash film and UV cured.

Even though for all the samples there was significant carbon loss during the UV cure, there was still a significant amount of carbon remaining. This is possible due to the formation of a thin barrier layer that prevents the UV from doing further damage to the underlying films or this wavelength is not efficient at inducing crosslinking. A nano-indentation procedure performed on this film may show an increase in the mechanical strength or the moduli of the film, which will make it able to withstand the rigorous process of CMP.

6.4 Conclusions

Unashed low-*k* SiOCH porous thin films and SC-CO_2/TMOS repaired plasma damaged low-*k* SiOCH films were annealed by UV light (320-500 nm wavelength) to seal the pores, enhance the mechanical strength and reduce the *k* value. FTIR data indicated the

removal of methyl groups and other unreacted species which would likely lead to a decrease in dielectric constant. Some of the carbon from the methyl groups appears to incorporate itself into the Si-O structure causing the Si-C-O peak in the Si-O structure to increase. These effects were also observed in the XPS data. A longer UV anneal could enhance mechanical strength, but on the other hand it can also increase density by decreasing pore size and porosity leading to an increase in *k*. The silylation species that were not able to penetrate the pores of the film because the first few species prevent others from filling the pores caused the films to increase in roughness which was observed in the AFM measurements.

6.5 References

[1] G. Maier, Prog. Polym.Sci. 26 (2001) 3.

[2] C. V. Nguyen, K. R. Carter, J. Hawker, J. L. Hedrick, R. L. Jaffe, R. D. Miller, J. F. Remenar, H. W. Rhee, P. M. Rice, M. F. Toney, M. Trollsas, D. Y. Yoon, Chem. Mater. 11 (1999) 3080.

[3] M. Morgen, E. T. Ryan, J. Zhao, A. Hu, T. Cho, P. S. Ho, Ann. Rev. Mater. Sci. 30 (2000) 645.

[4] H. J. Kim, Q. Shao, Y. H. Kim, Surf. Coat.Technol. 171 (2003) 39.

[5] K. Kim, D. H. Kwon, G. Nallapati, G. S. Lee, J. Vac. Sci. Technol. A16 (1998) 1509.

[6] A. Zenasni, B. Remiat, C. Waldfried, C. L. Cornee, V. Jousseaume, G. Passemard, Thin Solid Films 516 (2008) 1097-1103.

[7] C. H. Huang, H. L. Huang, C. I. Hung, N. F. Wang, Y. H. Wang, M. P. Houng, Jpn. J. of Appl. Phys. 47 (2008) 1532-1535.

[8] S. Rogojevic, A. Jain, W. N. Gill, and J. Plawsky, Electro-Chem. Solid State Lett. 5, F22 (2002).

[9] J. J. Kim, S. B. Jung, H. H. Park, and S. H. Hyun, Thin Solid Films 467 (2000) 377-378.

[10] S. S. Prakash, C. J. Brinker, A. J. Hurd, J. Non-Cryst. Solids 190 (1995) 264.

[11] Y. S. Mor, T. C. Chang, P. T. Tsai, C. W. Chen, S. T. Yan, C. J. Chu, W. F. Wu, M. Pan, W. Lur, S. M. Sze, J. Vac. Sci. Technol. B20 (2002) 1334.

[12] M. J. Loboda, C. M. Grove, R. F. Schneider, J. Electrochem.Soc.145 (1998) 2861.

[13] F. Ciaramella, V. Jousseaume, S. Maitrejean, M. Verdier, B. Remiat, A. Zenasni, G. Passemard, Thin Solid Films 495 (2006) 124.

[14] A. Grill, D. A. Neumayer, J. Appl. Phys. V94 (2003) 6697.

[15] Y. Shioya, T. Ohdaira, R. Suzuki, Y. Seino, K. Omote, J. of Non-Crystalline Solids 354 (2008) 2973-2982.

[16] I. Horcas, Rev. Sci. Instrum. 78, 013705 (2007).

[17] O. Joulbert, J. Pelletier, Y. J. Arnal, J. Appl. Phys. 65 (1989) 5056.

[18] A. G. Shard, J. P. S. Badyal, J. Phys. Chem. 95 (1991) 9436.

[19] M. Nakahara, Y. Sanada, J. Mater. Sci. 29 (1994) 3193.

CHAPTER 7

CONCLUSIONS AND FUTURE WORK

7.1 Conclusions

The first part of this work focused on the effects of different plasma treatments on low-*k* SiOCH films and the use of SC-CO_2 in combination with two different silylation agents (HMDS and DEDMS) to recover the hydrophobicity of these films. It was then established that:

- The average surface roughness was not significantly different after exposure to different plasmas, but the topographies of these films were markedly different especially for the oxygen and N_2/H_2 ashed films.
- All the ashed films showed similar contact angles because they had about the same amount of surface carbon concentration.
- After SC-CO_2 silylation, all films showed an increase in water contact angles because of the presence of methyl groups. The contact angle was higher when HMDS was used as a silylating agent than when DEDMS. This is because HMDS silylates to form trimethylsilyls as compared to dimethylsilyl for the DEDMS.

- Understandably, the amount of carbon on these films was higher for the HMDS treated films than the DEDMS films, as HMDS silylates and leave 3 methyl groups whereas there are 2 for DEDMS.
- IR studies confirmed that Si-OH and H-O-H groups were eliminated and replaced with methyl groups.
- Ellipsometry studies of the films showed a slight increase in the thickness of the films after repairing them. It was also observed from ellipsometric depth profile that the top layer of the films densified after plasma exposure.

In the second part of this work, the effect of temperature on these films after they have been repaired using SC-CO_2/HMDS and SC-CO_2/DEDMS were investigated.

- Increase in temperature from 25 ºC (RT) to 400 ºC reveal the removal of unstable methyl groups which caused the decrease in the CH_x (x=2, 3) peak and the Si-CH_3 stretch. This was observed for both the HMDS and DEDMS repaired films.
- This loss of carbon species was also confirmed with XPS studies; with HMDS repaired films losing more carbon than DEDMS repaired films. This suggests that DEDMS have stable stronger bonds than HMDS.
- The loss of carbons species caused reductions in the various films thickness.

In the first two parts of this work, it was established that silylating agents can recover surface hydrophobicity and also prevent water and precursor moieties from intruding into porous silica-based low-*k* films. The third part of this work was focused on

the surface modification and UV curing of these porous low-*k* films using TMOS as the silylating agents. This was done to verify if the silylating species will readily react with UV radiation to form very thin barrier layers.

- Exposure of these films showed a decrease in methyl groups, which is because of the removal of unstable methyl or hydrocarbons from these films.
- Some of the carbon species from these unstable methyl groups incorporates themselves in the Si-O structure, causing an increase in the Si-C-O peak within the Si-O structure. This is an indication that a deformation of the film has begun.
- Because the first few silylation species that reacts with the film seal the topmost pores preventing other species from penetrating deep in the film, hence, they can only settle on top of each other. This caused an increase in surface roughness as observed in the AFM data.
- Ellipsometric measurements only showed slight changes in the films thicknesses and refractive indices.

7.2 Future Work

Further work on these low-*k* films are proposed but not limited to the following:

- Different plasmas have different effects on the dielectric constant of these films. It is thus suggested that capacitance-voltage and current-voltage measurements should be performed on these films to find the dielectric constant and leakage current, respectively.

- UV treatments were performed on the films after SC-CO_2/TMOS to enhance the mechanical properties of these films. Hence, it is proposed that nano-indentation be performed on the films to measure changes in moduli.
- With regards to structural changes, even though ellipsometric measurements were able to give an idea of the effects of the heat and UV treatment on the density of the film, more details about the density and pore sizes of these films can be achieved by using x-ray reflectometry and positron annihilation lifetime spectroscopy (PALS).
- Knowing the type of released gas generated by the UV anneal is important for deciding how best to remove CH_3 bonds from the film by the UV anneal. Thermal desorption spectroscopy (TDS) is one equipment that can be used to measure the released gases.